2020

On the Cyclic Inelastic Behavior and Shakedown-Based Design of Metallic Materials and Structures: Analysis and Experiments

Ismail Soner Cinoglu
Lehigh University

On the Cyclic Inelastic Behavior and Shakedown-Based Design of Metallic Materials and Structures: Analysis and Experiments

by

Ismail Soner Cinoglu

Presented to the Graduate and Research Committee

of Lehigh University

in Candidacy for the Degree of

Doctor of Philosophy

in

Mechanical Engineering

Lehigh University

January 2020

Approved and recommended for acceptance as a dissertation in partial fulfillment of the requirements for the degree of Doctor of Philosophy.

_____
Date

_____
Dissertation Director

_____
Accepted Date:

Committee Members:

_____
Natasha Vermaak, Committee Chair

_____
Herman Nied

_____
Spencer Quiel

_____
Yue Yu

Acknowledgements

Firstly, I would like to express my gratitude to my Ph.D. advisor, teacher, and mentor Dr. Natasha Vermaak. She has thought me how to be a researcher and provided me with countless opportunities to improve myself professionally and personally. Her continuous positive support made this thesis possible.

In addition to my adviser, I would also like to thank the rest of my Ph.D. committee members: Dr. Yue Yu, Dr. Spencer Quiel, and Prof. Herman Nied, for providing valuable insight to me in preparation of this dissertation.

I thank my labmates Xiu Jia, Jerard Gordon, Ali Charbal, and Zhen Zhang. They have provided both technical and emotional support for the last five years to me. I was lucky to have such good friends, and I hope it stays this way for years to come. I also appreciate the excellent technical support provided by and long discussions with my colleague, Richard Towne. I also thank my dearest friends Sila Gulgec, Burak Ozdemir, Nur Koncuy Ozdemir, and Irem Bilgili. They have been a second family away from home.

My special thanks go to my family. My wife, Fatma Ayancik Cinoglu, encouraged me to start my degree and stayed by my side at every single day of it. I am forever grateful to her for her patience and for giving me the strength to achieve my goals. Finally, I am thankful to my parents and my brother for shaping me to the person who I am today. I would not be at this point in my life if it were not for them.

Contents

List of Tables

List of Figures

Abstract

Metallic structures in many engineering disciplines are subject to repeated and extreme thermomechanical loading conditions. The conventional design of these types of structures, that are not limited by high-cycle fatigue, employs first-yield criteria in order to avoid failure due to cyclic plasticity. However, yield-limited designs often fail to produce acceptable solutions for multifunctional structures in extreme environments. In order to overcome these limitations and capitalize on the elastoplastic load-bearing reserve, this dissertation analytically, numerically, and experimentally demonstrates inelastic design methods that exploit shakedown for metallic structures.

Several analytic and numerical case studies are presented that are relevant to aerospace and civil engineering applications. These include built-in beam structures, auxetics, and reinforced concrete structures. Experimentally, new macroscopic demonstrations of shakedown behavior and shakedown design (avoiding alternating plasticity and ratchetting) at ambient and elevated temperatures are made for two common engineering materials: the nickel-based superalloy IN625 and stainless steel 316L. The results indicate that allowing shakedown can significantly expand the feasible design space (2-4 times) compared to conventional first-yield. It is found that interactions with other material and structural behaviors such as dynamic strain aging, creep, and buckling can have both propitious and detrimental effects on the macroscopic shakedown response. In this way, this dissertation serves to promote more wide-

spread adoption of shakedown-based analysis in realizing new structural concepts and accurately assessing the structural integrity of existing components.

Chapter 1

Introduction

Metallic structures in many industrial sectors, including nuclear, aerospace and automotive, are often subject to extreme loading conditions that involve cyclic thermal and mechanical interactions. In such cases, and for structures that are not limited by high-cycle fatigue, conventional thermostructural design remains within the elastic domain. However, yield-limited designs often fail to produce acceptable solutions for multifunctional structures in extreme environments. Most notably, designs for high-temperature structures based purely on elasticity lead to bulky structures that are unsuitable for weight-critical applications such as high-speed aircraft that experience significant aerothermal heating. As a second example, components in nuclear power plants are often subject to thermomechanical loads that were not anticipated in the design process, and subsequent elastic analyses of structural integrity can lead to overly conservative, costly retirements that are wholly unnecessary. To overcome these limitations and capitalize on the elastoplastic load-bearing reserve, this dissertation analytically, numerically, and experimentally demonstrates inelastic design methods that exploit macroscopic shakedown for metallic structures subject to repeated thermomechanical loading conditions.

For materials and structures that exhibit time-independent behavior, shakedown

design theorems have found their most extensive application in the nuclear pressure vessel industry to delineate the boundaries between shakedown, cyclic plastic straining (alternating plasticity) and ratchetting [1–5]. These theorems have replaced traditional yield-limited assessments of structural integrity and are used widely in the design process to evaluate a structure's response to unanticipated thermomechanical loads. The operational space is extended by allowing shakedown to occur, whereby stresses locally exceed the yield strength of a material in the first few cycles of load and thereafter, fully elastic response is recovered. The range of possible structural responses is most often illustrated through the use of a Bree load-interaction diagram, which indicates combinations of loads (often thermal and mechanical) that lead to various cyclic material and structural behaviors [1, 6]. Figure 1 illustrates the classic Bree diagram for a thin-walled cylinder (with a radius, R and thickness, t), subjected to a fixed internal pressure, P, and a cyclic radial temperature difference, ΔT. The ordinate is $\mathrm{\Delta T/\Delta T}_o$ where $\mathrm{\Delta T}_o$ is the temperature difference required for yield initiation in the absence of a mechanical load ($\Delta T_o = 2\,(1-\nu)\,\sigma_o/E\alpha$); the abscissa is $\mathrm{P/P}_o$ with P_o being the pressure that causes yielding in the absence of a temperature gradient ($P_o = PR/t$) where σ_o is the yield strength, E is the Young's modulus and α is the coefficient of thermal expansion (CTE). Note that here material nonlinearities associated with temperature-dependent properties are not accounted for and only small deformations are considered [7–11].

For this configuration, the elastic domain is defined by $\mathrm{P/P}_o + \Delta T/\Delta T_o < 1$. At one extreme, wherein $\mathrm{P/P}_o > 1$, *plastic collapse* occurs on the first load cycle, i.e. the thin wall experiences complete yielding. For intermediate combinations of P and ΔT, one of three behaviors is obtained (Figure 1.1) [7]. (i) In the *shakedown* regime, localized plastic deformation that occurs in the early stages of cycling gives rise to residual stresses that prevent plastic deformation in subsequent cycles. The consequence is purely elastic behavior during long term cycling, which could dra-

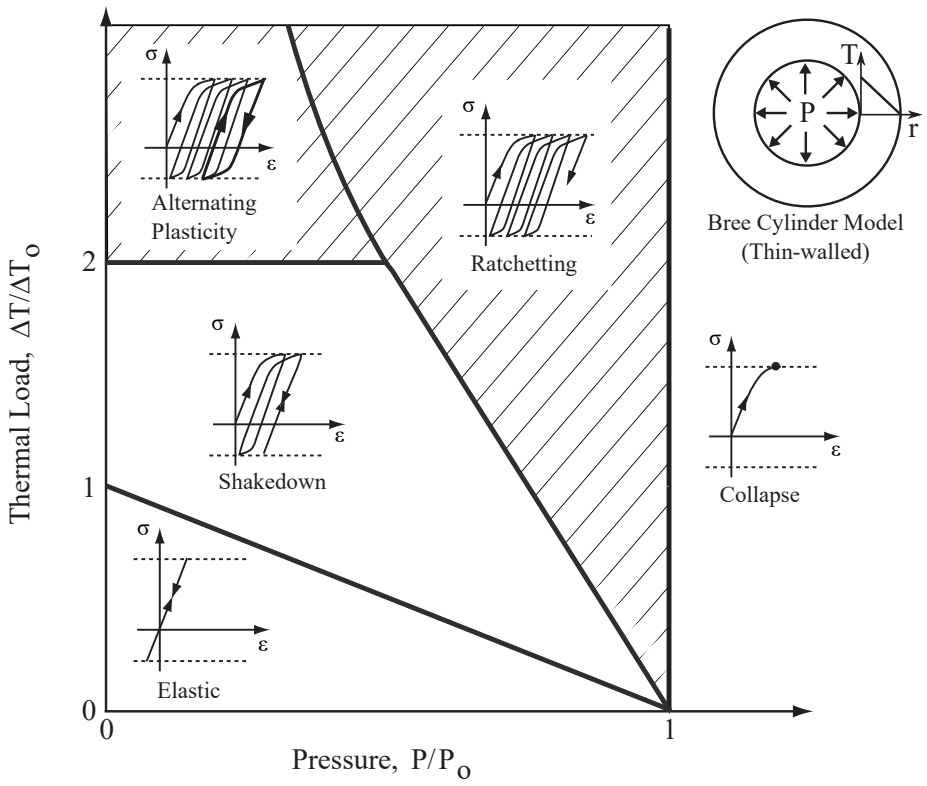

Figure 1.1: *Bree interaction diagram for the benchmark problem of a thin-walled cylinder and schematics of the resultant cyclic elastoplastic behaviors [1].*

matically increase lifetimes. (ii) *Alternating plasticity* results from loading beyond the shakedown limit. Here the plastic strain increment obtained during the first half of each loading cycle is followed by a plastic strain increment of equal magnitude but opposite sign during the second half. No net strain accrues during each cycle but the structure ultimately fails by low-cycle fatigue. (iii) *Ratchetting* refers to the condition in which a net increment of plastic strain accumulates during each cycle, eventually causing rupture.

These safe (elastic, shakedown) and inadmissible (ratchetting, alternating palsticity) cyclic elastoplastic behaviors may occur due to material and/or structural effects. Material ratchetting and structural rathetting under cyclic loading conditions are defined by Hubel [12, 13]. Hence, it is worthwhile to distinguish between material shakedown and structural shakedown in a similar way. Material shakedown occurs

in the presence of homogeneous stress distributions and by the hardening of a metal during plastic deformation. The yield surface of the material evolves (expands, translates and deforms) during initial load cycles and macroscopic shakedown occurs when subsequent stresses upon cycling stay within the yield surface. Structural shakedown occurs when non-homogeneous stress distributions exist in the structure. Structural shakedown can be obtained even when an elastic-perfectly plastic material behavior is assumed. An example of this is the classic work by Bree on thin-walled cylinders (Figure 1.1) [1]. In this dissertation, both structural and material shakedown will be considered.

Shakedown-based design methods have been implemented in the design codes for pressure vessels of nuclear power plants [2, 3]. In addition to nuclear engineering, shakedown-based designs have been used for tribology, multilayer semiconductor materials, pavement, and shape memory alloy components [14–17]. However, there are numerous applications that are not limited by high cycle fatigue, for which the potential benefit of shakedown-based designs remain unexplored or under-utilized. For example, combustor liners for hypersonic flight, as well as some automotive, gas turbine, and construction applications.

Determination of shakedown *limits* is the key component of developing shakedown based designs. This can be achieved analytically, numerically and experimentally. Analytical methods to identify shakedown limits typically utilize shakedown theorems that are classified in two main approaches, *lower bound* and *upper bound theorems*. Both approaches aim to determine the shakedown limit of a structure within a variable loading domain. The *lower bound* shakedown theorem (also called Melan's theorem) states that "if a self-equilibrating, time-independent residual stress field can be found that remains within the yield limit when combined with any fictitions elastic stress in a loading domain, the structure will shakedown" [18]. The *upper bound* theorem states that a structure will shakedown if the energy dissipated

by the plastic deformation is greater than or equal to the work done by the external loads within a cycle [18]. The original shakedown theorems assume small displacements and elastic-perfectly-plastic material behavior, but they have been extended for many conditions, including hardening, creep and temperature-dependent material properties [19–21]. Implementation of Melan's theorem in shakedown limit determination has also been studied by many researchers. The reader is referred to a review article by Weichert and Ponter for a full historical evolution of shakedown theory [21]. The advantage of the conservative lower bound shakedown theorem is that it requires only a linear elastic solution; the full loading history is not required to determine shakedown limits. As a conservative approach, this dissertation adopts the lower bound shakedown theorem. It will be further explained and used to develop an analytical shakedown limit in Chapter 2, Section 2.1.1 for a simple built-in beam relevant for some aerospace applications. Note that the upper bound shakedown theorem is not within the scope of this dissertation and will not be discussed further.

While analytical solutions implementing these theorems are available for some simple structures, typically numerical methods are required, especially when geometric and material nonlinearities are present. In such cases, shakedown limit determination is most often achieved via finite element analysis (FEA) and optimization techniques [22, 23]. Numerical approaches for shakedown limit determination that employ the lower or upper bound theorems are termed "Direct Methods". In contrast, the "classical load history approach" follows the incremental or step-by-step evolution of a system and finds the actual residual stress field that would result from the actual loading history that is deterministically known. It should be noted that "step-by-step" approaches and "direct methods" are not competing methods, but rather complementary as each provides different information and they often have separate domains of applicability. For example, direct methods are useful when the exact loading history is unknown and they avoid cumbersome incremental load-

history based calculations. In contrast, load-history-based approaches provide the evolution of local quantities that are often critical to lifetime analysis. In this dissertation, step-by-step numerical analysis is also used to demonstrate shakedown behavior and find limits for several test case structures in Chapter 2: built-in beams, reinforced concrete structures, and auxetic structures.

Experimental demonstrations of shakedown behavior and validation of analytical and numerical methods are essential in order to convince designers to adopt shakedown-based approaches. However, experimental shakedown studies of engineering materials and structures available in the open literature are very limited. To date there is a shortage of tests involving cyclic, mechanical or thermomechanical loads performed to investigate shakedown limits [24–29]. The current state-of-the art uses servohydraulic axial or axial-torsional testing rigs with or without induction heating to determine the shakedown behavior of hollow cylindrical samples or multi-bar systems.

For example, Heitzer *et al.* used an INSTRON 1343 test rig to test thick-walled cylindrical samples commonly used in the nuclear industry [25]. To demonstrate shakedown behavior, the authors applied a constant torque and a cyclic axial load. As multiaxial loading causes a non-homogeneous stress distribution through the thickness of a thick-walled cylinder, the tests induce simple structural shakedown. An INSTRON extensometer was used to monitor strains and the torsional angle was recorded. Several experiments with various combinations of the axial and torsional loads were tested to identify combinations that resulted in shakedown (manifested by the stabilization of the torsional angle with the cyclic alternating axial force) or inadmissible ratchetting behavior (the torsional angle increased in an unbounded manner despite the constant moment loading). Building on this existing work, Chapter 3 presents new experimental demonstrations of macroscopic *uniaxial* shakedown behavior for two common engineering materials: 316L stainless steel (Section 3.3)

and a nickel-based superalloy, Inconel 625 (Section 3.4).

In summary, this dissertation presents analytic, numerical, and experimental shakedown studies that are relevant to aerospace and civil engineering applications. The first combined analytical and numerical shakedown design study of thin-walled structures where interactions with thermal buckling are considered is presented in Chapter 2. In Chapter 3, cyclic uniaxial experiments with constant mean stress and variable stress amplitudes are employed to demonstrate macroscopic shakedown behavior of stainless steel 316L and Inconel 625 at ambient and 600^oC. Both contact and non-contact measurement techniques are employed to distinguish shakedown from inadmissible behaviors in the presence of time and rate-dependent effects (creep and dynamic strain aging). Additional experiments are performed in order to provide inputs for constitutive models for cyclic plasticity simulations. In Chapter 4, simulations of the ambient cyclic inelastic behavior of stainless steel 316L are presented and compared to the experimental results in Chapter 3.

Chapter 2

Case studies of elastoplastic shakedown design for structures

In this chapter, several case studies are used to demonstrate analytical and numerical shakedown analysis. These studies highlight potential lightweighting, robustness, and durability benefits from shakedown design for structures relevant to aerospace and civil engineering. The structures investigated in this section are subject to cyclic thermomechanical loading conditions. In particular, in all of the case studies either the mechanical load is kept constant during thermal cycles or the mechanical load is cycled while a constant thermal load/distribution is maintained.

Section 2.1 considers a simplified built-in beam that is relevant for aerospace applications, including combustor liners for hypersonic flight and stiffeners for exhaust-washed structures on high-speed aircraft (Figure 2.1). The beam is subject to a constant distributed load and a cyclic uniform thermal load. In Section 2.1.1, shakedown limit determination for this structure is first performed analytically under the simplifying assumptions of small displacements and no interaction between thermal and mechanical effects. In Section 2.1.2, the problem is reconsidered by allowing for nonlinear geometrical effects and thermomechanical coupling using step-by-step

finite element analysis. Perforated auxetic structures with negative Poisson's ratio have recently been shown to have excellent low cycle fatigue performance when incorporated in gas turbines where film cooling is needed. Based on these results, in Section 2.2, the shakedown behavior of similar perforated sheets is explored under a cyclic uniaxial mechanical load and a uniform steady temperature. Finally, a civil engineering application is considered in Section 2.3 that investigates shakedown benefits in the design and analysis of reinforced concrete structures for resilience under fire events.

2.1 Case Study I: Built-in beam structure for aerospace applications

For aerospace applications, beams and plates are common idealized thin-walled structures that are relevant for aerothermally heated and mechanically loaded aircraft surfaces (Figure 2.1) [30–32]. These include cooling channels in rocket nozzles, structural components in hypersonic vehicles, and stiffeners for exhaust-washed structures in highspeed aircraft. The elastoplastic design of beams and plates has been treated in previous analytical, numerical and experimental work [33–46] focusing on variable section thicknesses [35] and beams under axial loads, bending moments and transverse temperature distributions with hardening and damage [42]. However, additively manufactured systems enable new types of thin walled designs, raising fundamental design questions relating to the coupling between aspect ratios, temperature changes and cyclic plasticity. For example, additive manufacturing will push designs in thin-walled limits to capitalize on improved heat transfer associated with tortuous cooling channels (Figure 2.1). These and many other applications that are not limited by high cycle fatigue are designed to avoid cyclic plasticity, i.e. fall in the shakedown regime.

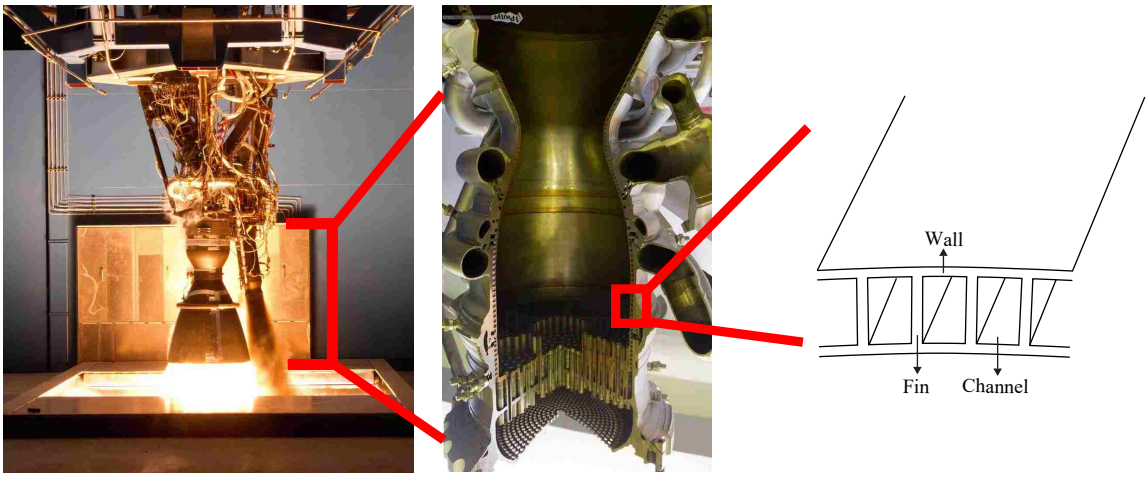

Figure 2.1: *Regenerative cooling structure of a liquid-propellant rocket nozzle.*

The thin-walled structure shown in Figure 2.1 is modeled as a built-in beam (Figure 2.2). Clamped boundary conditions are assumed such that the ends of the beam are constrained from translation and rotation. The structure is analyzed under a thermomechanical load shown in Figure 2.2b. The loading conditions consist of a steady and uniform distributed load (P) and a uniform temperature cycling on the entire beam. Material properties representative of Inconel 718 nickel-based superalloys at an elevated reference temperature of approximately $600°C$ ($E = 171\ GPa$, $\sigma_o = 1020\ MPa$, $\alpha = 14.4 \times 10^{-6}\ 1/°C$) are used assuming elastic-perfectly plastic behavior.

2.1.1 Case Study I-a: Built-in beam structure assuming small displacements

For preliminary design purposes, in this section analytical limits for shakedown are developed. The idealized thermostructural component depicted in Figure 2.2 is first analyzed assuming plane stress and neglecting shear.

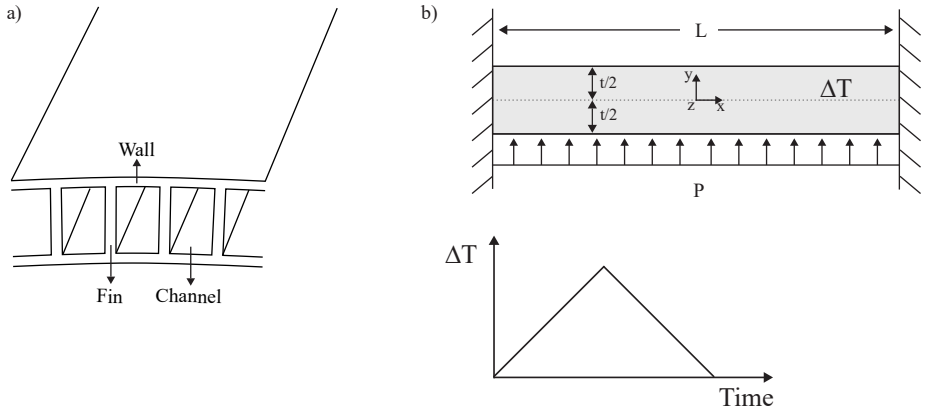

Figure 2.2: *a) Schematic illustration of cooling channels in rocket nozzles and structural components in hypersonic vehicles, motivating the present study. b) Idealized structure and loading used to map cyclic plasticity responses.*

Elastic Solution and First-yield

Under the loading and boundary conditions, the distribution of mechanical stress in the beam, $\sigma_{xx}(x, y)$, can be found from the relationship between the pressure loading, P (per unit depth, Z), and beam deflection, u, ($d^4u/dx^4 = P/EI$) [47]. Elasticity subject to the usual beam approximations yields:

$$\sigma_{xx} = -\frac{Py}{2t^3}\left(12x^2 - L^2\right) - E\alpha\Delta T. \tag{2.1}$$

From Eq. 2.1, the onset of plastic yielding occurs at $x = \pm L/2$ and is given by:

$$\frac{PL^2}{t^2} + 2E\alpha\Delta T = 2\sigma_o. \tag{2.2}$$

Extension of this plane stress small deformation analysis to i) pinned boundary conditions and ii) plane strain assumptions for both pinned and clamped conditions is presented in Appendices A.1 and A.2.

Shakedown Limit

In order to analytically determine the shakedown limit, the use of lower or upper bound shakedown theorems is required [18, 48]. For this work, a conservative approach using Melan's classical lower bound theorem is utilized, which assumes small strain theory and an elastic-perfectly-plastic material model. Although not used here, it should be emphasized that Melan's original theorem has been extended for many conditions, including hardening, creep and temperature-dependent material properties [19–21]. Melan's original theorem considers a solid body, R, subjected to a displacement boundary condition on part of it's boundary, $\partial_1 R$, and the remainder of the boundary, $\partial_2 R$, is subjected to a prescribed cycle of traction. The theorem states that "a solid is guaranteed to shake down if any time independent residual stress field, $\bar{\rho}_{ij}$, can be found which satisfies i) the equilibrium equation $\partial\bar{\rho}_{ij}/\partial x_j = 0$; ii) the boundary conditions $\bar{\rho}_{ij} n_j = 0$ on $\partial_2 R$, where n is a unit vector normal to the boundary $\partial_2 R$; and iii) when the residual stress is combined with the fictitious elastic solution, the combined stress does not exceed yield $f(\sigma^{\varepsilon}_{ij} + \bar{\rho}_{ij}) \leq 0$ at any time during the cycle of load" [49, 50].

A schematic illustrating the use of Melan's lower bound theorem is presented in Figure 2.3 for the built-in beam structure. Figure 2.3 displays stress distributions at the critical beam end cross-sections ($x = \pm L/2$). In these schematics, solid lines show the yield stress, σ_o, in tension and compression. In Figure 2.3a, potential elastic stresses resulting from the uniform pressure load only are shown. In Figure 2.3b, compressive thermal stresses are added to the mechanical-only stresses (assuming purely elastic response). The resulting stress level is shaded for combined thermomechanical loading. The fictitious portion is indicated with a dashed line. This stress state is fictitious because it exceeds the yield stress. In Figure 2.3c, a potential residual stress field, $\bar{\rho}_{ij}$, satisfying Melan's theorem for shakedown is found

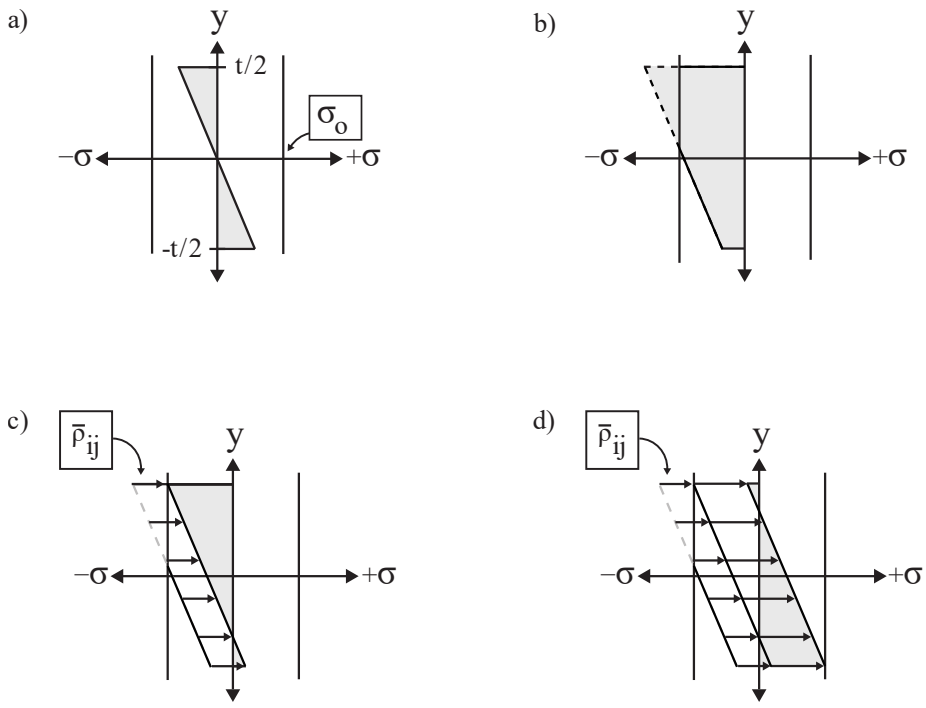

Figure 2.3: *Shakedown determination at critical cross-sections at $x = \pm L/2$ with schematic stress distributions for different loading cases. a) The elastic stress distribution due to mechanical loading only. b) The fictitious elastic stress distribution due to combined thermomechanical loading. c) A potential residual stress field ($\bar{\rho}_{ij}$) upon thermal loading. d) The residual stress distribution ($\bar{\rho}_{ij}$) upon thermally unloading, required for shakedown to occur.*

using this fictitious elastic stress state upon thermal loading. The potential residual stress field is the stress necessary to return the maximum (absolute value) fictitious thermomechanical stress to the yield limit:

$$\sigma_{xx}(\pm\frac{L}{2}, \frac{t}{2}) = -\frac{PL^2}{2t^2} - E\alpha\Delta T + \bar{\rho}_{ij} = -\sigma_o, \tag{2.3}$$

giving,

$$\bar{\rho}_{ij} = \frac{PL^2}{2t^2} + E\alpha\Delta T - \sigma_o. \tag{2.4}$$

The combined fictitious portion of the thermomechanical stress level (dashed line), and the residual stress field, $\bar{\rho}_{ij}$, are shown in Figure 2.3d. In order to satisfy Melan's theorem, the conditions must be met at all points of the loading cycle shown

in Figure 2.2b, including unloading. To determine whether this potential residual stress field satisfies Melan's theorem for all portions of the loading cycle, conditions at the other loading extreme (unloading) are also checked. The shakedown *limit* load (corresponding to the *maximum* allowable ΔT) is determined by the case where the residual stress field brings the point at $x = \pm L/2$ and $y = -t/2$ to the yield limit in tension upon thermally *unloading*. Upon thermally unloading, the stress distribution at the other critical location $x = \pm L/2$ and $y = -t/2$ is:

$$\sigma_{xx}(\pm\frac{L}{2}, \frac{-t}{2}) = \frac{PL^2}{2t^2} + \bar{\rho}_{ij}, \tag{2.5}$$

or, substituting Eq. (2.4) for $\bar{\rho}_{ij}$:

$$\sigma_{xx}(\pm\frac{L}{2}, \frac{-t}{2}) = \frac{PL^2}{2t^2} + \frac{PL^2}{2t^2} + E\alpha\Delta T - \sigma_o. \tag{2.6}$$

Again, to solve for the shakedown limit load, the stress at $x = \pm L/2$ and $y = -t/2$ should just reach yield in tension when thermally unloading, i.e. $PL^2/t^2 + E\alpha\Delta T - \sigma_o = \sigma_o$ or, rearranging:

$$\frac{PL^2}{t^2} + E\alpha\Delta T = 2\sigma_o. \tag{2.7}$$

Analytical Bree load interaction diagram (small displacements)

Elastic and shakedown limits determined using the direct analytical method are given in Figure 2.4. In this figure the normalized pressure load, P/P_o is shown along the ordinate; P_o is the uniform pressure magnitude that would initiate yielding of the built-in beam in the absence of the thermal load. The normalized thermal load, $\Delta T/\Delta T_0$, is shown along the abscissa; ΔT_o denotes the thermal load magnitude that would initiate yielding of the built-in beam in the absence of the pressure load.

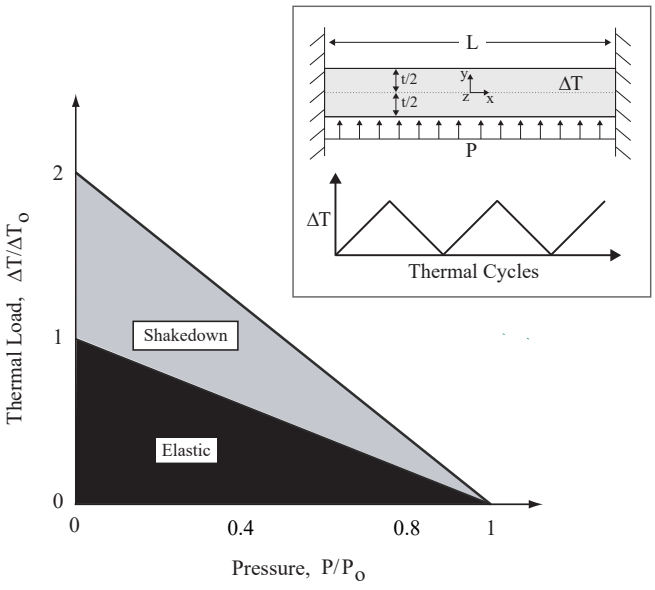

Figure 2.4: *Analytical elastic and shakedown limits of the built-in beam.*

In Figure 2.4, both the elastic and shakedown limits decrease with increasing steady distributed load (P). The areas below the limit lines indicate feasible design space based on elastic and shakedown behaviors. Allowing for shakedown behavior doubles the feasible design space when compared to yield-limited design.

Numerical shakedown limit determination via step-by-step analysis

In order to aid in interpretation of the analytical Bree load-interaction diagram, the built-in beam shown in Figure 2.2 was also modeled using the commercial finite element software Abaqus 6.14-1, (SIMULIA, Providence, RI). The beam was constrained from translation and rotation at the walls to simulate clamped boundary conditions. Only a half span of the beam was modeled by defining symmetry along the axis of the beam using planar B21 elements. A mesh sensitivity analysis was performed which identified that 200 elements along the beam was sufficient. Elastic-perfectly plastic behavior was assumed with the mechanical properties given in Section 2.1 for Inconel 718 nickel-based superalloys at an elevated reference tem-

perature.

The thermomechanical loading shown in Figure 2.2b was applied in the finite element model in two consecutive analysis steps. In the first step, a uniform pressure of $P = 0.1\ MPa$ ($P/P_o = 0.08$ for $L/t = 40$) was applied over the beam. The uniform temperature of the beam was cycled between the reference value and the maximum temperature in the second analysis step. It was found that 10 thermal cycles were sufficient to identify the nature of the elastoplastic behavior (elastic, shakedown or other inadmissible elastoplastic behavior). Under the thermomechanical loading detailed above, plastic strain localizes at the walls. The time evolution of the plastic strain at these critical points was monitored in the second analysis step to identify the elastoplastic behavior of the beam. As the applied pressure is low (well within the elastic regime for most aerospace materials), the structure displays elastic, shakedown, or inadmissible behaviors depending on the magnitude of the cyclic thermal load.

In order to visualize the distribution of plastic strains under this type of loading, a 2D finite element model was used under plane stress assumptions. Note that although only plane stress results are shown here, plane strain assumptions give similar strain distributions with larger magnitudes. Figure 2.5 shows the distribution of equivalent plastic strain (PEEQ) in the half-beam upon applying the last thermal cycle at a level that causes the structure to experience ratchetting. The contour plot reveals the critical locations in the beam under the thermomechanical loading applied. The critical locations are the top corners of the beam where both thermal and mechanical loads cause compressive stresses.

Post-processing of the numerical simulations and identification of the elastoplastic behavior is summarized below with the examples of shakedown (Figure 2.6a,b) and other undesirable (inadmissible) responses (Figure 2.6c,d). Note that in these numerical examples, shakedown is determined by monitoring the full cyclic elasto-

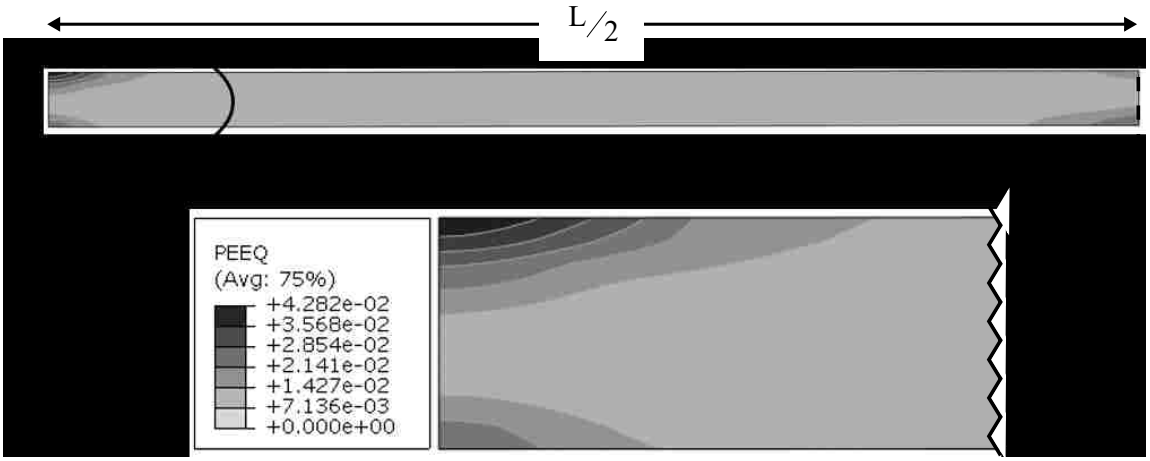

Figure 2.5: *Equivalent plastic strain distribution of a beam under a uniform pressure of* $P = 0.1\ MPa$ *and thermal load of* $\alpha\Delta T = 9.4 \times 10^{-3}$.

plastic response without the application of direct method shakedown theorems as is done in Section 2.1.1.

In the case of shakedown (Figure 2.6a,b), the magnitude of the plastic strain developed at the end of the first thermal cycle remains constant (stabilizes) and elastic behavior is recovered for the beam upon further thermal cycles. This behavior is shown in Figures 2.6a,b where the axial stress-strain response and the equivalent plastic strain (PEEQ) during the thermal cycles are plotted. In the axial stress-strain plot (Figure 2.6a), response during the first cycle is indicated and further triangle markers show the behavior during the rest of the 9 thermal cycles. In Figure 2.6a, the axial plastic strain at the critical points (at the walls) remains constant after the first cycle while the axial stress varies between the maximum and minimum values shown. The magnitude of the PEEQ in Figure 2.6b remains constant for thermal cycles 2-10, indicating shakedown and the recovery of elastic behavior.

An example of an undesirable elastoplastic response (alternating plasticity, ratchetting or collapse) that occurs if the thermal load exceeds the shakedown limit of the structure is shown in Figures 2.6c,d. In the axial stress-strain plot (Figure 2.6c), the response at the critical points (at the walls) in the first thermal cycle is identified.

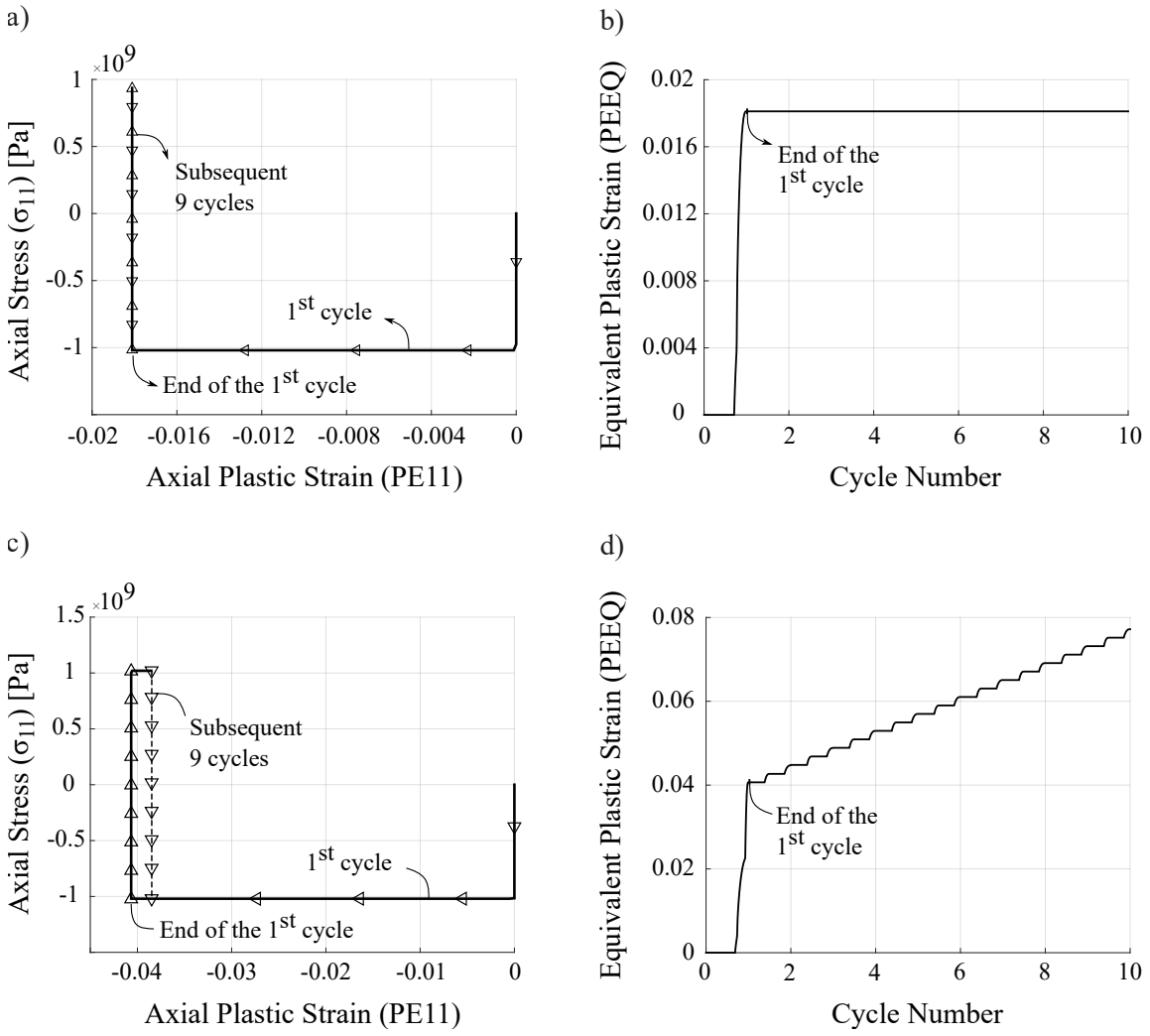

Figure 2.6: *a) and c) Axial stress and axial plastic strain response, b) and d) equivalent plastic strain (PEEQ) evolution during the 10 thermal cycles. The plots depict the response of the top corner at the walls of a built-in beam (Figure 2.2b) with an aspect ratio of* $L/t = 40$ *and a uniform pressure of* $P = 0.1\ MPa$*, which corresponds to* $P/P_o = 0.08$*. Material properties of Inconel 718 at an elevated reference temperature were used. The thermal load is below the shakedown limit (*$\alpha\Delta T = 7.2 \times 10^{-3}$*) for (a,b) and above the shakedown limit (*$\alpha\Delta T = 9.4 \times 10^{-3}$*) for (c,d).*

Upon heating the beam in the first cycle, the axial stress at the critical point reaches the yield stress in compression and initiates local plastic strains. When the thermal load is removed, the axial stress reaches yield in tension, changing the sign of the axial plastic strain. During subsequent thermal cycles, the axial plastic strain varies between two values of equal magnitude but opposite sign. As a result, there is no

net plastic strain and this represents alternating plasticity behavior which can lead to low cycle fatigue. In contrast, PEEQ, the equivalent plastic strain, at the critical points at the walls, remains a positive scalar and continues to accrue with thermal cycling in Figure 2.6d.

Numerical Bree load-interaction diagram (small displacements)

A numerical Bree interaction diagram (Figure 2.7) for the structure shown in Figure 2.2b was developed using the finite element model and procedure outlined in Section 2.1.1. An example Abaqus input file code for this type of analysis is given in Section 1 of the Supplemental File submitted with this dissertation. For each beam geometry considered, the procedure is repeated for increasing thermal load levels (ΔT) with increments of 10 $^{\circ}C$ until the first-yield and shakedown limits of the structure were identified. This numerical map is used for comparison with the analytical solutions presented in Section 2.1.1. For a better comparison with the analytical model, first only beams with small aspect ratios ($L/t < 25$) are considered. Then, the shakedown limits fore beams with increasing aspect ratios are investigated to show the effect of slenderness on the results.

This numerical map is used for comparison with the analytical solutions presented in Section 2.1.1. The axes of this interaction diagram are the same as described in Figure 2.4 in Section 2.1.1. The analytical elastic limit (Eq. (2.2)) is plotted as a solid red line and the lower bound shakedown limit (Eq. (2.7)) is plotted as a dashed black line in the diagram. The thermal loads, determined numerically, that cause first yield, shakedown or inadmissible elastoplastic behaviors (alternating plasticity, ratchetting) are shown in Figure 2.7. Open circles indicate FEA cases that are fully elastic, grey circles indicate cases that shakedown, black circles indicate cases that experience either alternating plasticity or ratcheting (inadmissible).

Figure 2.7 shows good agreement between the analytic limits and the numerical

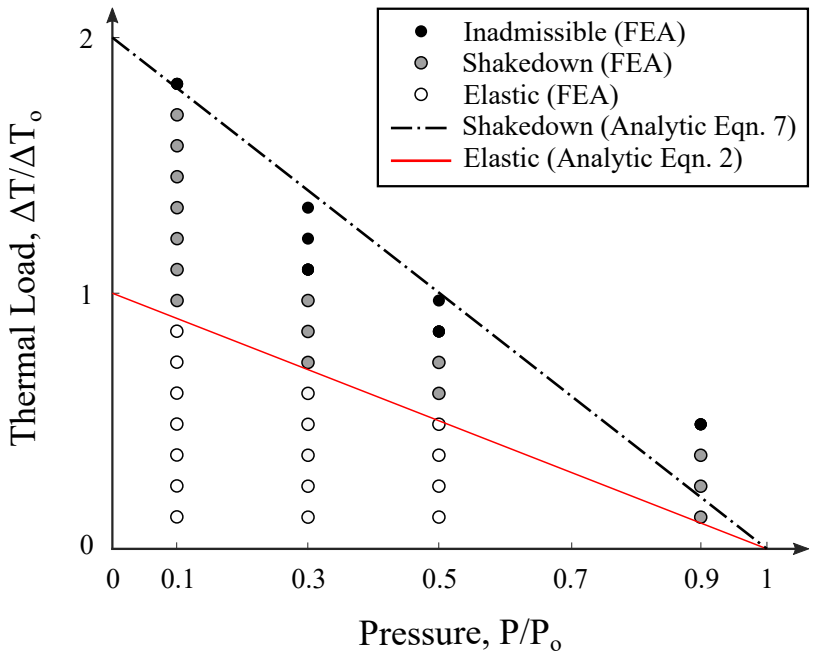

Figure 2.7: *Regime map, based on FEA computations assuming small displacements, illustrating cyclic elastoplastic behaviors. Open circles indicate cases that are fully elastic, grey circles indicate cases that shakedown, black circles indicate cases that experience either alternating plasticity or ratcheting (inadmissible). For comparison, the dashed black line shows the analytic lower bound shakedown limit and solid red line shows the analytic elastic limit.*

results, especially with low uniform pressure (i.e. $P/P_o < 0.2$). The difference between analytical and FEA results increases at larger pressures. This discrepancy is associated with the simplifying assumptions of the analytical solution. Both methods in this map assume small displacements and neglects the possibility of buckling. However, while the analytical solution in Section 2.1.1 completely decouples the thermal and mechanical analysis, the FEA model does not. On the one hand, the thermal load applied in the analytical method creates only compressive stresses in the beam model. On the other hand, the thermal load applied in the second step of the FEA analysis contributes to the transverse displacements caused by the uniform pressure and creates additional bending stresses.

To better illustrate the influence of both geometric and material parameters, Figure 2.8 depicts the elastic, shakedown and buckling limit curves for a fixed pressure

level, $P = 0.1\ MPa$. The limit curves are presented in terms of thermal strain, $\alpha\Delta T$, and beam aspect ratio, L/t. Analytical elastic limits and shakedown limits for different materials are shown with solid and dashed curves, respectively. For reference, the purely elastic thermal buckling limit curve is superimposed on the figure. The thermal load, $\alpha\Delta T$, that would initiate thermal buckling is given by $\alpha\Delta T = \frac{1}{3}\left(\frac{\pi t}{L}\right)^2$. This equation is found by replacing the critical load in the Euler buckling equation of elastic buckling theory, $P_{cr} = 4\pi^2 EI/L^2$, with an equivalent thermal load using the relation, $E\alpha\Delta T_{cr} = P_{cr}/A$. The cross-sectional area of the beam is denoted by A and is equal to the thickness, $A = t$, when a unity beam depth is assumed. The elastic thermal buckling constraint depends only on the beam aspect ratio and it is shown as a thick solid line. The ratios of Young's modulus and yield strength are representative of nickel-based superalloy Inconel 718 ($\varepsilon_o = 0.59\%$), Inconel 625 ($\varepsilon_o = 0.26\%$) and some other nickel and copper alloys ($\varepsilon_o = 0.1\%$) at an elevated reference temperature of $600°C$. Note that this level of pressure, $P = 0.1\ MPa$ corresponds to $P/P_o = 0.005$ for $L/t = 10$, $P/P_o = 0.12$ for $L/t = 50$ and, $P/P_o = 0.5$ for $L/t = 100$, when the properties of Inconel 718 ($\varepsilon_o = 0.59\%$) are used. It is again seen that, depending on material, geometry and loading, elastic thermal buckling may be initiated before either initial yielding or shakedown limits are reached.

In order to compare these small deformation based analytic calculations with FEA results, a parametric study was performed. Numerical elastic and shakedown FEA limits were found assuming material properties representative of Inconel 718 nickel-based superalloys at an elevated reference temperature of $600°C$ and shown in Figure 2.8. In order to compare with the small deformation analytical approach, geometric nonlinearity was neglected in the FE model. The numerical elastic limit agrees well with the analytic solution. For the shakedown limit, the numerical solution diverges from the analytic solution especially at large aspect ratios ($L/t > 50$).

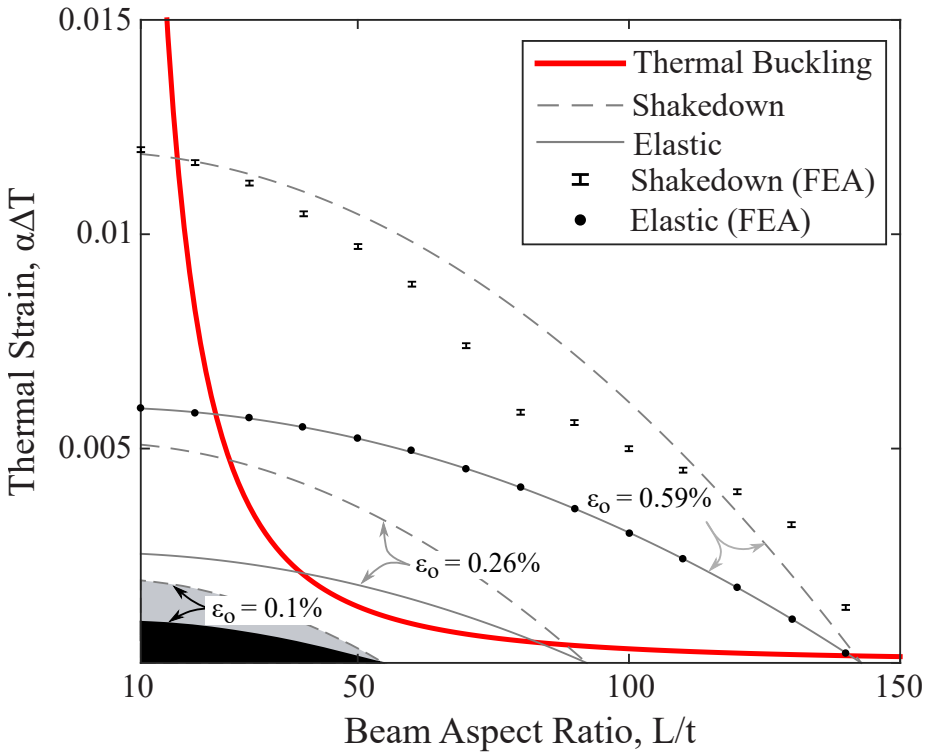

Figure 2.8: *Consideration of elastic thermal buckling, elastic and shakedown limits for a built-in beam subjected to* $P = 0.1$ *MPa uniform pressure. Limits for several types of aerospace materials with representative properties are given (nickel-based superalloys Inconel 718* ($\varepsilon_o = 0.59\%$)*, Inconel 625* ($\varepsilon_o = 0.26\%$) *and, other nickel and copper alloys* ($\varepsilon_o = 0.1\%$)*. Note that these ratios were determined with properties at a reference elevated temperature of* $600°C$*.*

The stress/displacement response of the beam in the FE analysis differs from the analytic solution after local yielding initiates. This can be attributed to a loss of stiffness followed by more pronounced displacements when local yielding of the beam occurs at the walls. This effects the shakedown limit of beams with small and large aspect ratios differently. For large aspect ratios, the thermomechanical loading creates compressive stresses throughout the critical cross sections, while for small aspect ratios, the loading causes a stress distribution that varies from compressive stress at the top corners to tensile stress at the bottom corners of the critical cross sections.

Similar to Figure 2.8, Figures 2.9a,b show the analytic elastic buckling, first-yield (E) and shakedown (SD) limits of clamped and pinned beams and compares

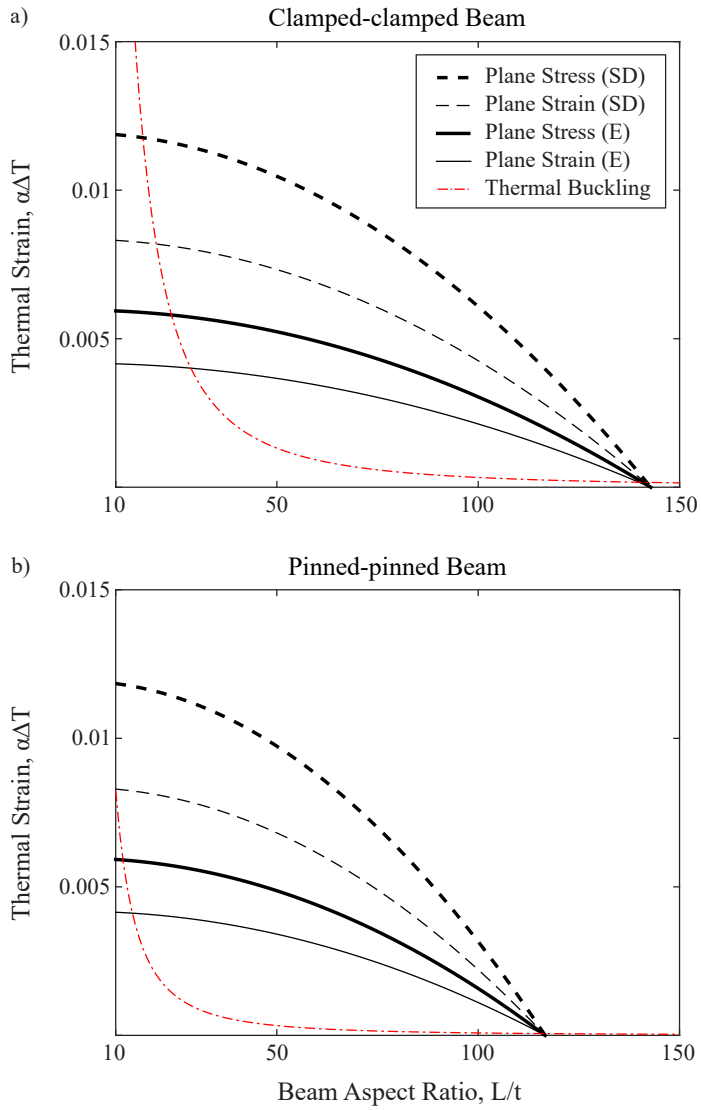

Figure 2.9: *First-yield (E), shakedown (SD) and elastic thermal buckling limits for a) clamped beams, b) pinned beams subject to* $P = 0.1\ MPa$ *(*$P/P_o = 0.005$ *for* $L/t = 10$*,* $P/P_o = 0.12$ *for* $L/t = 50$*,* $P/P_o = 0.5$ *for* $L/t = 100$*). Various aspect ratios for plane stress and plane strain assumptions are used with properties of Inconel 718 at an elevated reference temperature (*$\varepsilon_o = 0.59\%$*). Note that Figure 2.8 used plane stress conditions for the clamped beam but employed different materials.*

the limits when plane stress or plane strain assumptions are used for the $\varepsilon_o = 0.59\%$ material (Inconel 718). The limit equations are listed in Table 2.1 and derivations are given in Appendices A.1 and A.2. Note that the limits for $\varepsilon_o = 0.59\%$ in Figure 2.8 correspond exactly to the plane stress limit curves in Figure 2.9a. For both types of boundary conditions, plane stress assumptions result in higher elastic and shakedown

Table 2.1: *Elastic and shakedown limits for clamped and pinned beams under plane stress and plane strain conditions.*

Clamped Beam		
	Elastic Limit	Shakedown Limit
Plane Stress	$\frac{PL^2}{t^2} + 2E\alpha\Delta T = 2\sigma_o$	$\frac{PL^2}{t^2} + E\alpha\Delta T = 2\sigma_o$
Plane Strain	$\frac{PL^2}{t^2} + \frac{2E\alpha\Delta T}{1-\nu} = 2\sigma_o$	$\frac{PL^2}{t^2} + \frac{E\alpha\Delta T}{1-\nu} = 2\sigma_o$
Pinned Beam		
	Elastic Limit	Shakedown Limit
Plane Stress	$\frac{3PL^2}{4t^2} + E\alpha\Delta T = \sigma_o$	$\frac{3PL^2}{2t^2} + E\alpha\Delta T = 2\sigma_o$
Plane Strain	$\frac{3PL^2}{4t^2} + \frac{E\alpha\Delta T}{1-\nu} = \sigma_o$	$\frac{3PL^2}{2t^2} + \frac{E\alpha\Delta T}{1-\nu} = 2\sigma_o$

limits when compared to solutions under plane strain assumptions. Elastic buckling is initiated at smaller aspect ratios when plane stress assumptions are used. Beams with pinned constraints are susceptible to elastic buckling over a larger range of aspect ratios (Figure 2.9b). All of these results indicate that it may be crucial to investigate the effects of early elastic buckling on the shakedown performance and design of these structures.

Three main points that provide design guidance are identified based on Figures 2.8 and 2.9. When a small deformation analysis of the thermal and mechanical loading is adopted, without explicit interactions between buckling and shakedown, the absolute benefit of designing to shakedown decreases as the aspect ratio increases and the yield strain (ε_0) decreases. Thermal buckling becomes more relevant over a larger range of aspect ratios and at lower applied thermal strains as the yield strain of the material increases. Thermal buckling may take place before a material reaches the first yield or shakedown limits for some beam aspect ratios. In this way, geometry and material selection may be used to promote or suppress desired behaviors. The effect of aspect ratio on the shakedown performance is investigated further by allowing for large deformations due to thermal buckling in the following Section 2.1.2.

2.1.2 Case Study I-b: Built-in beam structure considering thermal buckling

The following numerical study investigates the shakedown performance of built-in beams with various aspect ratios. The beam thickness was kept constant at $t = 6\ mm$ and the beam length was changed to obtain aspect ratios between 10 and 40. The loading conditions detailed in Section 2.1 were applied in this numerical model. In the first analysis step, uniform pressure was applied over the beam. The uniform temperature of the beam was then cycled between the reference value and the maximum temperature in the second analysis step. For each beam geometry considered, the procedure is repeated for increasing thermal load levels (ΔT) with increments of 10 $^{\circ}C$ until the first-yield and shakedown limits of the structure were identified.

One key component of structural analysis for heated built-in beams (Figure 2.2) is the possibility of thermal buckling. Elastic buckling theory assumes that the beam is sufficiently slender, such that the dimensions of the beam cross-section are small compared to the beam length. If the slenderness ratio is sufficiently large, buckling will occur in the elastic range [51]. In order to investigate the effects of thermal buckling (elastic or plastic) on shakedown behavior, a numerical approach that includes the nonlinear geometrical effects is used for shakedown determination.

For each beam aspect ratio considered, a separate eigenvalue buckling analysis was performed. Deformation modes corresponding to the first buckling mode from the eigenvalue analysis were imposed as initial imperfections before analyzing the elastoplastic behavior. The magnitude of the initial imperfections were set such that the maximum displacements were approximately 3% of the beam thickness. Imperfection magnitudes from 2% to 5% were evaluated and no effect on the shakedown results was seen. Examples of Abaqus input file codes for both imperfection analysis

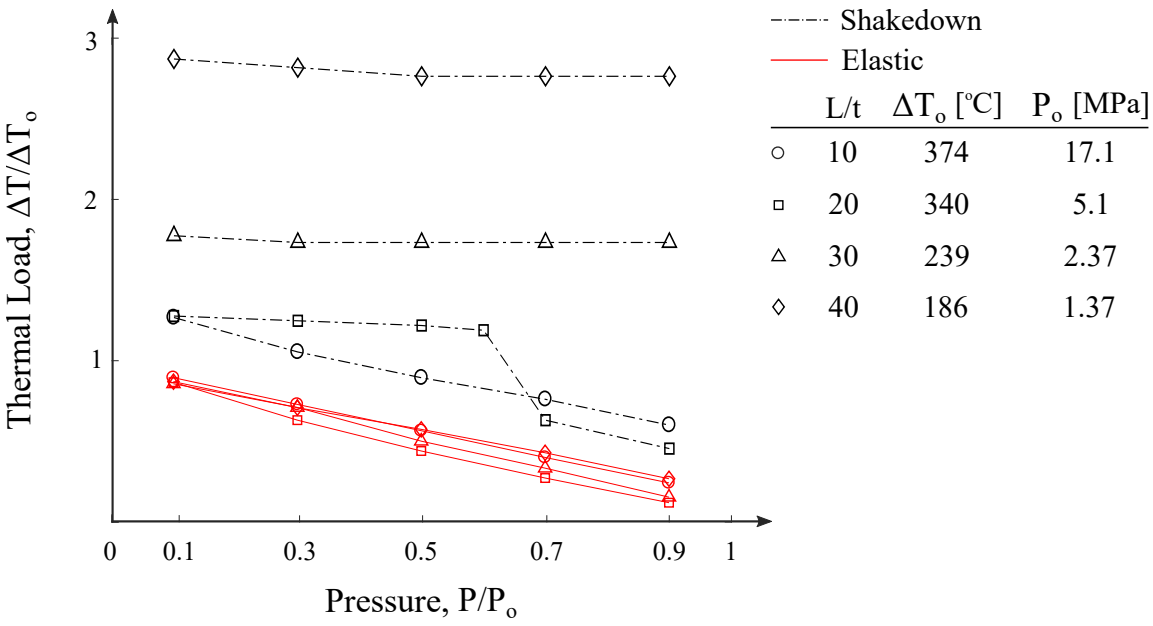

Figure 2.10: *Regime map, based on FEA computations, illustrating cyclic elastoplastic behaviors as a function of normalized thermal and mechanical loading. This diagram indicates the feasible thermomechanical loading domains below the elastic and shakedown limit lines. Black dashed lines indicate shakedown limits and red solid lines indicate elastic limits for beams with various aspect ratios.*

and shakedown analysis are given in Sections 2.1 and 2.2 of the Supplemental File submitted with this dissertation.

Based on these loading and geometric conditions, cyclic plasticity regime maps (Figures 2.10 and 2.11) were created. In Figure 2.10, the normalized pressure load, P/P_o is shown along the ordinate and the normalized thermal load, $\Delta T/\Delta T_0$ is shown along the abscissa. Note that ΔT_o and P_o values are different for each beam aspect ratio and listed in the legend of Figure 2.10. Critical loading combinations for first yield and shakedown limits based on structures with aspect ratios of $L/t = 10$ (circles), $L/t = 20$ (squares), $L/t = 30$ (triangles) and $L/t = 40$ (diamonds) are shown. All of the elastic limits in these cases are depicted in red solid lines and the shakedown limits in black dashed lines. This diagram indicates the feasible thermomechanical loading domains below the elastic and shakedown limit lines.

The normalized shakedown limits change significantly with aspect ratio while the

elastic limits are all similar. Without imperfections and nonlinear geometry effects, all of the elastic limit lines, regardless of aspect ratio, would follow a line with a slope of -1 between the normalized thermal and pressure loads of 1. The minor variation in elastic limits shown in Figure 2.10 is due to the presence and interaction of imperfections and pressure loading. Figure 2.10 shows that for all of the beam aspect ratios considered, shakedown behavior enlarges the feasible design space that is determined by first yield.

The benefit of shakedown tends to increase with increasing aspect ratio. For example, at $P/P_0 = 0.5$, the allowable shakedown loadings for aspect ratios $L/t = 10, 20, 30, 40$ are 1.6, 2.8, 3.5, 4.8 times the elastic designs, respectively. At $L/t = 10$, there is no buckling before the shakedown load is reached. At $L/t = 20$ and 30, there is plastic buckling during the first thermal loading cycle before shakedown occurs. At $L/t = 40$, there is elastic buckling during the first thermal loading cycle before shakedown occurs. The apparent drop in the shakedown limit for aspect ratio $L/t = 20$ (between $P/P_0 = 0.5$ and 0.7) is due to the absence of thermal buckling. For example, buckling occurs at $P/P_0 = 0.5$ before the beam reaches the shakedown limit and after first-yield. The same is true for aspect ratio $L/t = 20$ at $P/P_0 = 0.6$. At these intermediate pressure levels, buckling occurs during thermal loading and postpones ratchetting. At the higher pressure level of $P/P_0 = 0.7$, the addition of thermal loading does not cause buckling. This reduces the allowable thermal loading for shakedown. As beams with large aspect ratios are more prone to thermal buckling and large deformations, these results suggest a relation between shakedown performance and nonlinear geometrical effects. This relation is further investigated in the following numerical study by analyzing beams with different aspect ratios under the same pressure loads.

Elastic, Shakedown and Buckling Behaviors as a Function of Aspect Ratio

A numerical interaction diagram for the structure shown in Figure 2.2b was developed using the finite element model and analysis procedure outlined in Section 2.1.2. Beams with aspect ratios from 10 to 50 were analyzed under a low pressure level of $P = 0.1\ MPa$ (corresponding to $P/P_o = 0.005$ for $L/t = 10$ and $P/P_o = 0.12$ for $L/t = 50$) and an intermediate pressure level of $P = 0.38\ MPa$ ($P/P_o = 0.022$ for $L/t = 10$ and $P/P_o = 0.4$ for $L/t = 50$). These uniform pressure values were chosen because the maximum stress they create for the beam with the largest aspect ratio is around 12% and 40% of the yield stress for the low and intermediate pressure levels, respectively.

The results of this numerical parametric study are summarized in the design map in Figure 2.11. For reference, the purely elastic thermal buckling limit curve is superimposed on the figure (thick grey dashed line). For both of the pressures analyzed, beams with small aspect ratio ($L/t \leq 20$) will yield without experiencing any buckling behaviors before shakedown. As the aspect ratio increases ($L/t = 25 - 35$), following first-yield, some plastic buckling was observed before shakedown limits were reached. The critical plastic buckling limits observed in the FE analyses were smaller than the elastic buckling limits. Plastic buckling only occured over a small range of aspect ratios ($L/t = 25 - 35$) and a plastic buckling limit line is not shown in Figure 2.11; instead, only the elastic thermal buckling limit is shown as a reference. At large aspect ratios ($L/t \geq 35$), elastic buckling occurs before yielding and shakedown. At low pressure, it was found that critical elastic buckling loads observed in the numerical FE analyses agreed well (within 10%) with the elastic buckling formula for the beams with large aspect ratios ($L/t \geq 35$).

Figure 2.11 also reveals the effect of buckling on elastoplastic shakedown behavior. The feasible design spaces are the areas below the elastic and shakedown limit

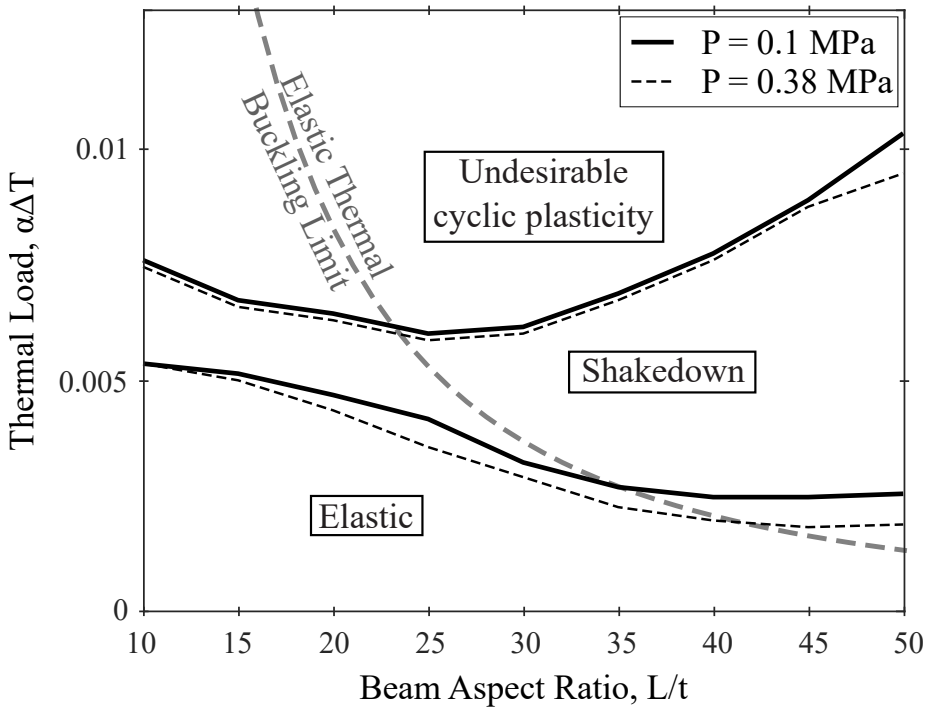

Figure 2.11: *Design map showing the fully coupled elastic, shakedown and buckling behaviors from FE analyses. Beams with various aspect ratios under $P = 0.1\ MPa$ and $P = 0.38\ MPa$ uniform pressure were analyzed. The analytic elastic thermal buckling limit is superimposed for reference indicating when buckling would occur before yielding or shakedown behaviors are reached. Material properties representative of the nickel-based superalloy Inconel 718 were used.*

curves. In the low aspect ratio portion of the map ($L/t \leq 20$), before onset of initial elastic thermal buckling, the elastic and shakedown limits decrease with increasing aspect ratio. This result is in agreement with the small deformation analytical limit curves shown in Figure 2.8 (see Section 2.1.1 for the analytical derivation) where the influence of buckling is not explicitly included in the analysis. However, for the beams with larger aspect ratios ($L/t \geq 35$), buckling can occur before the structure reaches either the elastic or shakedown limit. As a result of elastic buckling, the elastoplastic behavior changes drastically. The results suggest several consequences of elastic buckling.

Following elastic thermal buckling at higher aspect ratio values ($L/t \geq 35$ for both $P = 0.1$ and $P = 0.38\ MPa$), for a given material, the elastic limit remains relatively

constant with increasing aspect ratio. In contrast, for this region of the design map, the shakedown limit continues to increase with increasing aspect ratio. The benefit of designing to shakedown increases as the aspect ratio increases (enlarged feasible design space).

Extended design domains may also translate to lightweighting gains, but the specific benefits depend on the material employed. As an example of weight reduction by allowing shakedown, we use the same material properties and low uniform pressure, $P = 0.1\ MPa$ from Figure 2.11 (Inconel 718, $E/\sigma_o = 168$). The mass of the structure can be calculated as $m = \rho L t$, per unit depth of the beam. The use of beam theory introduces the beam aspect ratio constraint, $L/t \geq 10$ and manufacturing constraints may impose minimum beam dimensions for the beam length, for example: $L \geq 4\ mm$ and beam thickness, $t \geq 0.3\ mm$. A reference mass for the beam can be determined using the minimum dimensions ($L_{min} = 4\ mm$ and $t_{min} = 0.3\ mm$), $W_{ref} = \rho L_{min} t_{min}$. If we assume a thermal load of $\alpha \Delta T = 5.3 \times 10^{-3}$, elastic design rules would dictate a beam with a greater thickness and a normalized weight of $W_{\substack{\text{elastic} \\ \text{design}}}/W_{ref} = 1.33$ (see Figure 2.11). Designing instead to shakedown would allow for a normalized weight of 1 which indicates a 33% reduction in weight when compared to traditional elastic design rules. These results again illustrate the advantages of designing to shakedown: incorporating shakedown in the design of beams enlarges the feasible design space and allows for lightweighting when compared to elastic designs.

Shakedown in the Post-buckled Regime

In order to better understand the conditions that improve the shakedown performance in the post-buckled regime, a sequentially coupled approach is outlined in the following. First, a buckled shape and the corresponding stresses induced by the geometric nonlinearity are determined using an analytical method summarized in B.

This analysis gives the transverse displacement and axial stress of a built-in beam as a function of thermal load and applied pressure for moderate rotations. In the following example, a low uniform pressure of $P = 0.1\ MPa$ is again assumed and the displacement/axial stress solution is obtained at the critical thermal buckling load. A finite element model was created and initialized with the analytically determined buckled shape (Eq. (B.5)). The model was also initialized with the stresses obtained analytically (Eq. (B.8)). As initializing a non-uniform stress field through the thickness of a beam element is not possible in the ABAQUS software; continuum plane stress (CPS4R) elements were instead used. Initial stresses were imposed on the finite element model with a user subroutine (SIGINI) available in ABAQUS. The initial temperature was set to the critical buckling load value.

Following the initialization of the finite element model with the analytic buckling solution, an additional Abaqus/Explicit step was used to further thermally cycle the beam under the constant pressure. In the first thermal cycle, the temperature was increased to a maximum value from the critical buckling temperature and then decreased to the reference temperature. In the subsequent loading cycles, the temperature was cycled between the reference level and the maximum value. Similar to the fully coupled analyses previously presented in this Section, the plastic strain evolution at the critical points of the beam, was monitored to determine if shakedown occurs.

This kind of sequential numerical approach can also be used to explore how the shakedown performance is affected by the stress/deformation due to thermal buckling. For example, by comparing results from sequential and fully coupled approaches, one can determine if thermal buckling that occurs before shakedown changes the shakedown limit compared to cases where these behaviors can occur simultaneously or otherwise. In order to make a better comparison between the fully coupled and sequentially coupled analyses, the fully coupled analysis from Section

2.1.2 was repeated using continuum elements for beams with aspect ratios of 40 and 50. It is found that continuum elements result in a less conservative (larger) shakedown limit load than the beam elements if a fully coupled approach is taken (Figure 2.12). Next, the sequential analysis was applied to the same two test case beams with aspect ratios 40 and 50. This was done at both a temperature below and a temperature above the shakedown limit determined by the fully coupled analysis with continuum elements.

All of the simulation results for these two test cases are shown in Figure 2.12. It is seen that the sequential analysis differs negligibly from the fully coupled analysis. The implication is that it is not necessary to include full coupling between buckling and elastoplastic behaviors to determine shakedown limits. This also suggests that using initially curved beams instead of straight beams may promote similar shakedown performance.

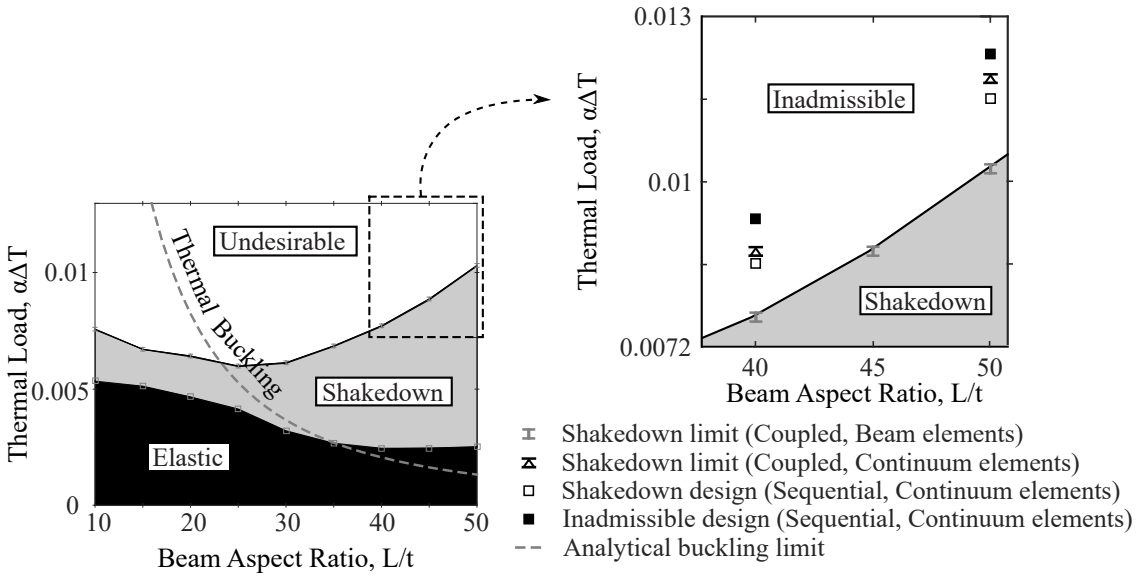

Figure 2.12: *Comparison of sequentially and fully coupled shakedown analyses. The figure on the left is a reproduction of Figure 2.11 ($P = 0.1\ MPa$ case only with the shakedown region highlighted in grey and elastic domain in black) to highlight the high aspect ratio region of the shakedown domain for investigation here. On the right, several cyclic thermomechanical FEA simulations are performed for two test cases ($L/t = 40, 50$) with the sequential and fully-coupled approaches. A uniform pressure of $P = 0.1\ MPa$ and Inconel 718 properties were assumed at an elevated reference temperature.*

Discussion of Case Study I: built-in beam

Based on the fully coupled numerical study in Section 2.1.2, the small deformation analytic design tools of Section 2.1.1 give overly conservative measures of shakedown benefits at higher aspect ratios where elastic thermal buckling is expected to occur before first-yield or shakedown. For the smaller aspect ratio beams that are not expected to buckle due to thermal loading, they may be used as a preliminary design step. For any material of interest and a given level of pressure, the value of what determines a large aspect ratio is defined by where elastic thermal buckling occurs before first yield and shakedown. For example, one could analytically construct Figures 2.9a,b for a case of interest to identify these large or small aspect ratio regions. For the remainder of this discussion, the terms smaller and larger aspect ratios refer to this definition.

For more accurate design, the fully coupled cyclic elastoplastic numerical procedure from Section 2.1.2 may be used as it is reliable for all ranges of aspect ratio, material conditions, and includes the potential for interactions between thermal buckling and shakedown. Figure 2.11 shows a practical application of the use of shakedown theory in the design of thermomechanical beams. The results suggest that conventional yield-limited designs are overly conservative. This is especially true for beam structures with large aspect ratios, which can withstand thermomechanical loads much larger than those identified by traditional yield-limited design. For example, the shakedown limits found for small aspect ratio beams were 1.4-1.9 times larger than the first-yield limits. This improvement increases to 2.5-4 times for large aspect ratio beams (Figure 2.11). For these larger aspect ratio beams, buckling relaxes the geometric constraint in the beam and allows the structure to shakedown at larger thermomechanical loads under cyclic loading conditions than without buckling present.

In applications where structures are allowed to operate in the post-buckling regime, designers can take advantage of this enhanced shakedown behavior by using large aspect ratios or by tailoring the material selection to promote thermal buckling. Alternatively, they could develop pre-service thermal treatments that promote thermal buckling. Lastly, similar shakedown design benefits may be obtained by using initially curved beams.

2.2 Case Study II: Auxetic structures

Materials and structures may show auxetic or negative Poisson's ratio behavior (expansion in tension and contraction in compression) due to their lattice structure and topology, respectively. Auxetic materials have been shown to exhibit excellent mechanical properties such as high shear resistance [52], fracture toughness [53], indentation resistance [54–57], and energy absorption [58–61]. Auxetic effects can be obtained in a structure made of a conventional material by arranging the topology such that the global behavior of the structure results in a negative Poisson's ratio. For example, auxetic structures can be obtained when mutually orthogonal periodic holes with large aspect ratios (length to width ratio) are made in plates/tubes [62]. Gas turbines contain several perforated components that are used for film cooling, as shown in Figure 2.13. Auxetic structures with holes are potential candidates for these components as they provide both the porosity required for the film cooling as well as the enhanced mechanical properties provided by the negative Poisson's ratio effects. Recently, it has been shown by Javid *et al.* that porous negative Poisson's ratio or "NPR" structures (Figure 2.13c) exhibit increased fatigue life when compared to conventional porous structures with circular holes [63].

As these types of gas turbine components typically serve under cyclic thermomechanical loading conditions, understanding their cyclic elastoplastic behavior may

lead to more weight-efficient design approaches. The cyclic inelastic behavior of auxetic structures has not previously been presented in the literature and is the focus of this section.

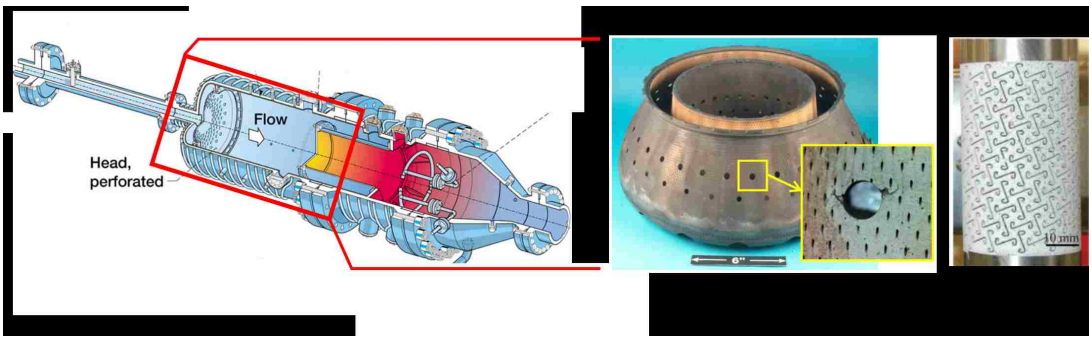

Figure 2.13: *Auxetic structure.*

2.2.1 Numerical shakedown analysis for auxetics

In order to investigate the shakedown behavior of auxetic structures, several geometries resulting in different degrees of negative Poisson's ratio are considered. Inspired by the recent work by Taylor *et al.* and Javid *et al.* [62, 63] a simple rectangular plate with mutually orthogonal periodic elliptical holes was used. Taylor *et al.* showed that the Poisson's ratio of such structures is directly related to the length of ligaments (l) separating neighboring holes shown (Figure 2.14) [62]. The governing length (l) (and thus also the Poisson's ratio) can be adjusted by varying the aspect ratio of the elliptical holes (a/b). In this study, three different geometries with various hole aspect ratios (a/b=30, 15, and 8) are analyzed numerically (Figure 2.14).

Finite element analyses for these structures were performed using the commercial software ABAQUS (Providence, Rhode Island). Although for gas turbine applications the loading is cyclic and thermomechanical, as a first analysis (and following Taylor et al. [62]), uniaxial mechanical-only cycles are investigated at ambient temperatures. For this first case, material properties that are representative of the

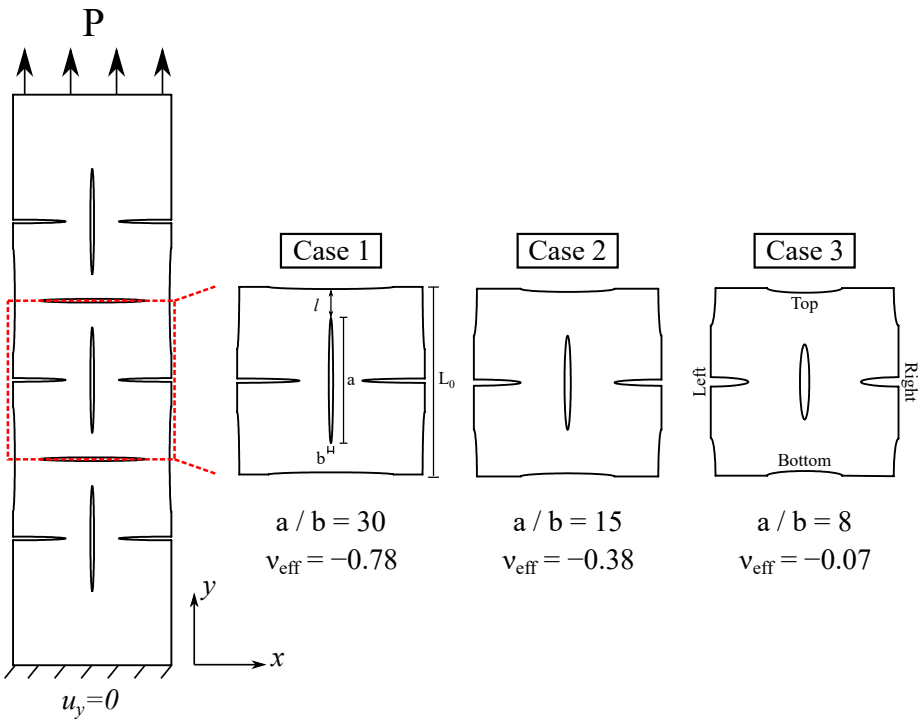

Figure 2.14: *Auxetic model and variations with different hole aspect ratios resulting in different levels of negative Poisson's ratio.*

6061 aluminum alloy at ambient were used assuming elastic-perfectly-plastic behavior ($E = 70\ GPa$, $\sigma_0 = 275\ MPa$). Due to the relatively sharp vertices of the elliptical holes, especially in the case of the largest aspect ratio ($a/b = 30$), stress concentrations occur near the hole tips. This requires fine mesh near the regions prone to stress concentrations. However, uniformly reducing the mesh size in the entire structure yields an excessively large model and large calculation times. To overcome this problem, an adaptive mesh process available in the Abaqus software was used. This method adaptively remeshes the geometry with the aim of creating a mesh-independent model with the least number of elements. As an example, the convergence of the maximum von-Mises stress and maximum equivalent plastic strain in the $a/b = 30$ model under a tensile stress 1.3 times the load causing first-yield is shown in Figure 2.15.

Upon completion of the mesh adaptivity process, a model with fine mesh near the

stress concentration regions and a coarse mesh in the regions where the stresses and strain are non-critical was achieved. The adapted mesh for case #1 with $a/b = 30$ is shown in Figure 2.16. A total of approximately 100,000 elements were used in this model. A similar mesh adaptivity procedure was used for the other structures with $a/b = 8$ and 15, but results are not shown here as the stress concentrations in these model are not as severe as the model with $a/b = 30$. In Figure 2.16, the detailed mesh discretization on the right gives a close-up view of the inner surface of the elliptical vertex.

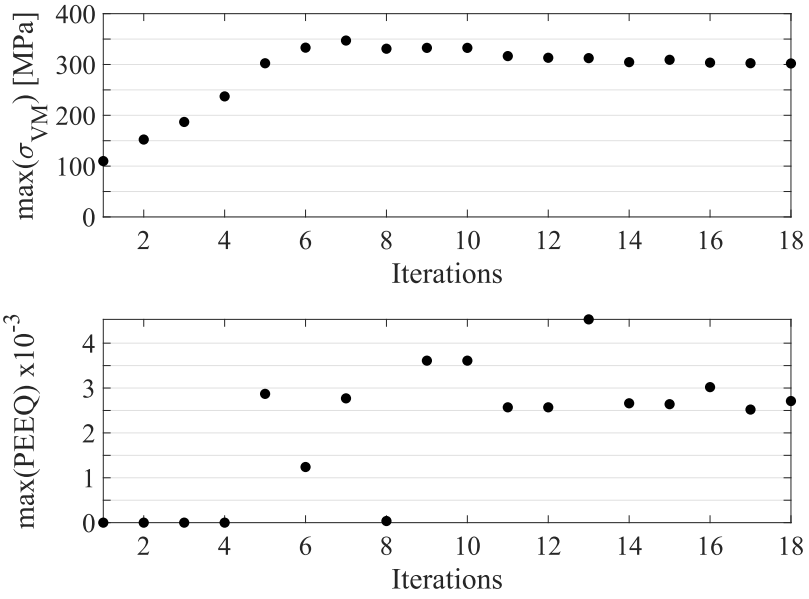

Figure 2.15: *Mesh convergence during the mesh adaptivity process for the auxetic case #1 with* $a/b = 30$.

Following Taylor *et al.* [62], each model was analyzed under cyclic tensile loading between zero and a maximum value that would exceed the material yield limit. The tensile load was applied in terms of a pressure (P) on the top surface of the model while a displacement boundary condition was applied at the bottom surface, constraining the vertical degree of freedom (Figure 2.14). Using this model, first the elastic limit (tensile load that causes first yield) was found for each case ($a/b = 8$, 15, 30). The evolution of the plastic strain within the structure was then moni-

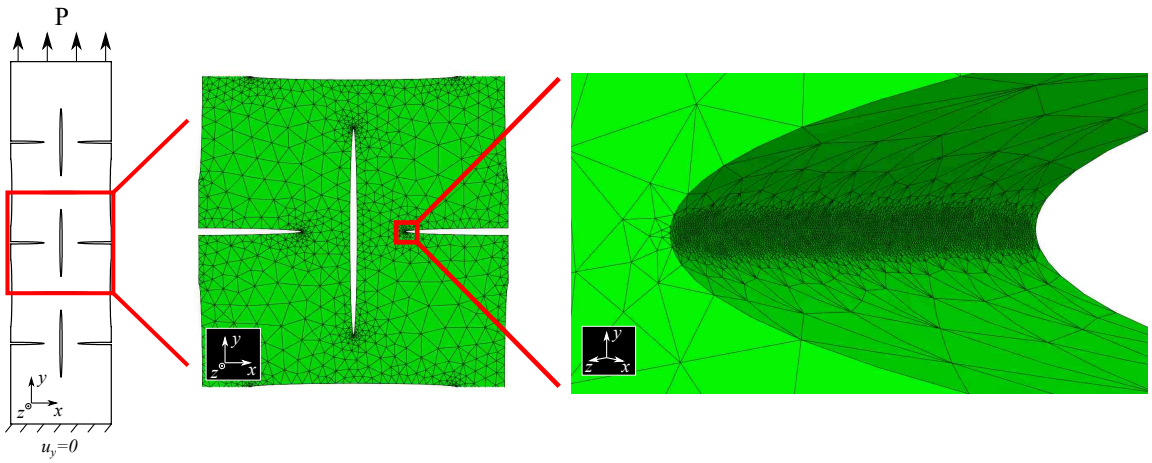

Figure 2.16: *Details of the mesh discretization of the structure with* $a/b = 30$.

tored during 10 cycles, and the nature of the elastoplastic behavior was determined (shakedown or ratchetting). The magnitude of the tensile loading on the structures was incrementally increased in a parametric study to determine the shakedown limit (the largest loading magnitude that causes shakedown behavior). Note that in this example, the plastic strain accumulation upon cycling does not arrest but instead dramatically reduces. Hence, an allowable plastic strain per cycle criterion is needed to identify effective shakedown behavior. For this limit analysis a plastic strain accumulation threshold of 10^{-6} per cycle was assumed for the shakedown behavior. The choice of this strain accumulation threshold will be further discussed in Chapter 4, Section 4.2.

In order to study the interaction between shakedown performance and auxeticity, an effective Poisson's ratio was calculated for each geometry following a similar method employed by Taylor *et al.* [62].

$$\nu_{eff} = -\frac{\bar{\epsilon}_{xx}}{\bar{\epsilon}_{yy}}, \tag{2.8}$$

where $\bar{\epsilon}_{xx}$ and $\bar{\epsilon}_{yy}$ are expansion of the unit geometry (Figure 2.14) in the horizontal

(x) and vertical (y) directions under tensile loading:

$$\bar{\epsilon}_{xx} = \frac{\bar{u}_x^R - \bar{u}_x^L}{L_0}, \quad \bar{\epsilon}_{yy} = \frac{\bar{u}_y^T - \bar{u}_y^B}{L_0}. \tag{2.9}$$

L_0 is the length of the unit cell, $\bar{u}_x$ and $\bar{u}_y$ are the average displacements in the horizontal and vertical directions of the nodes on the right (R), left (L), top (T), and bottom (B) edges of the unit cell highlighted in Figure 2.14.

2.2.2 Results of the numerical shakedown analysis for auxetics

A representative contour plot of horizontal (1-direction) displacements obtained under tensile loading (upon reaching the yield limit) for the structure with $a/b = 30$ is shown in Figure 2.17 on the undeformed geometry. The applied tensile loading results in horizontal (1-direction) expansion of the structure in the middle section, causing a negative Poisson's ratio effect. Following the method explained in Section 2.2.1 and using Equations 2.8 and 2.9, an effective Poisson's ratio (ν_{eff}) was calculated for all three structures ($a/b = 8, 15$ and 30) at the different tensile loads causing first-yield in each structure. The calculated effective Poisson's ratios vary between -0.07 and -0.78 (Figure 2.14, Table 2.2). Recall that the possible values for Poisson's ratio for linear elastic materials range between -1 and +0.5. Elastic and shakedown limits were determined for each structure following the procedure detailed in Section 2.2.1. The effective Poisson's ratio, elastic limit, and shakedown limits obtained numerically are listed in Table 2.2.

Elastic and shakedown limits are plotted against the effective Poisson's ratio in order to identify possible trends (Figure 2.18a). In this figure, the elastic and shakedown limits are shown with circle and square simulation markers, respectively. Figure 2.18b shows the normalized elastic and shakedown limits as a function of the effective

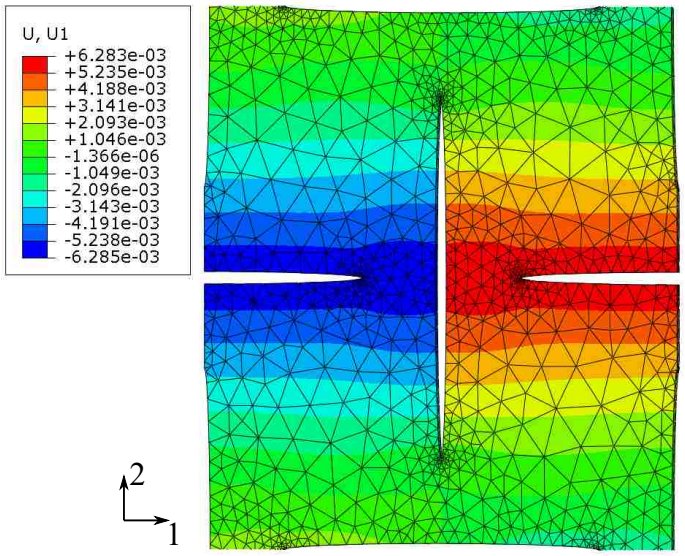

Figure 2.17: *Displacement in the horizontal direction shown for the central unit cell of the model with $a/b = 30$, for the loading level that causes first-yield in the structure.*

Poisson's ratio. In this figure, the limits for each structure were normalized by the individual elastic limit (Table 2.2) corresponding to each geometry case (resulting in a normalized elastic limit of 1 for all of the structures).

The results in Figure 2.18a show that both elastic and shakedown limits decrease with larger negative Poisson's ratios. This outcome can be explained by the reduction of the x-y planar cross-section with increasing hole aspect ratios (Figure 2.14). Regardless, for all three of the effective Poisson's ratios explored, the shakedown limit was found to be significantly larger than the elastic limit. While the absolute shakedown limit decreased with increasing auxeticity, the normalized shakedown limit in Figure 2.18b, which is more relevant for design purposes, is found to be independent of the effective Poisson's ratio and approximately twice the elastic limit for all structures. These promising preliminary results serve as motivation for future numerical and experimental investigations that will include thermal effects.

Table 2.2: *Poisson's ratio, elastic limit and shakedown limit results for the structures with* $a/b = 8, 15$ *and* 30.

a/b	8	15	30
Effective Poisson's ratio	-0.07	-0.38	-0.78
Elastic limit [MPa]	9.60	4.00	1.12
Shakedown limit [MPa]	19.20	7.80	2.20

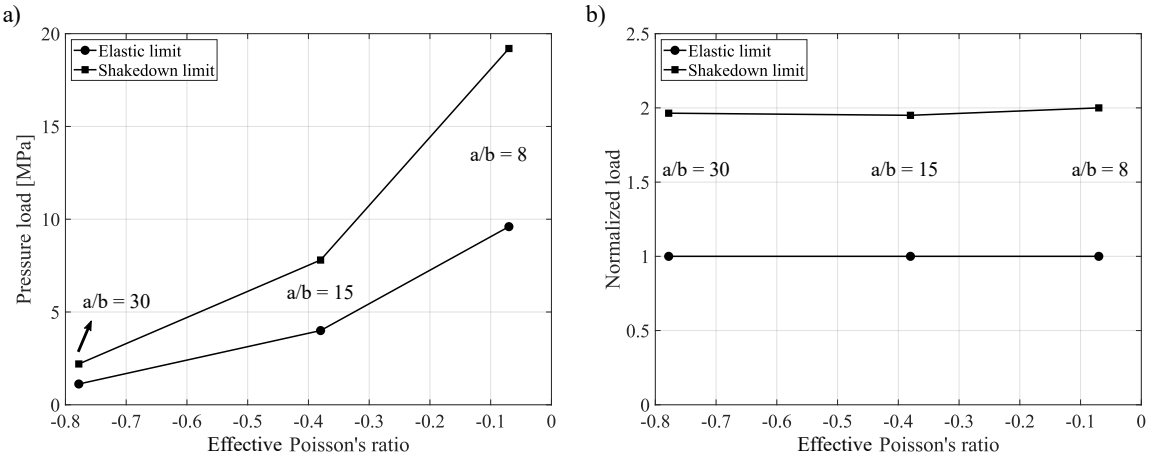

Figure 2.18: *Numerical results for the elastic ans shakedown limits of the auxetic structures.*

2.3 Case Study III: Reinforced concrete structures

Evaluating the resilience (safety load factors, ultimate load-bearing capacity) of reinforced structures (Figure 2.19) under elevated temperatures representative of fire conditions is critical for many civil applications. Attention has been focused on the determination of axial force-bending moment interaction diagrams of reinforced concrete structures subjected to a fire-induced temperature gradients using specialized step-by-step finite element analysis codes. Shakedown-based analysis has recently been shown to offer a rigorous framework for determining safe load bearing capacities, including under fire conditions [64, 65].

In general, few studies have investigated the shakedown behavior of reinforced-concrete (RC) structures [64–71]. Alawdin and Bulanov conducted a numerical study for the load bearing capacity of RC structures under a vertical dead load and ran-

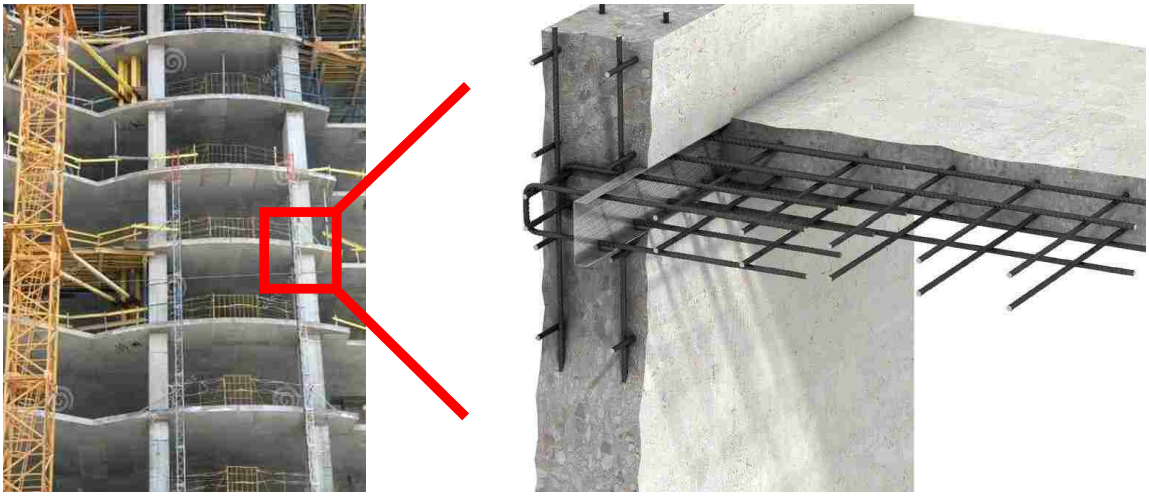

Figure 2.19: *Reinforcement bars inside a concrete structure.*

domly varying, horizontal mechanical loads, using an optimization scheme which accounts for fracture of members [68]. In another study, Alawdin and Liepa investigated optimal reinforcement cross-sectional areas and member sizing using an optimization approach based on shakedown design limits [69]. Very few have explored the shakedown response of RC structures under thermomechanical loads [64, 65]. Bleyer et al. developed a lower bound direct shakedown method to investigate the load bearing capacity of reinforced concrete slabs under fire conditions [65]. The authors showed the evolution of thermomechanical load interaction diagrams with different fire temperature fields.

Building on these studies, here a greater understanding of the RC shakedown behavior under multi-axial thermomechanical loadings is sought. In this section, a step-by-step numerical finite element analysis (FEA) study is used to explore and demonstrate shakedown behavior of a RC structure under a combination of four-point bending loads and fire conditions. The goal is to further support shakedown design strategies for RC components under extreme thermomechanical loadings.

2.3.1 Numerical shakedown analysis for RC structures

The commercial FEA code ABAQUS (Providence, Rhode Island) was used to simulate and understand the cyclic response of RC structures under thermomechanical loading. The slab model is based on a test-case available in the ABAQUS benchmark documentation. This ABAQUS benchmark problem was for simulating smeared cracking of a RC structure under mechanical-only loads. It was modified by adding thermal loading that represents fire conditions to allow for some initial exploratory shakedown analysis of RC structures. Figure 2.20 shows a schematic of the RC slab of interest from a side view (bottom illustration) and top view (top illustration). The dashed lines indicate the placement of the reinforcement bars. Thermechanical loading, dimensions and boundary conditions are also shown. The model (see Figure 2.20) employed S4R type shell elements with 10 elements along the beam length (762 mm) and 2 elements for the width of the beam (457 mm). Based on a sensitivity study (not shown), it was found that this was sufficient to guarantee that the results are not mesh dependent. The cross-section of the slab was modeled using 9 section points. Symmetry of the problem allows half of the beam to be modeled (symmetry in x-direction, 381 mm).

Material properties shown in Table 2.3 were assigned to the rebars and the concrete cover. Interaction between the concrete and rebar, and loss of concrete stiffness during cracking were modeled by adding tension stiffening to the concrete properties through a built-in function available in ABAQUS (Abaqus Analysis User's Manual, Section 20.6.3 Concrete damage plasticity, [72]). A linear reduction in the tensile strength of concrete beyond the cracking failure limit was assumed (Table 2.3). Since the behavior of the structure is dominated by the tensile cracking of the slab, the cracking model neglects failure in compression by allowing unlimited strength in compression. An elastic-perfectly-plastic material model was assumed for the re-

bars with no hardening after yielding. The rebar properties given in Table 2.3 are representative of ambient properties. Temperature dependence of the Young's modulus and yield stress for rebar was included in the model based on the guidelines in Eurocode 1 [73].

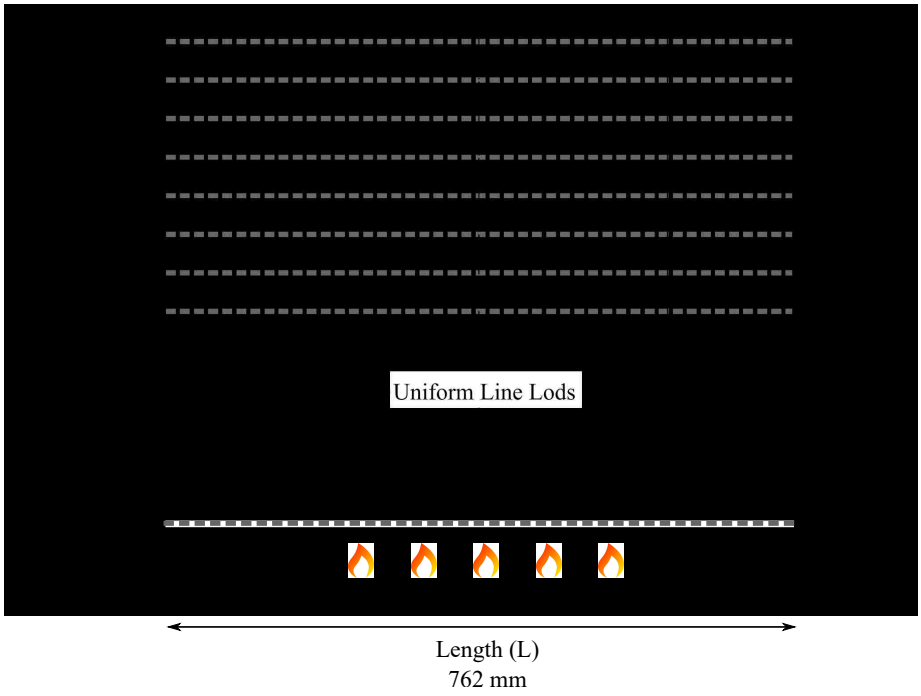

Figure 2.20: *Reinforced concrete slab model, boundary conditions and bending loads.*

A combined thermomechanical load was applied in the model. The mechanical load is a constant and uniform line load as shown in Figure 2.20. A cyclic temperature gradient through the thickness (y-direction, Figure 2.20) was applied to the RC slab. For the thermal load, a representative temperature distribution was obtained from a separate heat transfer analysis in ABAQUS. For this heat transfer model, the slab cross-section was subjected to fire conditions for 8 hours as specified by Eurocode 1 [73]. In particular, convection and radiation at the bottom surface of the slab that is exposed to fire and the top surface that is exposed to ambient conditions were included to determine a representative thermal gradient in the case of fully developed fire (as schematically shown in Figure 2.21). The convective heat transfer coefficients

($h_{c,a} = 4\ W/m^2K$ and $h_{c,f} = 25\ W/m^2K$ for the surfaces exposed to ambient and fire conditions, respectively), and surface emissivity ($\varepsilon_m = 0.8$) are also indicated in Figure 2.21. An example Abaqus input file code for this type of analysis is given in Section 3 of the Supplemental File submitted with this dissertation. The resulting reduction of the temperature through the thickness with respect to distance from the bottom surface is shown in Figure 2.22. This temperature gradient is assumed to be consistent along the length (L) and width (w) of the slab.

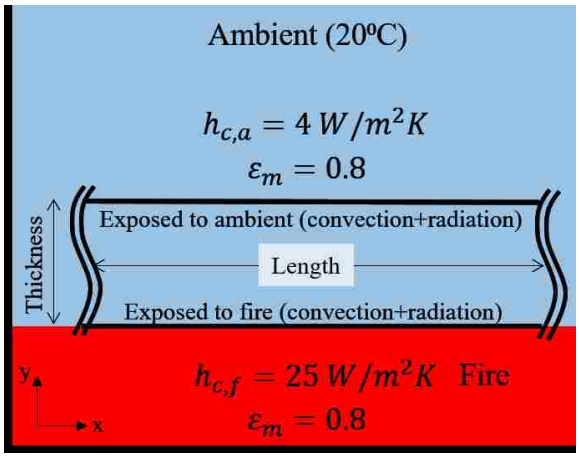

Figure 2.21: *Heat transfer analysis model used to obtain thermal distribution.*

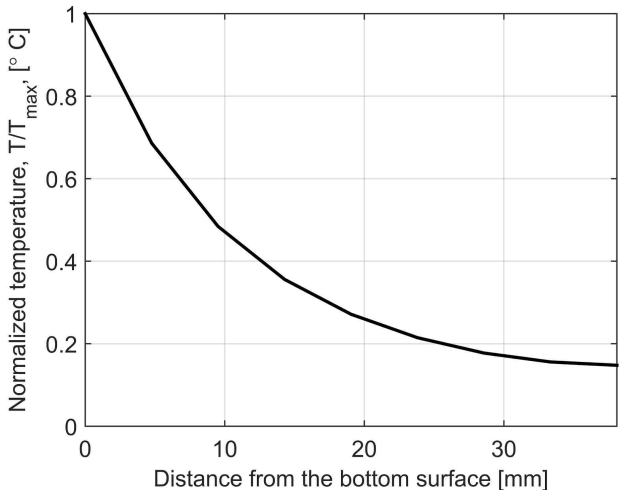

Figure 2.22: *Nonlinear temperature gradient through the thickness obtained by the heat transfer analysis. Note that the bottom surface is the one impinged by the fire.*

Full cyclic elastoplastic analyses were performed at various force levels and under the same thermal distribution (as Figure 2.22) with a maximum temperature value of 300^{o}C. This maximum temperature was chosen as a threshold that does not cause an excessive stiffness loss for the rebars (Young's modulus and yield stress degrades 80% and 50% at 300^{o}C according to Eurocode 1 [73]). First, the bending load magnitude that causes the structure to reach its elastic limit (F_{EL}) was found. Next, in order to demonstrate shakedown behavior, the bending load was doubled to cause local plastic deformation in the structure when combined with the thermal gradient ($F = 2 \cdot F_{EL}$). An Abaqus/Explicit solver was used to apply 20 cycles of thermal load under constant bending load and the equivalent plastic strain of the rebars was monitored.

Table 2.3: *Material properties of the concrete and rebar.*

Concrete Properties	
Youngs modulus	20 GPa
Poissons ratio	0.18
Yield stress	18.4 MPa
Failure stress	32 MPa
Plastic strain at failure	$1.3{\cdot}10^{-3} mm/mm$
Density	2400 kg/m^3
Cracking failure stress	2 MPa
Rebar Properties	
Youngs modulus	200 GPa
Yield stress	220 MPa

2.3.2 Shakedown results for RC structures

Distributions of axial stresses upon application of the last thermal cycle (#20) are shown for loading levels on the RC slab that result in response just below the elastic limit (Figure 2.23a) and within the shakedown regime (Figure 2.23b). In particular, the thermal load is kept the same in Figures 2.23a and b, and the bending force

is doubled in Figure 2.23b compared to Figure 2.23a to demonstrate shakedown behavior. The results are for a slab cross-section at the rebar layer (see Figure 2.20). In these analyses, the critical rebar location where local plastic strains occur is determined and highlighted in the black box in Figure 2.23b.

The thermomechanical load applied on the structure creates bending stresses along both the length (L) and width (w) directions. Since the right-hand side of the slabs are simply supported, the effect of an increased bending force is mostly seen at the middle of the reinforcement layer (at the x-symmetry lines in Figure 2.23). However, the reinforcing bars can carry only axial stresses that are along the length direction. The nonuniformity of the axial stresses is attributed to the cracking of the concrete under tensile loading.

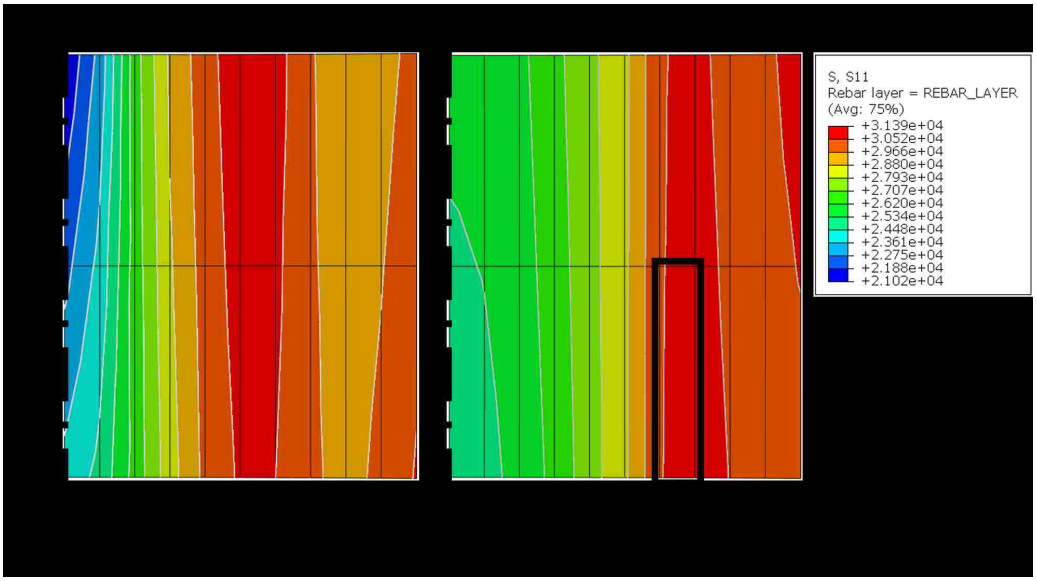

Figure 2.23: *Figure 3: Distribution of axial stresses for the slab at the a) elastic limit ($F = F_{EL}$) and b) shakedown conditions ($F = 2 \cdot F_{EL}$).*

Figure 2.24 shows the axial stress versus axial plastic strain response of the critical rebar location (boxed in Figure 2.23b) during the cycles of thermal. It is observed that some plastic deformation develops at this location in the first loading cycle. Due to the residual stresses in the rebar from unloading, the plastic strains stabilize

in the subsequent loading cycles, leading to shakedown behavior. The shakedown behavior presented in this example could be used in optimizing the design of the RC beam. Namely the rebar type (e.g. diameter) and position could be chosen to promote shakedown performance over a broader range of loading conditions.

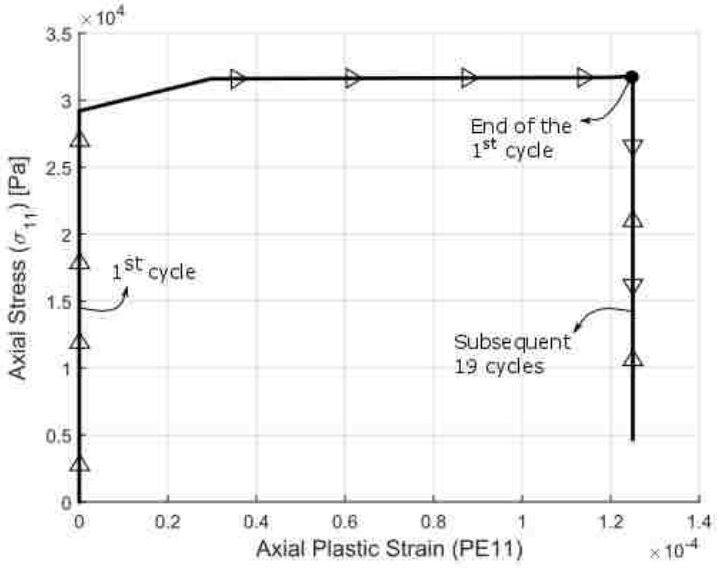

Figure 2.24: *Stress vs plastic strain response of the critical rebar location (highlighted in Figure 2.23) demonstrating shakedown behavior.*

Shakedown analysis for two-way reinforced concrete structures

In order to analyze more modern RC structures that incorporate two-way reinforcements, two additional case studies were performed (Figure 2.25). In the first case, a rebar diameter of 6 mm was used for the rebars in both directions. The bending load magnitude that causes this structure to reach its elastic limit was found. A bending load of a quarter of this magnitude was combined with a cyclic thermal gradient found by a heat transfer analysis that represents the temperature distribution after 0.5 hours in the fire conditions specified by Eurocode 1 [73]. Here the shorter time duration was used so that the maximum temperature of the rebars does not exceed the 300^{o}C threshold chosen in Section 2.3.1.

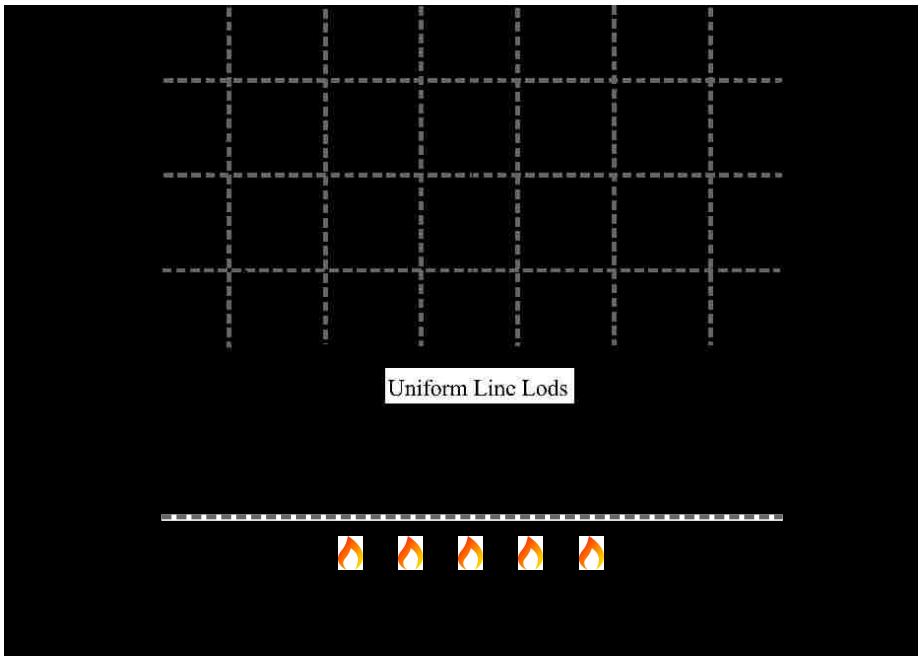

Figure 2.25: *Two-way reinforced concrete slab model.*

Distributions of equivalent plastic strain at the peak of the last thermal cycle are shown for the reinforcement layer in the width direction in Figure 2.26a. Evolution of the equivalent plastic strain at the critical rebar location (red contour region in Figure 2.26a) during thermal cycles is shown in Figure 2.26b. In this first case, the reinforcement bars completely yield and the equivalent plastic strains do not stabilize under the thermomechanical loading considered, causing unsafe structural response (ratchetting).

In the second case study, the same thermomechanical loading is applied on a similar structure with a rebar diameter of 12 mm. In this case, the loading creates only a local plastic deformation in the rebar layer as shown in Figure 2.27a. Evolution of the equivalent plastic strain at the critical rebar location (red region in Figure 2.27a) shows that the plastic deformation stabilizes after the first few cycles: the structure safely shakes down and no accumulation of plastic strain in the subsequent cycles is observed (Figure 2.27b).

In summary, the first test case (that has rebars with a diameter of 6 mm) is

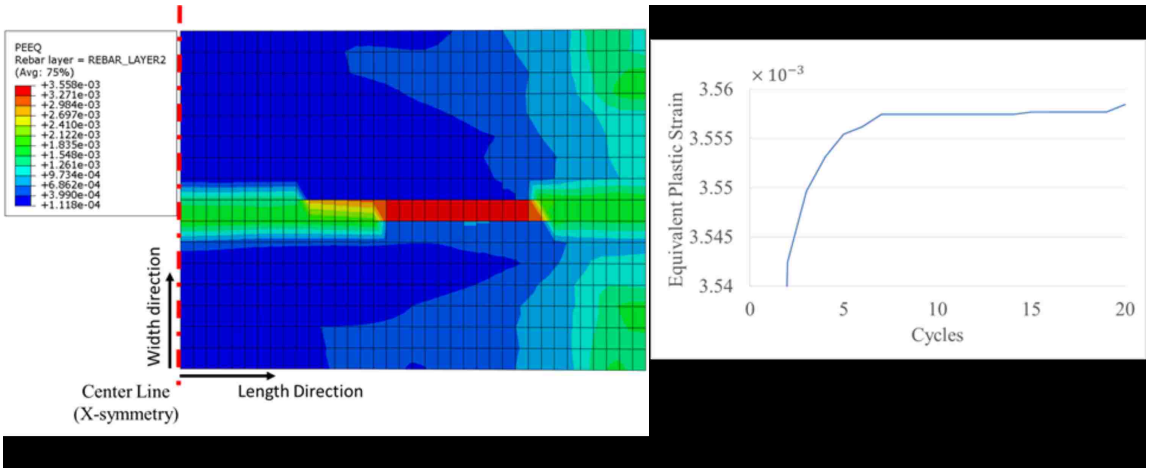

Figure 2.26: *Case 1 with 6mm diameter rebars. a) Distribution of equivalent plastic strain (PEEQ) for the reinforcement layer in the width direction upon application of last thermal cycle and bending load. b) Evolution of equivalent plastic strain at the critical rebar location during 20 thermal cycles.*

inadmissible due to the complete yielding of the reinforcements and non-stabilizing plastic strains. The structure experiences ratchetting which is an unsafe elastoplastic behavior. In the second test case, although the rebars are beyond their elastic limit, shakedown behavior assures no further accumulation of plastic deformation with thermal cycles. The reinforcements can safely carry additional cyclic thermal loading provided that the loading magnitudes are not increased. This simple example illustrates the potential benefits of incorporating shakedown in the design of RC structures to increase allowable loads when compared to elastic limits. This kind of shakedown analysis could be used to more accurately assess structural integrity or improve resiliency. In particular, the two cases presented in this section suggest how designers could include shakedown considerations when sizing rebars. Similarly, rebar distribution and/or graded sizes within the RC slab could be varied to exploit shakedown behavior for resilient designs.

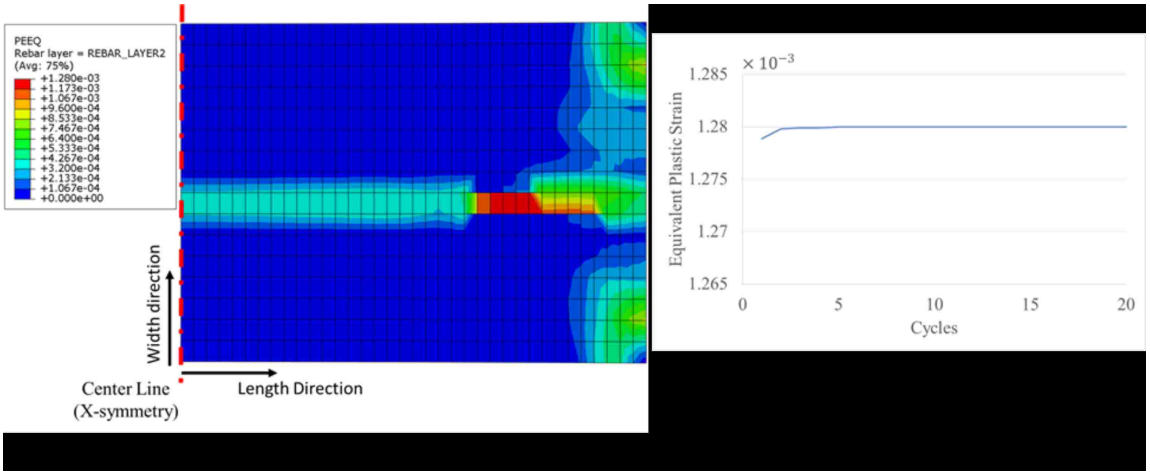

Figure 2.27: *Case 2 with 6mm diameter rebars. a) Distribution of equivalent plastic strain (PEEQ) for the reinforcement layer in the width direction upon application of last thermal cycle and bending load. b) Evolution of equivalent plastic strain at the critical rebar location during 20 thermal cycles.*

Chapter 3

Experimental cyclic inelastic and shakedown investigations

Metallic components often serve under repeated thermomechanical loading conditions in nuclear engineering, aerospace, and automotive industries. Under cyclic thermal and mechanical loadings, materials may inevitably exceed elastic limits. In these cases, for applications not limited by high cycle fatigue, design methodologies that avoid low-cycle fatigue and ratchetting failures are critical. Shakedown-based design approaches can address this need, however they remain generally underutilized (one notable exception is in nuclear engineering codes for pressure vessel design [2, 3]). One reason for this is the lack of experimental shakedown studies of engineering materials and structures available in the open literature. Experimental demonstrations of shakedown behavior and validation of analytical and numerical methods are essential in order to convince designers to adopt shakedown-based approaches. To date there is a shortage of tests involving cyclic, mechanical or thermomechanical loads performed to investigate shakedown limits [24–29].

Pellissier-Tannon *et al.* performed cyclic uniaxial tension-tension and tension compression tests at varying mean stress and stress amplitude values on a stain-

less steel 316 material, and investigated critical stress limits for cyclic plastic strain accommodation (alternating plasticity) at room temperature and 320^oC [74]. The shakedown behavior of a ferritic steel (20 MnMoNi 5 5) was investigated by Heitzer *et al.* under multiaxial (tension-torsion) loading at ambient conditions. Thick-walled hollow samples were subjected to cyclic tensile loads and constant torque. The authors used several mean force and torque values to validate their numerical shakedown limits. A few component-level experimental studies for the shakedown of metallic structures were performed for steel bars and beams [75], steel tubes [76], the partial penetration of welded nozzles in a spherical shell [77], multi-bar components [26], and composite bridges [78, 79].

While direct experimental validation for the numerical case studies of structural shakedown presented in Chapter 2 would be ideal, this is beyond the scope of this dissertation. Instead in this chapter, simpler investigations of material shakedown are presented for metals (SS 316L and IN625) relevant to the applications in Chapter 2. The testing equipment and material details are given in Sections 3.1 and 3.2. The methods and results for uniaxial monotonic, creep, and cyclic inelastic tests on SS 316L and IN625 are given in Sections 3.3 and 3.4, respectively.

3.1 Test Equipment

An MTS 319.25 servo-hydraulic axial-torsional testing frame with an axial load capacity of 250 kN (55 kip) was used for the mechanical testing programs in this chapter. Hydraulic grips with 1 in diameter were used to clamp cylindrical samples. During thermal and mechanical phases of the tests, rotational movement of one of the grips was free so that a zero torsional load was obtained on the samples. The testing frame was equipped with and Ambrell 6 kW induction heating system for the isothermal tests at elevated temperatures. An induction coil was designed to ensure

visibility of the gage section of the samples during the tests for non-contact measurements. The induction heating system provides rapid heating of the samples and a consistent heat production throughout the isothermal tests. The thermomechanical testing equipment used for all of the tests given in this chapter is shown in Figure 3.1.

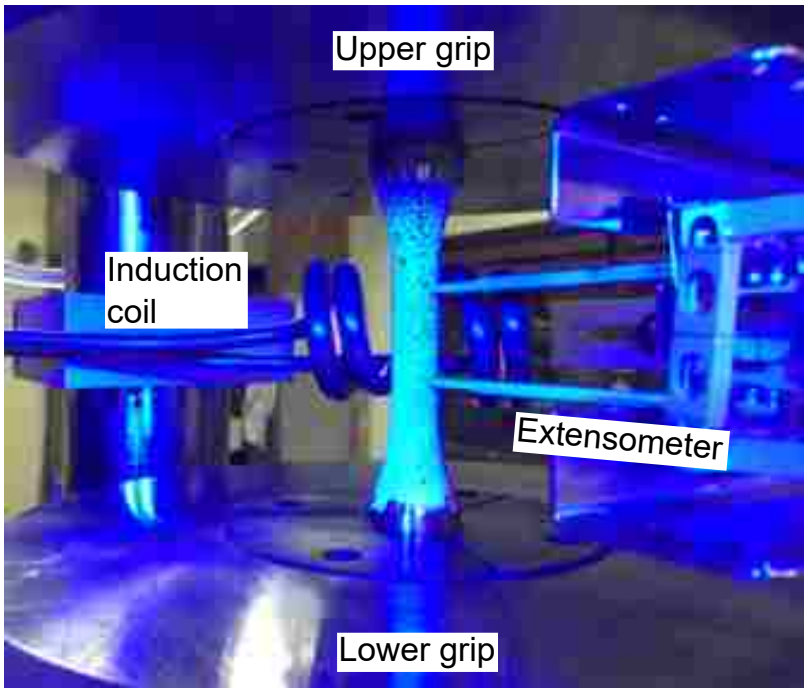

Figure 3.1: *Experimental setup and induction coil.*

Strain measurements were performed using two different methods. A high-temperature, axial-only, MTS 632.53E-11 extensometer with a 1 inch gage length and a high-temperature MTS 632.68E-09 axial/torsional extensometer with a gage length of 2 inches were used to measure axial and axial/torsional strains in the gage length of the samples. Strain signal from this extensometer was also used to control the servo-hydrolic testing frame during monotonic and strain-controlled tests. No cooling of the axial extensometer was required as the extensometer is rated for accurate strain measurements up to 650^{o}C without cooling. Water cooling was used for the axial/torsional extensometer to keep a steady temperature to reduce errors associated

with heating the components of the extensometer. The physical extensometers were accompanied by a stereo digital image correlation system for full-field, non-contact measurements of mechanical fields on the sample surfaces in the gage section. A virtual extensometer that is available in the DIC software was used for comparison with the physical extensometer readings. This was used, for example, to ensure that heat produced during the tests did not affect the accuracy of the extensometer that was in physical contact with the samples. The stereo DIC system was also equipped with a FLIR A655 infrared camera for temperature field measurements. The emissivity value used in the thermography software was calibrated by placing thermocouples on the sample and comparing with non-contact measurements. Full-field measurements of strain and temperature were taken using the DIC and thermal imaging equipment throughout all of the tests explained below (monotonic, creep, force-controlled, and strain-controlled cyclic tests).

Using this equipment, before each thermomechanical test, samples were heated until 600^oC was reached in the gage section, and then they were soaked at this level for 20-30 min. to ensure thermal stabilization. In Figure 3.2, a representative plot of the maximum temperature change with time (Fig. 3.2a) and the temperature distribution for a sample after thermal stabilization (Fig. 3.2b) are shown. It was found from IR measurements that the target of 600^oC was typically achieved within 10 degrees (590^oC) or $< 2\%$ for the middle third of the gage section and 530^oC or $< 12\%$ for the gage extremities.

3.2 Materials

Different materials that are commonly used in pressure vessel and aerospace industries were tested. Annealed 316L stainless steel was used for the uniaxial tests in Section 3.3 because it has broad applications across different industries where shake-

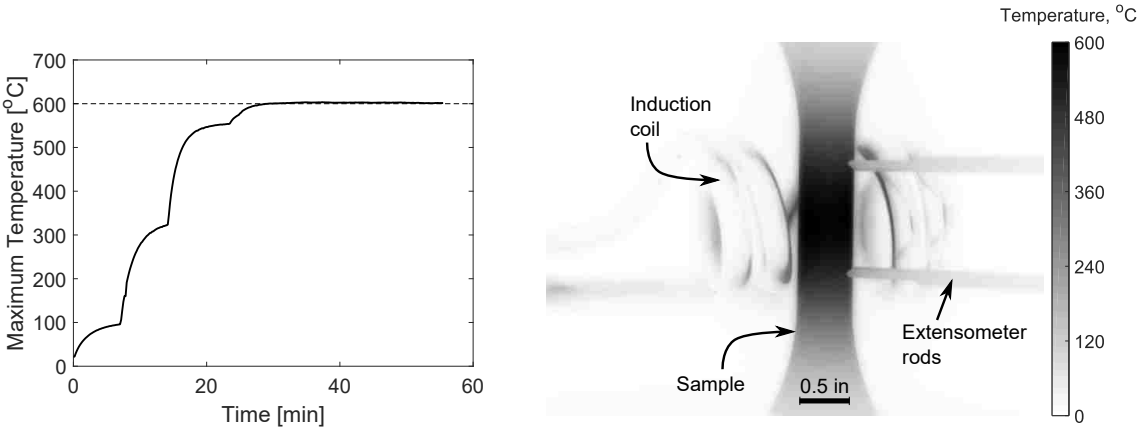

Figure 3.2: *a) Heating of the samples and b) temperature distribution upon thermal stabilization.*

down based designs may significantly enhance performance. For example, SS 316L is used in engine, exhaust and pressure vessel parts in aerospace, automotive, gas turbine and nuclear industries. Also, its mechanical behavior at ambient and elevated temperatures are reported by many authors and available for comparison. IN625 alloy is also used because it is a common nickel-based alloy used in aerospace (and other industries) due to its high strength and resistance to creep and corrosion at elevated temperatures. Its elastoplastic behavior in force-controlled conditions has drawn little attention and is the main focus of Section 3.4.

SS316L and IN625 samples used in the uniaxial tests were machined from 1 in diameter rods to obtain the final dimensions shown in Figure 3.3, following the recommendations in standards ASTM E8, A370, and E466 [80–82].

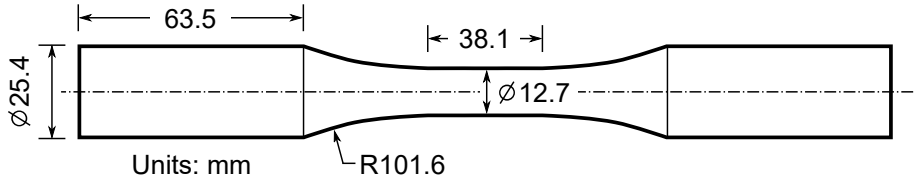

Figure 3.3: *Dimensions of the samples used in the uniaxial tests in this study.*

Table 3.1: *Chemical composition of the materials used in this study.*

SS316L	%C	%P	%Si	%Ni	%Cu	%N	%Ti	%Sn	%Ta	%W
	.024	.028	.65	12.12	.4	.051	.005	.011	.003	.076
	%Mn	%S	%Cr	%Co	%Mo	%Cb	%Al	%B	%V	
	1.79	.024	17.47	.259	2.02	.03	.005	.001	.06	
IN625	%C	%P	%Si	%Ni	%Ti	%Mn	%S	%Cr	%Mo	%Al
	.04	.003	.06	60.79	.22	.05	.001	22.31	8.70	.18
	%Cb	%Fe								
	3.52	3.9								

3.3 Cyclic uniaxial tests on SS316L

Type 316 stainless steel is a corrosion-resistant material that has good mechanical performance at high temperatures (up to 650^oC). While elastoplstic design has been implemented in the codes for pressure vessels made of 316 stainless steel, the codes allow the use of the inelastic analysis *only if* elastic analysis fails to create a feasible design. This severely limits the benefits of shakedown design. Stainless steel 316L is also widely used across gas turbine, and marine industries but the opportunities to realize durability or lightweighting benefits through shakedown have been overlooked. Due to the importance of cyclic uniaxial loadings in design scenarios [83–97], this shakedown study will focus on cyclic tension-tension and tension-compression loading conditions for stainless steel 316L.

Several researchers have investigated the cyclic uniaxial behavior of stainless steel type 316 under ratchetting conditions where the cyclic plastic strain continuously increases and results in failure [74, 92, 98–102]. It is well-known that austenitic stainless steels show rate-dependent creep deformation even at room temperature. It has also been shown experimentally that considerable creep deformation takes place under cyclic uniaxial loads and cyclic creep behavior depends strongly on the temperature for stainless steel type 316 [98, 101, 103, 104] and type 304 [105–110]. Nomine *et al.* performed uniaxial cyclic tension tests prior to and after constant

stress creep tests at room temperature [101]. This provided insight regarding the interaction between creep and the cyclic plastic deformation of stainless steel 316L at ambient temperatures. They reported that when the creep deformation is exhausted before cyclic tension tests (with a maximum stress equal to the creep stress) cyclic strain accommodation (shakedown) takes place rapidly.

Although creep is classically considered a thermally activated mechanism and expected to become more severe with increasing temperature, it has been established that stainless steels show substantial creep up to 200^oC, reduced creep from 250-600^oC, and increasing creep severity with temperature beyond 600^oC. This anomalous behavior between 250-600^oC is associated with the dynamic strain aging (DSA) phenomenon, which is attributed to the presence of solute atoms restricting dislocation movement [111, 112] and reducing creep deformation. Typically, DSA is activated at 250 - 300^oC (depending on the alloy) and at strain rates between $1 \times 10^{-2} - 1 \times 10^{-4}[mm/mm/s]$ and disappears at temperatures above 600 - 700^oC [113–116]. When DSA disappears (above 600 - 700^oC), creep deformation becomes more severe. DSA also contributes to different mechanical behaviors under monotonic and cyclic loading conditions. Under strain-controlled monotonic loading, serrated yielding occurs due to dynamic strain aging. It has also been shown that the low-cycle-fatigue performance (associated with alternating plasticity) is effected by DSA: fatigue life decreases significantly when DSA conditions exist [115, 117–122].

The interaction between creep, DSA and cyclic plastic deformation is complex and requires further investigation in order to evaluate shakedown benefits. In this section, we examine the cyclic behavior of stainless steel type 316L at a maximum temperature of 600^oC, where creep and DSA are interacting (reduced creep observed when DSA is active) and at ambient temperatures where DSA is inactive (and creep dominates). In the presence of these mechanisms, we determine the safe elasto-plastic shakedown limit of the material under cyclic uniaxial loading. We do this

experimentally by constructing Bree-like load interaction diagrams.

This study on SS316L is organized as follows. First, the experimental procedures used in the study are detailed in Section 3.3.1. Mechanical properties are determined through monotonic tests at varying strain rates at ambient and 600^oC and reported in Section 3.3.2. Uniaxial cyclic test results above the elastic limit of stainless steel 316L in force control are also given. Some cyclic tests at ambient conditions are repeated after a creep test in order to show the effect of creep deformation on the cyclic plastic strain accumulation in Section 3.3.2.

3.3.1 Test methods

Monotonic test methods

Monotonic strain-controlled tests at ambient and elevated temperature conditions were performed to investigate the mechanical properties and the rate-dependency of the tested material. This was achieved by incrementally increasing and decreasing the strain rate during monotonic tests by two orders of magnitude similar to the procedure applied in Portier *et al.* and Kang *et al.* [99, 108]. The strain rates used in these tests are: $\dot{\epsilon} = 3 \times 10^{-3}, 3 \times 10^{-4}$, and 3×10^{-5}. Uniaxial strains during the monotonic tests were analyzed using both the axial MTS extensometer and DIC. For the DIC, digital images of the samples were acquired at a constant rate of 2 Hz. With this rate, 10 data points were obtained when the strain rate was largest ($\dot{\epsilon} = 3 \times 10^{-3}$) between the strain ranges of 2-3% and 5-6% (Figure 3.6). A virtual extensometer method available in the DIC software was used to record the uniaxial strain for a 1 inch gage section. For elevated temperature tests, the same procedures were used, however, the samples were also heated prior to initializing the strain-controlled phase. The samples were heated with the induction heater until a maximum temperature of 600^oC measured with a FLIR A655 thermal camera was

obtained. Then the samples were held at the same temperature for 20-30 min. to stabilize the thermal field in the testing area (Section 3.1).

Force-controlled cyclic test methods

The strain response of stainless steel 316L under stress cycles at non-zero mean stress is the main focus in this study and is analyzed using uniaxial force-controlled experiments. These tests are used to find the safe force limit that would result in stable cyclic behavior (shakedown). In this type of test, each sample is loaded to a non-zero mean stress, from which the stress is then cycled by a pre-determined stress amplitude as shown in Figure 3.4. Each sample is tested under three mean stress levels. In these tests all three samples were subjected to $N = 100$ cycles at the smallest mean stress levels and $N = 150$ cycles at the two larger mean stress levels. Using one sample under subsequent increasing stress levels has been shown to have a negligible effect on the measured cyclic behavior for stainless steel 316 [123]. This was demonstrated by first testing a single sample at different cyclic strain levels between 0-4%. Then separate samples were used to test each strain level. The results from both types of tests were compared and shown to have negligible difference.

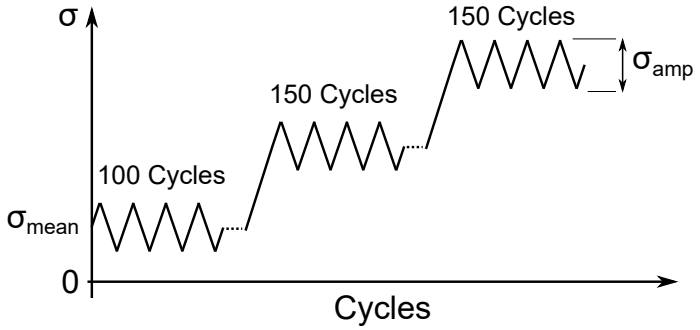

Figure 3.4: *Cyclic uniaxial loading.*

At non-zero mean stress, depending on the loading magnitude and active deformation mechanisms, the material may exhibit a safe cyclic elastoplastic response where the accumulation of plastic strain with cycles arrests (shakedown). When the

loading magnitude is above the shakedown limit, stabilization of the plastic strain is not possible and undesireable cyclic plastic behaviors may result (alternating plasticity or ratchetting). In addition to cyclic plastic straining, the material may also undergo continuous deformation due to creep if active. Although the stress on the sample is cycled, the presence of stress may trigger creep strain and can affect the cyclic behavior [101, 108–110]. In this way, the creep deformation is expected to be larger at high stress levels and when the stress is increasing, and to be diminished at the low stress levels and/or during unloading. As demonstrated by the monotonic tests under various strain rates, the rate-dependent behavior of the material is more pronounced at ambient temperatures; and a very limited rate-sensitivity is observed at 600^oC in this study. Hence, it is expected that the material will experience more creep deformation at ambient conditions and negligible creep at 600^oC (presumably associated with DSA).

Creep-cyclic plasticity interaction test methods at ambient

Tests patterned after Taleb and Cailletaud [124] are used to investigate the contribution of creep deformation on the cyclic accumulation of plastic strain in the force-controlled cyclic experiments. The loading history of this test is illustrated schematically in Figure 3.5. In this test, a sample is first subjected to 3 constant stress levels (corresponding to the maximum stresses at each cyclic level of the tests in Figure 3.4). The duration of the creep tests were set equal to the duration of the stress cycles in the original cyclic test (Figure 3.4). Then the sample was subjected to the original stress cycles at the highest level of the cyclic force-controlled test. In this creep-cyclic test, if the creep deformation is exhausted during the constant stress portion and cyclic stabilization occurs during the force cycles, then one can conclude that creep deformation dominates the cyclic inelastic strain accumulation in the original cyclic tests. Conversely, if the creep deformation is exhausted and

cyclic stabilization does not occur, then the implication is that cyclic plasticity (e.g. ratchetting) is more significant when compared to creep deformation.

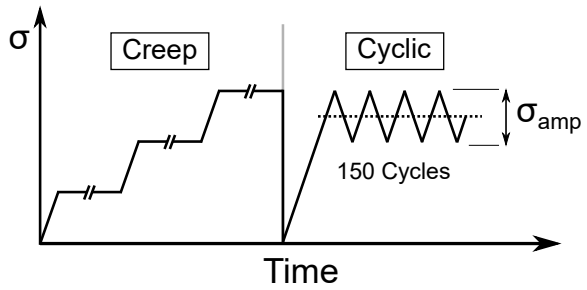

Figure 3.5: *Creep-cyclic uniaxial loading.*

3.3.2 Test results for SS316L

Monotonic test results for mechanical properties

Results of the monotonic tests at ambient and elevated temperatures are shown in Figure 3.6. The true stress - true strain response is given for three rates: $\dot{\epsilon} = 3\times10^{-3}, 3\times10^{-4}$, and 3×10^{-5}. The strain measured by the MTS extensometer is in black and superposed are the measurements from DIC in red. The Young's Modulus (E), linear elastic limit (σ_y^o) and 0.2% yield stress ($\sigma_y^{0.2\%}$) of the material at ambient and the elevated temperature are determined from the monotonic tests and shown in Table 3.2.

Table 3.2: *Mechanical properties of the material at ambient and elevated temperature.*

Temperature	$E\ [GPa]$	$\sigma_y^o\ [MPa]$	$\sigma_y^{0.2\%}\ [MPa]$
Ambient	189	149	331
600^oC	153	79	213

The distinct steps in strain rate levels are clearly visible for the ambient results (confirming strain-rate dependency). In particular, rate-dependency is evidenced at ambient temperature in Figure 3.6 as the material showing a larger stress response at

faster strain rates than the stress response at slower rates. At 600^oC, the strain rate dependency is no longer evident (i.e. there is very little difference between the stress responses for the different strain rates). It is well known that austenitic stainless steel alloys show rate-independence at temperatures between 350-600 ^oC. This decrease in the rate-dependency is associated with the dynamic strain aging phenomenon [108, 113–116, 119, 125–128]. At temperatures above 600^oC, the material recovers rate-dependency as the dynamic strain aging disappears (not shown here). In addition, at 600^oC, serrated flow is seen. This behavior has been reported elsewhere for stainless steel 316 at 600^oC for relatively faster strain rates [113–117, 129, 130]. Serrated flow is caused by the interactions between solute atoms and mobile dislocations in the microstructure and it is commonly used as an indication of DSA [129, 130].

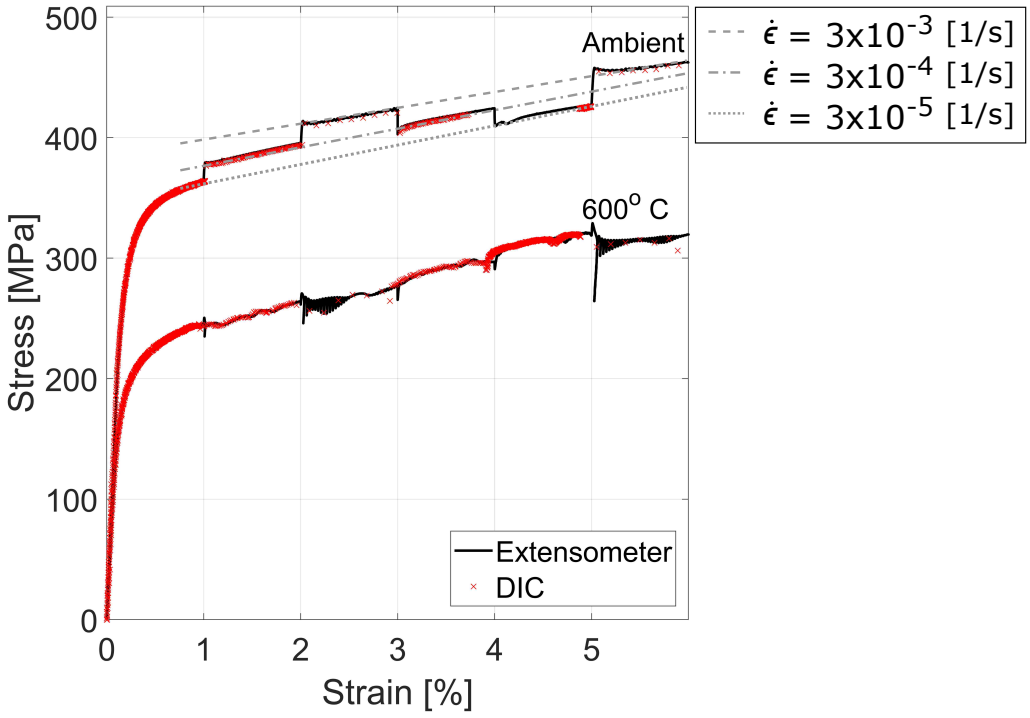

Figure 3.6: *Monotonic test results at ambient and 600^oC.*

Summary of test program at ambient and 600^oC:

By applying various mean stresses and stress amplitudes on the samples (Figure 3.7), we are able to experimentally determine the limit above which plastic strain does not stabilize (the boundary between shakedown and undesirable inelastic behavior). Figure 3.7 is a Bree-like load interaction diagram that shows the tests conducted in terms of normalized mean stress versus stress amplitude at ambient (Fig. 3.7a) and 600^oC (Fig. 3.7b). Tests performed on samples #1, 2 and 3 are shown in open circles, diamonds, and triangles, respectively for ambient and on samples #4 and 5 in open squares and right pointing triangles for 600^oC. Superimposed on these Bree-like load interaction diagrams, are analytical limits for elastic (σ_y^o), 0.2% yield ($\sigma_y^{0.2\%}$), and a cut-off stress corresponding to 5% strain ($\sigma^{5\%}$) using a von Mises criterion. σ_y^o and $\sigma_y^{0.2\%}$ are from Table 3.2 and $\sigma^{5\%}$ is introduced as a maximum cut-off limit that could be used for the design of structures (design considerations are explained later in Section 4.2). All maximum stress levels applied on the samples are above the material's linear elastic limit (σ_y^o, dashed black line) determined from the monotonic tests.

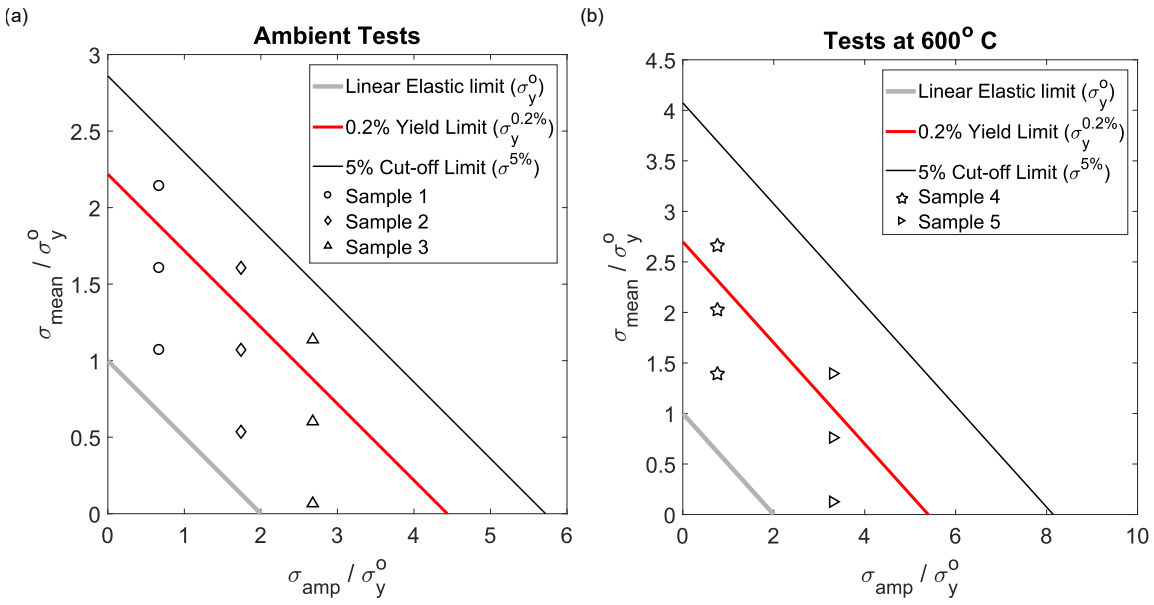

Figure 3.7: *Experimental program for the force-controlled cyclic tests on SS 316L.*

Ambient force-controlled test results:

Results of the force-controlled tests are shown in Figure 3.8 for three samples at ambient temperature. True stress versus strain response of the samples under cyclic loading are given in Figures 3.8a, c and e. The maximum strain at cyclic stress peaks is shown in Figures 3.8b, d and f and the strain increment per cycle ($\frac{\Delta\epsilon}{\Delta N}$) at the end of cycling at each level is shown for the samples. The stress-strain plot in Figure 3.8a shows the hardening of the material during loading between the mean stress levels and the strain accumulation during force cycling at the highest load level. Evolution of the maximum strain per cycle is extracted from the stress-strain data and plotted in Figure 3.8b.

It is shown in Figures 3.8b, d and f that plastic strain accumulation stabilizes (suggesting shakedown, $\frac{\Delta\epsilon}{\Delta N} \cong 0$) at the first two stress levels. However for the largest stress level, although the cyclic strain rate significantly decreases, no stabilization occurs (suggesting ratchetting). However, in the stress-strain diagrams in Figures 3.8a, c and e near the stress peaks of the last stress level, rounded peaks are observed. These rounded peaks indicate that creep deformation is taking place [131]. In particular, strain continues to increase even after the stress reaches the maximum point and starts to decrease.

The implication is that the cyclic strain accumulation observed at the largest stress level in the samples 1, 2, and 3 is dominated by creep deformation and not cyclic plastic deformation (ratchetting). This is supported by several factors. First, in order for ratchetting deformation to occur, a stress amplitude larger than 2 times the initial size of the yield limit of the material should be applied at non-zero mean stress [123]. This criterion is schematically illustrated in Figure 3.9 assuming only kinematic hardening. When the stress amplitude is smaller than 2 times the initial yield surface size (σ_y^o), after hardening during the loading portion of the first cycle, the

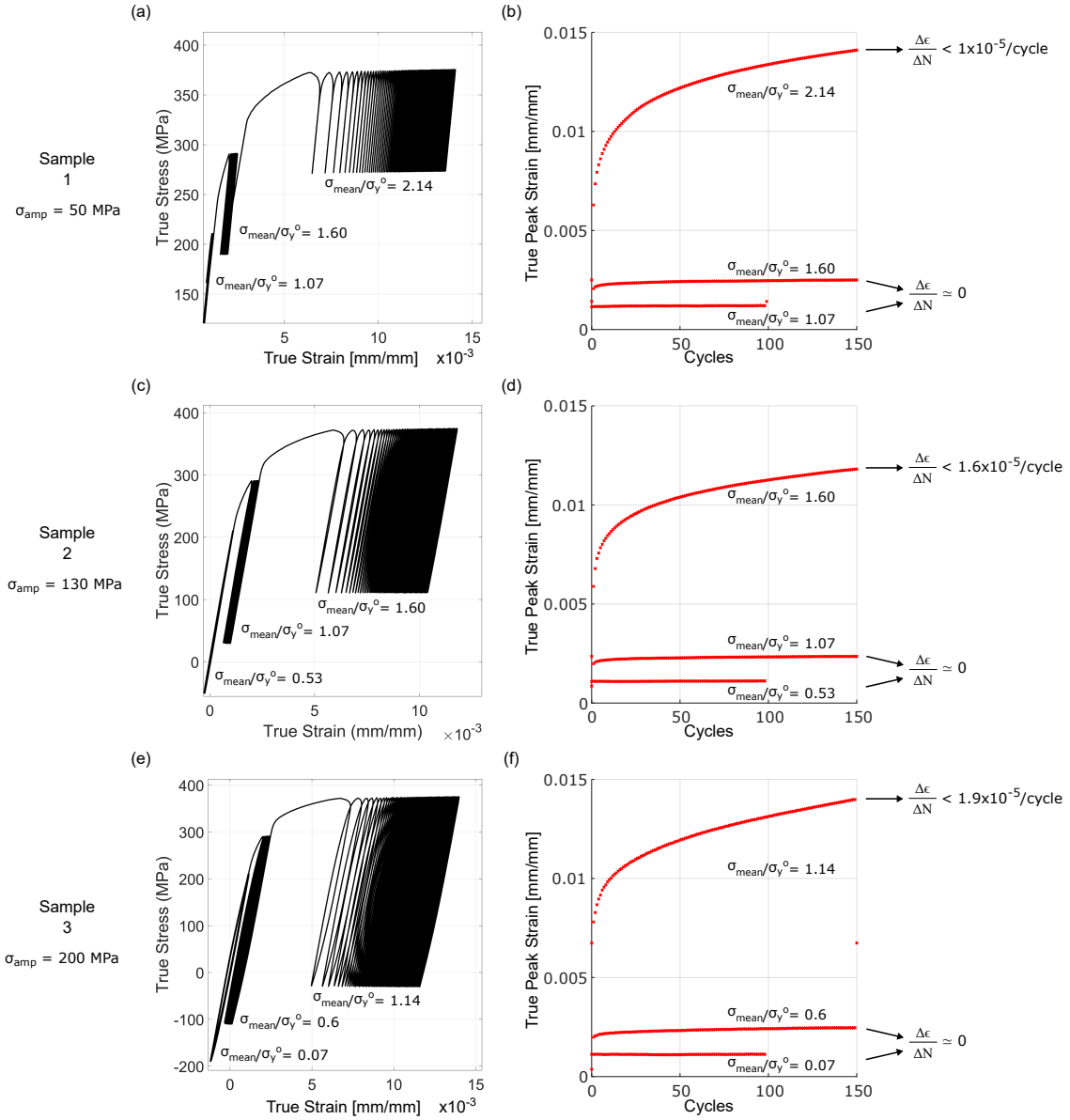

Figure 3.8: *Hysteresis loops and peak strain evolution per cycle demonstrating the stable (shakedown) and unstable behavior of the samples.*

yield surface remains unchanged. This is because, upon the removal and reloading of the axial load, the stress state will stay within the new yield surface and will not cause any further plastic deformation (Figure 3.9a). When the stress amplitude is larger than 2 times the initial yield surface size, the cyclic loading would cause an evolution of the yield surface both at the minimum and maximum stress levels (Figure 3.9b).

When combined with the isotropic hardening and limiting surface for the backstress, the latter would cause accumulation of the plastic strain (ratchetting). The reader is referred to Lemaitre and Chaboche, Section 5.4.4 for further information on this behavior [123].

Secondly, it is shown by Nomine *et al.* by similar experiments on stainless steel 316L at room temperature, that strain accumulation under cyclic axial tension loads is due to creep deformation [101]. This is demonstrated Nomine *et al.* by performing constant stress creep tests prior to cyclic tension tests (with a maximum stress equal to the creep stress). As a result, once the creep deformation is exhausted before tensile cycling, cyclic strain increments are accommodated rapidly (shaking down), and showing no ratchetting deformation. Thirdly, as it will be shown later for elevated temperature tests, when creep is reduced in the DSA regime, no ratchetting deformation is observed at similar normalized load amplitudes. The effect of creep deformation on the room temperature cyclic shakedown tests will be further investigated in this study, through a creep-cyclic test in Section 3.3.2.

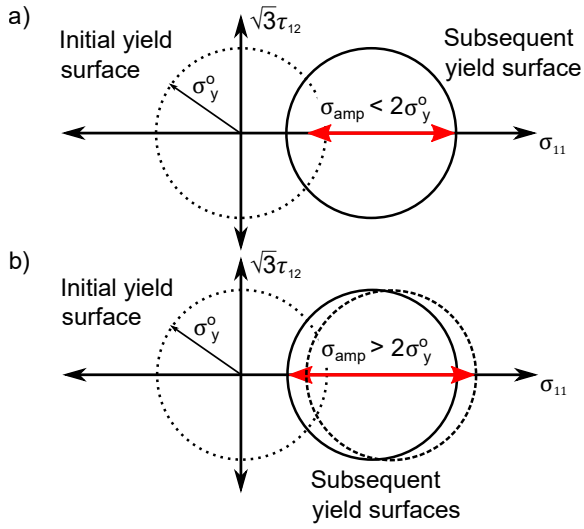

Figure 3.9: *Illustration of ratchetting condition under uniaxial loading.*

The second and third samples are tested at ambient at larger stress amplitudes than the first sample (Figure 3.8c-f). The amplitudes used for these samples were

large enough to cause compressive stresses when the applied force is a minimum. A hysteresis loop becomes visible at the largest loading level of the third sample (Figure 3.8e). This indicates that creep deformation is combined with time-independent cyclic plastic deformation (alternating plasticity or ratchetting). If the amplitude were increased further, cyclic plastic behaviors (alternating plasticity or ratchetting) would become more critical in the uniaxial cyclic tests. The importance of combined ratchetting-creep deformation in the uniaxial cyclic behavior of stainless steel 304 has been reported by Yoshida [105] and, Taleb and Cailletaud [124] but is not the focus of this study.

Expansion of feasible design space (by 2 times) for SS316 at room temperature is demonstrated using the Bree load-interaction diagram in Figure 3.10 based on the experimental program given in Figure 3.7 (markers indicate the experimental points used at ambient). Stress amplitudes above the largest experimental value ($\sigma_{amp}/\sigma_y^o = 2.7$) are not considered and are grayed out in Figure 3.10. This is done because undesirable time-independent cyclic plastic behaviors (ratchetting, alternating plasticity) are expected.

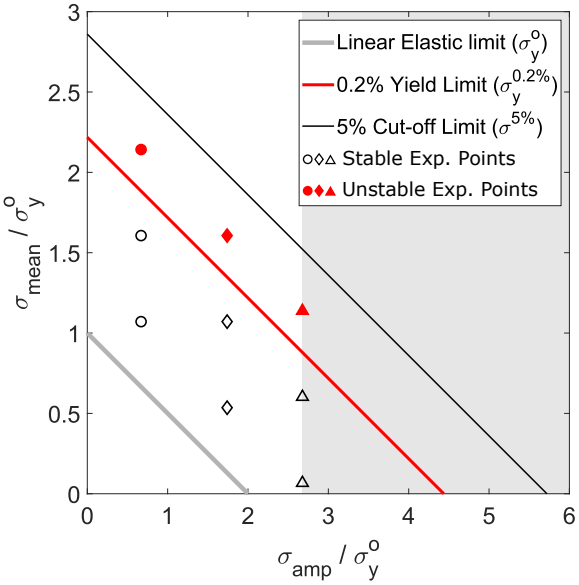

Figure 3.10: *Bree load interaction diagram showing the shakedown (SD) limit of the material at ambient conditions.*

Force-controlled test results at 600^oC

A similar procedure was applied on two more samples at a constant elevated temperature of 600^oC where a small stress amplitude and a large stress amplitude case was investigated (Figure 3.11). The true stress-strain response of the material is given in Figure 3.11a and c and corresponding maximum strains at stress peaks are given in Figure 3.11b and d. In all of the loading cases, stabilization of the cyclic plastic strain was observed ($\frac{\Delta\epsilon}{\Delta N} \cong 0$, indicating shakedown). As shown in the monotonic test results in Figure 3.6, rate dependency of the material is suppressed, suggesting negligible creep deformation. This is supported by the stress-strain cycles in Figure 3.11a as no rounded peaks or strain accumulation is seen in the material response. In all loading cases, an elastic cyclic behavior is recovered after substantial plastic deformation. This indicates that the shakedown performance of the material is enhanced at the elevated temperature considered in this study. This provides motivation for expanding the safe-use limits of structures made of stainless steel 316L using shakedown-based design methods.

Expansion of feasible design space for SS316 at 600^oC is demonstrated using the Bree load-interaction diagram in Figure 3.12 based on the experimental program given in Figure 3.7 (markers indicate the experimental points used at 600^oC). Stress amplitudes above the largest experimental value ($\sigma_{amp}/\sigma_y^o = 3.3$) are not considered and are grayed out in Figure 3.12. This was done because undesirable alternating plasticity is expected which limits the shakedown domain. The shakedown limit (blue squares) is estimated to be coincident with the 5% strain cut-off limit (Figure 3.12). This is done because no incremental accumulation of plastic strain (ratchetting or creep) was observed in the tests performed at this temperature. Because there is effectively no creep deformation, the material is expected to show a stabilized cyclic response at all stress levels below the collapse limit (not shown).

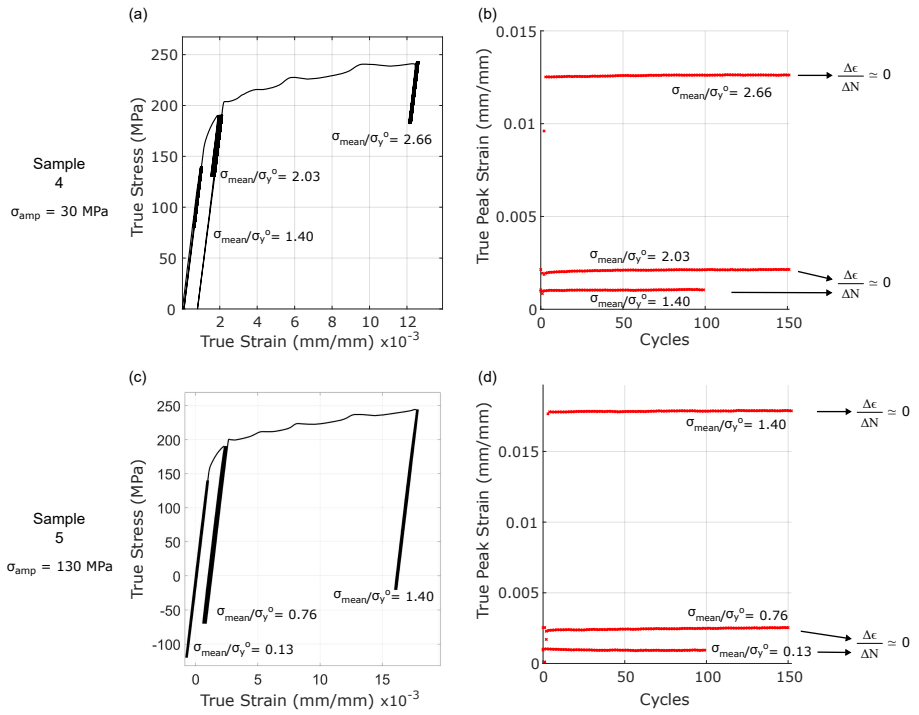

Figure 3.11: *Hysteresis loops & peak strain evolution per cycle demonstrating the stabilization of the cyclic plastic strain at elevated temperature.*

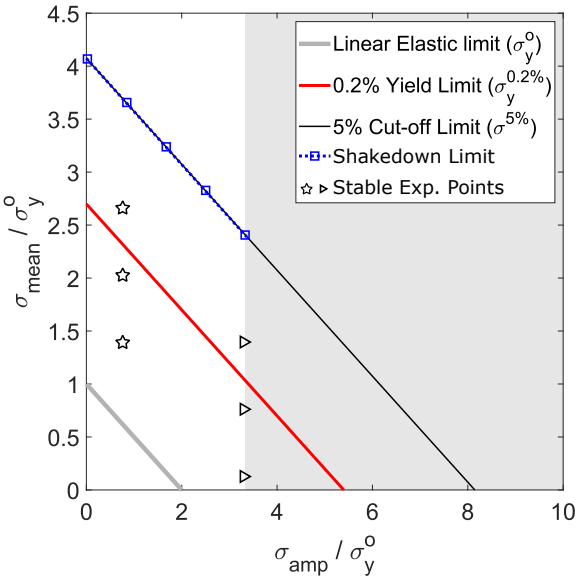

Figure 3.12: *Bree load interaction diagram showing the shakedown (SD) limit of the material at 600ºC.*

At 600^oC, the shakedown limit is estimated to be coincident with the 5% strain cut-off limit as shakedown is expected at all loading levels below the collapse limit. This suggests further expansion of the potential feasible design space based on shakedown: 4 times when compared to the linear elastic limit.

Creep-cyclic test results at room temperature:

In this section the results of creep-cyclic tests at room-temperature (Section 3.3.1) are used to identify the contribution of creep deformation in the ambient force-controlled cyclic experiments. The small-amplitude force-controlled cyclic test at ambient conditions (Figure 3.7a, Sample 1) is repeated after a sample was subjected to constant stress at the maximum stress levels of the cyclic test (i.e. 210, 290, 375 MPa). The creep time was set to the duration of the stress cycles in the original cyclic test (i.e. 45 minutes at the smallest stress level and 66 minutes at the other two stress levels.). After the creep test at the largest stress level, the sample was subjected to the original stress cycles (from Figure 3.8a).

Figure 3.13 shows the results of the creep-cyclic tests at ambient. Creep deformation at the three maximum stress levels of the cyclic test is shown in Figure 3.13a. This is shown as axial strain as a function of time recorded by DIC (crosses) and extensometer (black line) with good agreement. It is observed that while the creep deformation stabilizes at the first two stress levels, unstable creep deformation occurs at the largest stress level within the duration of the creep test. The material's stress-strain response to the stress cycles after the creep test and peak strain at stress peaks are also shown in Figures 3.13b and c. When compared to the cyclic force-controlled test shown in Figure 3.8a,b (performed at the same mean stress and stress amplitude), plastic strain in the creep-cyclic test stabilizes with cycles. This stabilization occurs because the creep deformation is mostly exhausted in the initial creep phase of the test.

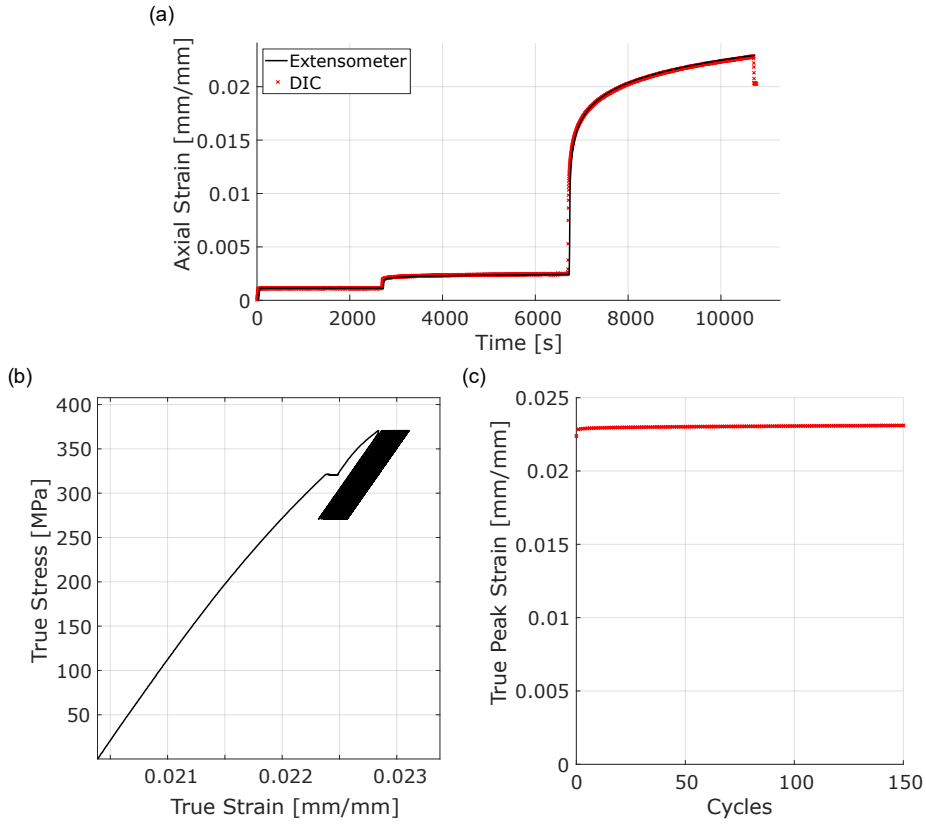

Figure 3.13: *Creep-cyclic test results. a) Creep strain evolution at three stress levels, b) true stress-strain response to the load cycles after the creep phase, and c) Maximum strain at stress peaks during load cycles after the creep phase.*

The results suggest that the cyclic strain accumulation in all three samples at ambient conditions is dominated by creep deformation. For this reason, the results of the creep test will be used to determine the parameters of a numerical creep model (Chapter 4). This model will then be used to investigate the cyclic creep behavior of the material at different mean stress and stress amplitudes in Section 4.1 to aide in determining the shakedown limit (stable cyclic inelastic behavior) of the material.

3.4 Cyclic uniaxial tests on IN625

The nickel-based superalloy Inconel 625 (IN625) has been primarily used in aerospace, pressure vessel, marine, and gas turbine applications. The material is preferred in

these applications for its high strength, corrosion resistance and creep resistance at elevated temperatures up to about 1140 ^oC (2100 ^oF) [132–137]. Often the service conditions for this material involve complex cyclic thermomechanical loadings, and in some cases, such as hypersonic flight, could involve relatively few cycles. Conventionally, first-yield based methods are used for the design of aerospace structures to avoid plastic behaviors that lead to failure. However, design methods based on purely linear elastic behavior may also fail to find feasible or lightweight solutions. Thus, inelastic analysis (for shakedown) may be required to accurately assess the load-bearing capacity of thermostructural components in extreme environments.

Inelastic shakedown-based design methods require load-contolled tests to determine safe loading limits to achieve shakedown behavior. In contrast, the cyclic inelastic behavior of IN625 has mostly been investigated through strain-controlled tests for low-cycle-fatigue (LCF) life [138–140]. In this way, there is a lack of studies investigating the material's behavior under force-controlled conditions in the literature. As one notable exception, the cyclic inelastic behavior of IN625 was investigated under both strain-controlled and force-controlled conditions by Suave et al. [139]. In particular, the authors study the effect of age hardening on the mechanical properties, low cycle fatigue, and ratchetting response as well as microstructural changes during the cyclic loading at elevated temperatures. They concluded that age hardening improves the LCF performance, due to strengthening by the γ'' precipitate formation. They also observed that age hardening results in lower ratchetting rates.

Additionally, as demonstrated in Section 3.3 for stainless steel, understanding interactions between cyclic plastic behaviors and rate-dependent behaviors such as dynamic strain aging (DSA) is of great importance to develop more robust design strategies. The effect of DSA on the behavior of IN625 in load-controlled tests is also unknown due to lack of published experiments of this type in the inelastic regime. Based on strain/deformation based data, IN625 shows DSA behavior at a wide range

of temperatures (250 - 750^oC) and strain rates (10^{-5} - 10^{-3} $1/s$) [141–144]. DSA is a strengthening mechanism caused by solute atoms that restrict dislocation movement in the microstructure. DSA results in rapid fluctuations (serrated yielding) in the macroscopic stress-strain behavior. It has been observed through a set of tensile tests that the critical strain for the onset of DSA for IN625 decreases with temperature and increases with strain rate in the temperature range of 250-450^oC. Above 450^oC, the effects of temperature and strain rate on the critical DSA strain are not as clear [141, 142]. In addition to standard tensile tests, Maj *et al.* performed high-speed compression tests on IN625 at strain rates of 0.1, 1, and 10 s^{-1} at 600^oC [145]. They observed serrated yielding effects (an indicator for DSA) even at the largest strain rate in compression. To the best of the authors' knowledge, this dissertation is the first to present the effect of the DSA on the inelastic stress-strain behavior in force-controlled tests in the literature.

In the following, the intent is to motivate inelastic design strategies, (that could be used for example, to support hypersonic flight) by demonstrating macroscopic shakedown behavior for IN625 at 600^oC in the presence of rate-dependent behaviors (DSA). Testing methods used in this study are described in Section 3.4.1. Experimental results and discussions are presented in Section 3.4.2.

3.4.1 Test methods

Monotonic strain-controlled tests for rate-dependent DSA behavior

Three monotonic tests were performed at 600^oC in strain control using the MTS extensometer and FlexTest 40 controller. Three samples were tested at various strain rates ($\dot{\epsilon} = 3{\cdot}10^{-5}$, $3{\cdot}10^{-4}$ and $3{\cdot}10^{-3}s^{-1}$) in order to investigate the rate dependency of the mechanical properties and DSA behavior. During the monotonic test on one of the samples, the strain rate was incrementally increased and decreased to check the

strain rate history effect (Figure 3.17 shows results). All three samples were loaded up to a 5% maximum strain, approaching collapse, but limited in order to protect the MTS extensometer.

Mechanical properties of the material such as the linear elastic limit (σ_y^o), 0.2% yield limit ($\sigma_y^{0.2\%}$), 2% cut-off limit ($\sigma_{cut-off}^{2\%}$), and 3% cut-off limit ($\sigma_{cut-off}^{3\%}$) were determined as the average of three monotonic uniaxial tests in strain-control at 600^oC, and their values are given in Table 3.3. Yield limit is found to be the same in tension and compression. The tests were performed up to a 5% strain, and approaching collapse, at various strain rates from $3 \cdot 10^{-5}$ - $3 \cdot 10^{-3}$ s^{-1}. The maximum of 5% strain was also chosen in order to protect the extensometer used for strain measurements. In the design of some engineering structures, maximum accumulated inelastic strain is restricted by design standards. The cut-off limits are superimposed on Figure 3.6 to represent the allowable stress for a maximum cut-off strain level that could be used for the design of structures.

Table 3.3: *Mechanical properties of the material at 600ºC* .

σ_y^o	$\sigma_y^{0.2\%}$	$\sigma_{cut-off}^{2\%}$	$\sigma_{cut-off}^{3\%}$
362 ± 17 MPa	473 ± 6 MPa	516 ± 4 MPa	550 ± 7 MPa

Strain-controlled cyclic test methods

Symmetric cyclic tests were performed in strain control using the MTS extensometer and FlexTest 40 controller (Section 3.1). Increasing levels of symmetric strains, $\pm 0.3\%$, $\pm 0.4\%$, $\pm 0.6\%$, $\pm 0.8\%$ and $\pm 1\%$ were applied at 600^oC to investigate the cyclic hardening behavior of the material with a strain rate of $\dot{\epsilon} = 6 \cdot 10^{-3}$ 1/s. This rate corresponds to the post-yielding rate targeted in the force-controlled cyclic tests (Section 3.3.1). One hundred cycles were applied at each strain range, and the test was repeated twice. A schematic of the loading for these tests is shown in Figure

3.14. In order to check the effect of strain cycles at smaller levels on the behavior in the largest strain range, two more samples were tested only at ±1% with the same strain rate ($\dot{\epsilon} = 6 \cdot 10^{-3}$). In these two additional tests, 100 cycles were also applied.

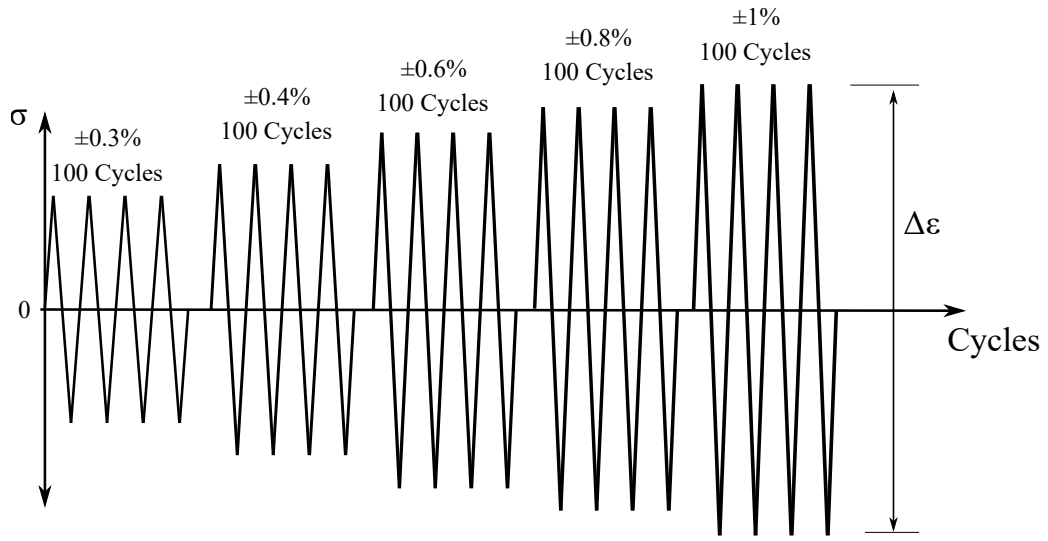

Figure 3.14: *Loading conditions used in the strain-controlled tests.*

Force-controlled cyclic test methods

Force-controlled cyclic tests were performed in order to establish whether or not shakedown states were achieved for a variety of cyclic tension-compression loading levels with non-zero mean stresses, listed in Table 3.4. In these tests, samples were first loaded to a non-zero mean stress (Figure 3.15a). Then, the stress was cycled with a predetermined amplitude; the loading rate was fixed at 15 MPa/s. The mean stress ans stress amplitude levels (Table 3.4) were set such that the stress state in each sample would exceed the 0.2% yield stress ($\sigma_y^{0.2\%}$) of the material during both loading and unloading for each cycle. This behavior is expected to cause ratchetting or alternating plasticity at large amplitudes and is illustrated in Figure 3.16. Note that each sample was tested at three stress amplitudes (for example, 1a, 1b, 1c, Table 3.4) while the mean stress on the sample was kept constant, as shown in Figure 3.15a. The purpose of testing one sample at multiple levels was to reduce the cost and time

for testing. It will be shown later in Section 3.4.2, that performing these tests with consecutively increasing load levels on a single sample is negligably different from individual tests on separate samples (following example cyclic plasticity testing procedures presented in Chaboche and Lemaitre [123]).

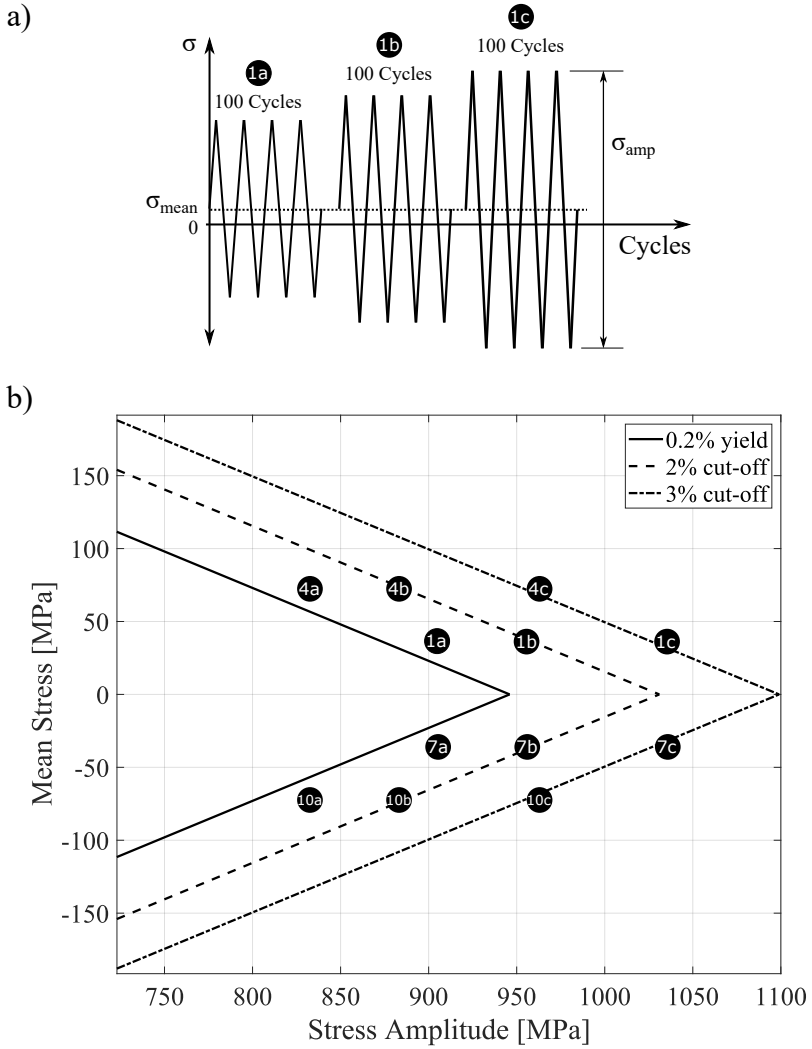

Figure 3.15: *a) Tension compression cycles applied in force-controlled cyclic experiments, b) load-interaction diagram showing the loading sets used in the force-controlled cyclic tests Table 3.4.*

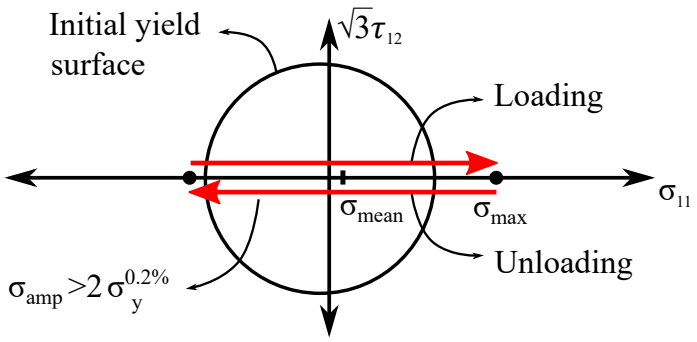

Figure 3.16: *An example of stress conditions in the force-controlled cyclic tests.*

This procedure was used to investigate various mean stresses ranging from tension to compression. In order to facilitate comparison, when the mean stress was changed from tensile to compressive, the stress amplitude was set such that the maximum absolute stress on the samples stayed the same (Table 3.4). Repeatability was established by testing additional samples under the same loading conditions (samples #2, #5, #6, #8, and #11 are marked by "(r)" for repetition in Table 3.4). During all tests, 100 cycles were applied for each loading case (a, b or c). Also, one sample was tested directly at the largest stress amplitude for some of the mean stress cases (samples #3, #9, and #12 are denoted "single-level" in Table 3.4) to check if there was any effect of the prior cycles at smaller stress amplitudes on the behavior during the subsequent load levels (history effect).

In order to better visualize the testing program from Table 3.4, it is also presented in a load-interaction diagram in Figure 3.15b. 0.2% yield ($\sigma_y^{0.2\%}$), 2% strain and 3% strain cut-off limits ($\sigma_{cut-off}^{2\%}$, $\sigma_{cut-off}^{3\%}$) are superimposed on the load-interaction diagram with the values given in Table 3.3. The limits of the load-interaction diagram are set such that all of the loading combinations shown cause yielding in both tension and compression. In particular, minimum and maximum limits of the stress amplitude along the x-axis are set to $2 \cdot \sigma_y^0 = 740\ MPa$ and $2 \cdot \sigma_{cut-off}^{3\%} = 1100\ MPa$ to ensure plastic deformation at the minimum and maximum stress reached

Table 3.4: *Cyclic tests performed in force control. All stress values are in MPa.*

Sample	Description (r: repetition)	Mean Stress [MPa]	Stress Amplitude			Maximum Stress		
			a	b	c	a	b	c
1	Multilevel	36	905	956	1035	489	514	554
2	Multilevel (r)	36	905	956	1035	489	514	554
3	Single-level	36	1035			554		
4	Multilevel	72	833	883	963	489	514	554
5	Multilevel (r)	72	833	883	963	489	514	554
6	Multilevel (r)	72	833	883	963	489	514	554
7	Multilevel	-36	905	956	1035	-489	-514	-554
8	Multilevel (r)	-36	905	956	1035	-489	-514	-554
9	Single-level	-36	-1035			-554		
10	Multilevel	-72	833	883	963	-489	-514	-554
11	Multilevel (r)	-72	833	883	963	-489	-514	-554
12	Single-level	-72	963			-553.9		

during a cycle without exceeding the 3% strain cut-off limit of the material. Mean stress limits along the y-axis are bounded by the condition that the maximum stress should not exceed the 3% strain cut-off limit. The data points in Figure 3.15b indicate the loading sets used in the testing program, Table 3.4. While the cyclic force-controlled tests can be used to establish shakedown, ratchetting or alternating plasticity responses, strain-controlled tests are also required in order to investigate the influence of the DSA behavior (which has been shown to be rate-dependent for IN625 [141, 142]) on the cyclic inelastic responses observed.

3.4.2 Uniaxial test results for IN625

Monotonic test results for mechanical properties

Strain-controlled monotonic test results from the three samples at different rates are shown in Figure 3.17. Axial stress-strain plots in this figure correspond to a sample tested at strain rates of $\dot{\epsilon} = 3 \cdot 10^{-5}$, $3 \cdot 10^{-4}$, and $3 \cdot 10^{-3}$ (black dots), a sample tested at a constant rate of $\dot{\epsilon} = 3 \cdot 10^{-5}$ (red dots) and one at $\dot{\epsilon} = 3 \cdot 10^{-4}$ (blue

dots) respectively. The linear elastic limit (σ_y^o), 0.2% yield limit ($\sigma_y^{0.2\%}$), 2% cut-off limit ($\sigma_{cut-off}^{2\%}$), and 3% cut-off limit ($\sigma_{cut-off}^{3\%}$) given in Table 3.3 are superimposed on the stress-strain curves in Figure 3.17 as horizontal dashed lines. These limits are useful to compare with the strain levels obtained in the force-controlled tests in Section 3.4.2.

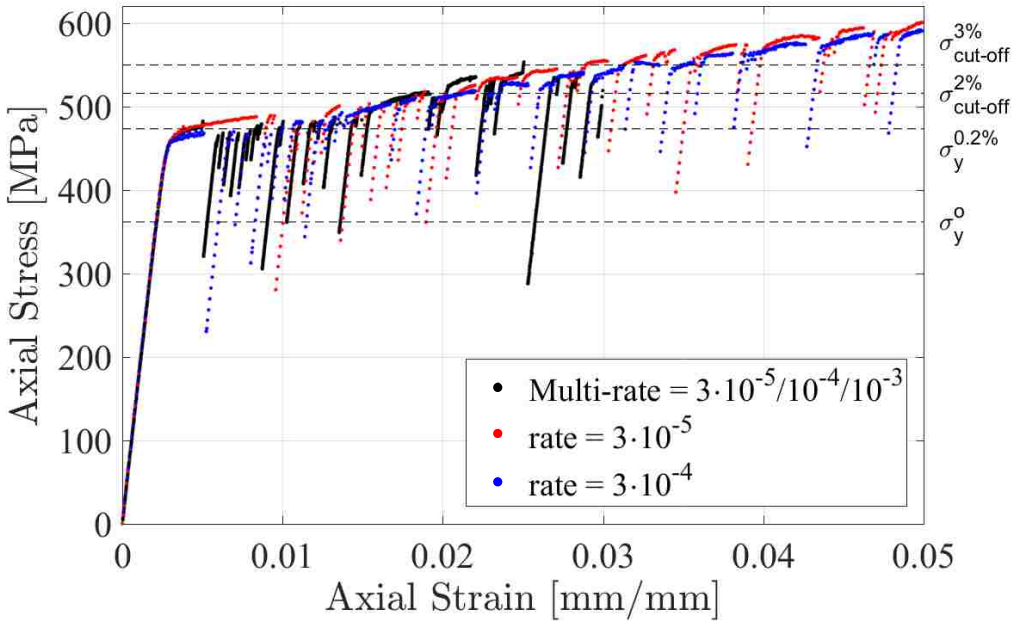

Figure 3.17: *Monotonic test results at 600°C .*

These monotonic tests at different strain rates show that the rate-dependency of the mechanical properties is negligible. Dynamic strain aging behavior (serrated yielding) was observed at all of the strain rates used in these tests. The amplitude of the serrations in the monotonic tests vary widely; however, the critical strain at the onset of serrations decreased with the strain rate. For example, the DSA started at larger strain levels when the strain rate was the smallest ($\dot{\epsilon} = 3 \cdot 10^{-5}$). The implication is that DSA may be in effect at a wide range of rates (e.g. $10^{-5} - 10^{-3}$) and may start at very small strains in the force-controlled tests if the rate is larger than the fastest rate used in the monotonic tests ($\dot{\epsilon}_{max} = 3 \cdot 10^{-3}$).

Strain-controlled cyclic test results

Representative results of the cyclic strain-controlled tests under increasing levels of strain ranges (±0.3%, ±0.4%, ±0.6%, ±0.8% and ±1%) are shown in Figure 3.18. The stabilized cycle stress-strain loops (at cycle #100 for levels 0.3-0.8%, and before failure for strain level of 1%) of each strain range (Figure 3.18a) and the evolution of the stress peaks throughout the entire test (Figure 3.18b) are given. It is observed that the material cyclically hardens when the strain range is above ±0.6%. The maximum stress reaches 800 MPa (in compression), and the sample failed after 60 cycles in the last level of the test when the strain range was ±1%.

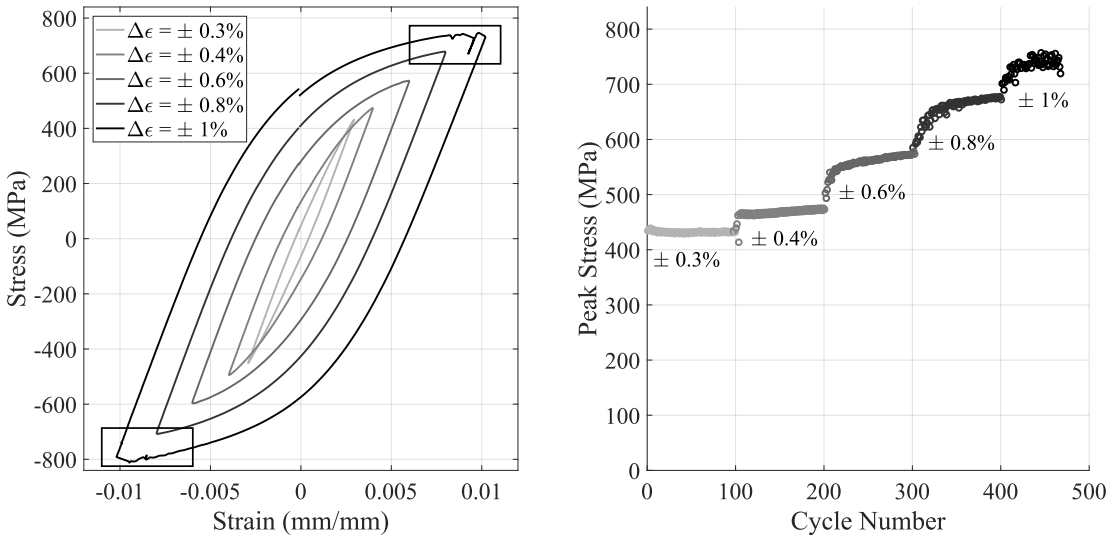

Figure 3.18: *Representative strain-controlled test results of a sample tested under consecutive increasing strain ranges at 600ºC .*

DSA was observed during the strain-controlled cyclic tests both in tension and compression at strain ranges of ±0.6%, ±0.8% and ±1% in the initial cycles and disappeared during the cycling at ±0.6% and ±0.8%. However, at the ±1% strain level, the DSA effect persisted during all cycles until failure. Thus behavior is especially evident through serrations in the boxed regions in Figure 3.18a.

In order to check the effect of the previous cycling at smaller strain ranges on the

cyclic behavior for the last strain level (i.e. effect of the first 400 cycles in Figure 3.18b on the behavior during the final ±1% cycles), two additional samples were tested for 100 cycles only at the ±1% strain level. The evolution of the stress-strain loops at intermediate cycles and peak stresses plotted against cycle number for all 100 cycles are shown in Figures 3.19a and 3.19b, respectively. The results show that the sample cyclically hardened for approximately 50 cycles and then stabilized for the remainder of the test. DSA behavior is also observed in the tensile and compressive yielding portions of the hysteresis loops in Figure 3.19a.

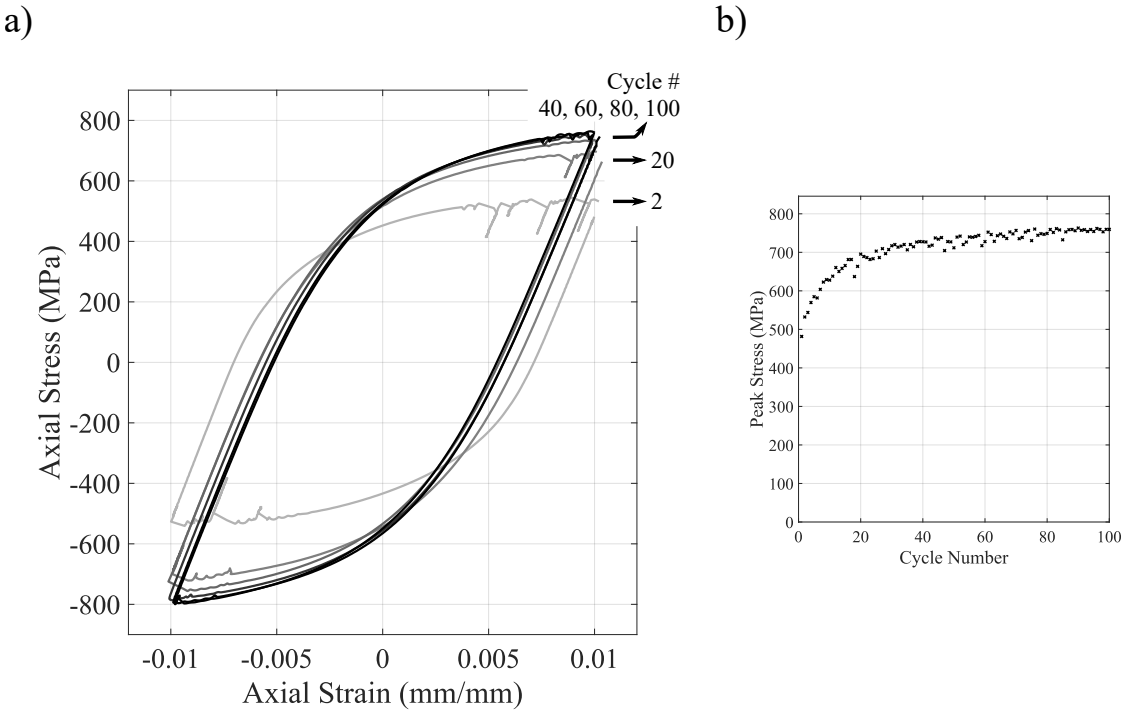

Figure 3.19: *Strain-controlled test results of a sample tested at ±1% at 600°C .*

Comparison of the representative behavior of the two tests without prior loading history shown in Figure 3.19 with the sample tested at multiple strain levels (Figure 3.18) is shown in Figure 3.20. Figure 3.20a shows the stabilized cycle hysteresis loops of the multi-level test and final cycles (stabilized or before failure) of the two samples tested only at ±1% strain. The hysteresis loops of all three tests were comparable, suggesting that for this multi-level cyclic strain-controlled test, the smaller strain

ranges don't affect the macroscopic stabilized hysteresis loop in the largest strain range. It can be seen in Figure 3.20b that the peak stress reached during cycling is the same value (760 MPa) in all three tests. However, the multi-level test with loading history starts with a peak stress of 690 MPa when loaded to 1% strain in the first cycle due to the cyclic hardening that occurred in the previous levels (Figure 3.18). It should be noted that the material reaches much larger stress levels (760 MPa) than those obtained in the strain-controlled monotonic tests at 1% strain (less than 500 MPa) due to cyclic hardening.

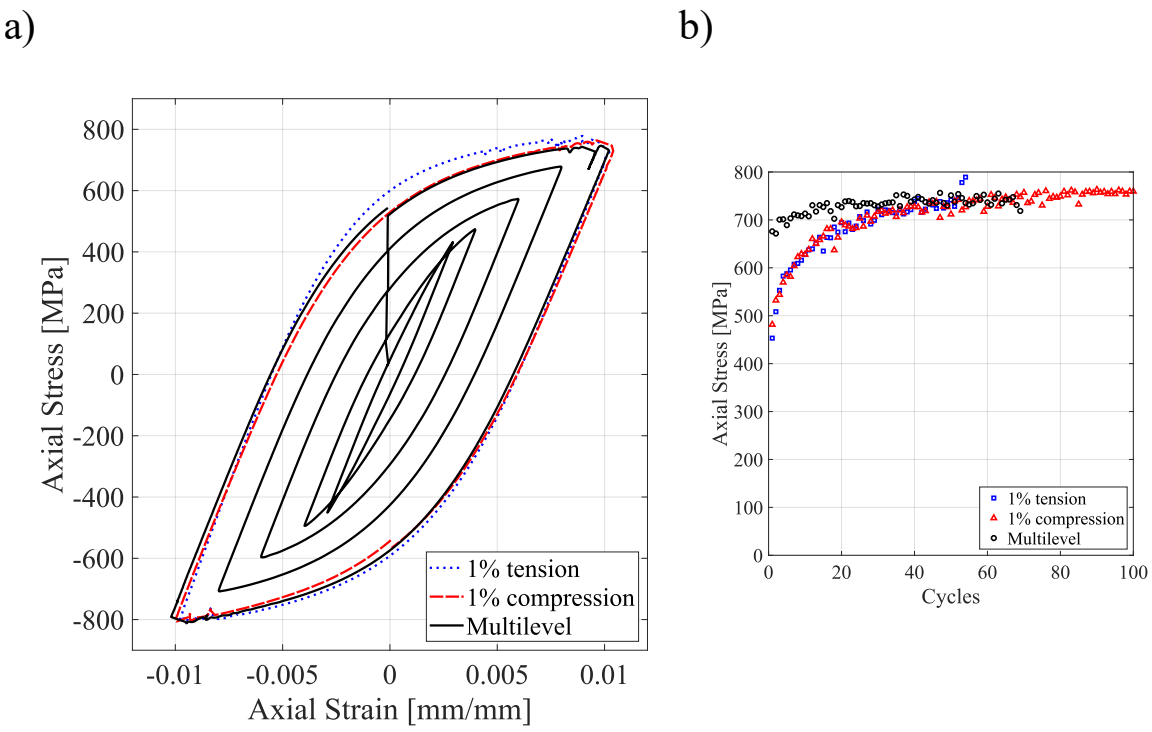

Figure 3.20: *Comparison of strain-controlled test results of a sample tested at ±1% and a sample tested at multiple-levels at 600°C .*

Force-controlled cyclic test results at non-zero mean stress to characterize cyclic inelastic behavior

Figure 3.21 shows results of the force-controlled cyclic tests from test #1, #3, and #4 in Table 3.4. A representative cyclic stress-strain response of a sample tested

under a constant mean stress and three consecutively increasing stress amplitudes (test #1a in light gray, 1b in dark gray, and 1c in black) is shown in Figure 3.21a. The maximum stresses reached at each cycle for the 100 applied cycles at all three stress amplitude levels (see test method schematic in Figure 3.15a) are given in Figure 3.21b as a function of the cycle number. Similarly, representative stress-strain and peak-stress evolution results for sample #4 and sample #3 (at the largest stress amplitude without loading history) are shown in Figures 3.21c-f. Line colors in these figures indicate the loading level (e.g. 4a in light gray, 4b in dark gray, 4c in black are the three stress amplitude levels applied on sample #4 (Table 3.4), as shown schematically in Figure 3.15a.

For Figures 3.21 a, c, and e, at each stress amplitude level and during each cycle, the sample yields in both tension and compression, resulting in hysteresis loops. The loading levels were chosen in order to elicit this yielding and produce these hysteresis loops. Figures 3.21b, d, f show that the maximum strains stabilize at all loading levels for samples 1, 3, and 4. In fact, this was the case for all of the tests listed in Table 3.4. This indicates that there is no net accumulation of plastic strain upon cycling (no ratchetting), and the relevant cyclic plastic behavior observed in the tests is deemed to be alternating plasticity.

In order to measure the severity of the cyclic plastic deformation (alternating plasticity) in these force-controlled cyclic tests and determine loading levels and inelastic responses that could be acceptable for design purposes, the evolution of hysteresis loop widths ($\delta\epsilon$) are monitored. This is because they correlate directly with the plastic work done per cycle (area within the hysteresis loop at each cycle) [146]. A hysteresis loop width of a cycle is calculated as the difference between the strain value obtained at the mean stress during loading and unloading of the cycle. Larger $\delta\epsilon$ values during cycling indicate alternating plasticity behavior is present that could result in failure of the material. When $\delta\epsilon$ decreases during cycling and

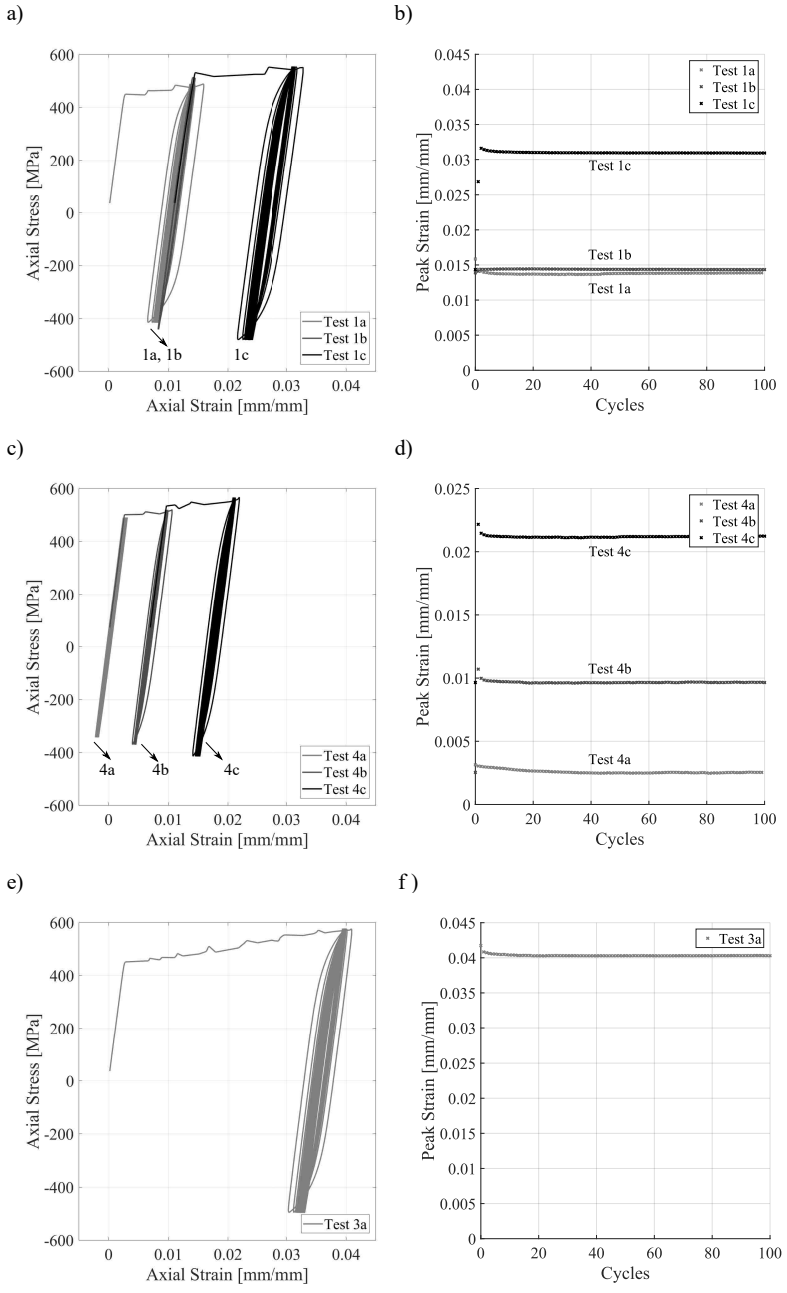

Figure 3.21: *Representative results for force-controlled cyclic tests at multiple stress amplitudes. Sample and test numbers are labeled according to Table 3.4.*

approaches zero, the implication is that elastic behavior is being recovered, and the material approaches a safe shakedown state.

Figure 3.22 shows the evolution of the hysteresis loop width results calculated at the mean stress value for each cycle. In this figure, results from test #1a-c (solid line, multi-level), test #2a-c (dashed line, repetition of test #1a-c multi-level), and test #3a (dotted line, sample tested at the largest stress amplitude from test #2c, but without loading history) are compared. The results show that during the loading cycles, the width of the hysteresis loops decreases. The results from the separate tests nearly coincide (solid, dashed, and dotted lines) with a maximum percent standard deviation of 10%. Thus, it is suggested that the test is repeatable and the effect of the loading history on the results is negligible (test 1a-c, 2a-c, 3a). Similarly, Figure 3.23 tracks $\delta\epsilon$ for tests #1, 4-6 and #7, 10, 11, respectively. Tests with small absolute mean stresses of 36 MPa (tests 4a, 5a, 6a, 10a, and 11a) have widths approaching zero (values around 1×10^{-5}) that may effectively reach shakedown.

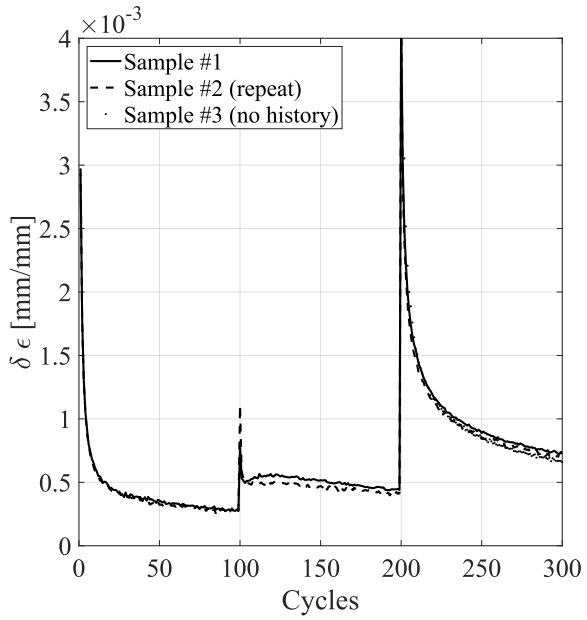

Figure 3.22: *Evolution of the hysteresis loop width during cycling.*

The same $\delta\epsilon$ analysis was done for the force-controlled cyclic tests listed in Table 3.4 to investigate the effect of the magnitude and sign of the mean stress on the evolution of the hysteresis loop widths with cycling (indicating the achievement of shakedown or alternating plasticity). Figure 3.23a compares the evolution of $\delta\epsilon$ from tests with a mean stress of 72 MPa (test #4a-c with solid line, #5a-c with dashed line, and #6a-c with dotted line) with a sample tested under a mean stress of 36 MPa (test #1a-c, red crosses). It is observed that while a good agreement between the tests #4-6 with the same mean stress (72 MPa) was achieved, the final $\delta\epsilon$ values were 2-3 times larger when the mean stress was smaller by half (36 MPa).

Similarly, Figure 3.23b shows the hysteresis loop evolution with cycles for sample #10 (solid line), sample #11 (dashed line) and sample #7 (red crosses). The results show that, similarly to the tensile mean stress cases, the test under a smaller compressive mean stress by half (-36 MPa, sample #7) resulted in 2-3.5 times larger final hysteresis loop widths. Note that the maximum absolute stress applied in these seven tests was the same (554 MPa). This supports the idea that monitoring maximum stress alone is not sufficient for design considerations. Instead, the cyclic inelastic behavior, and in particular whether effective shakedown or alternating plasticity is achieved, is determined by both the mean stress and stress amplitude. Furthermore, comparison of the plots in Figures 3.23a and b shows that the evolution of hysteresis loop width is not affected by the sign of the mean stress. In this way, inelastic shakedown design may be equally considered for cycling with tensile and compressive mean stresses.

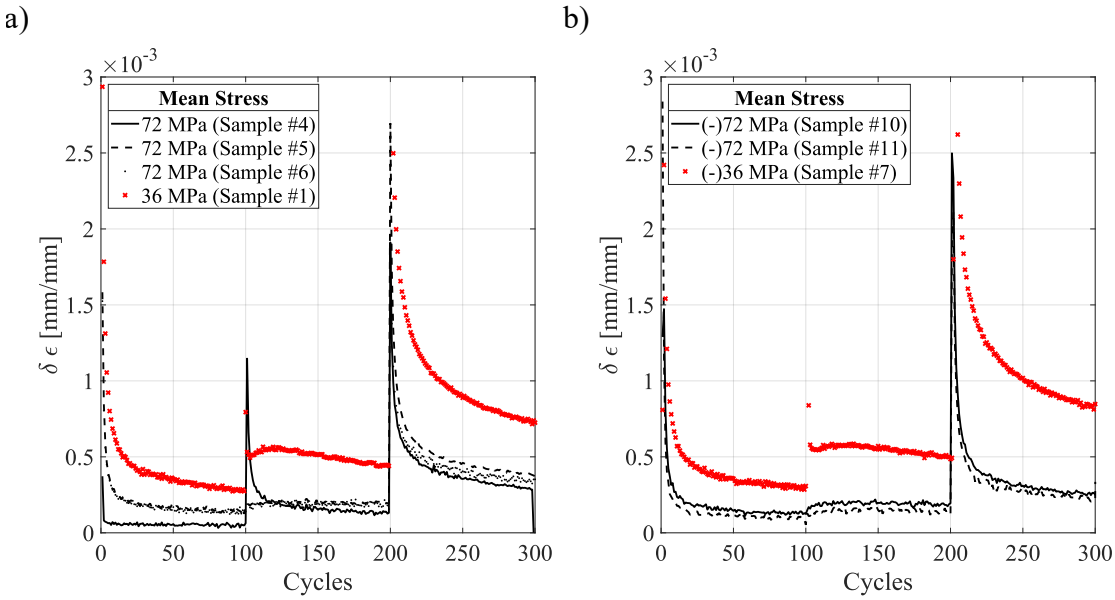

Figure 3.23: *Effect of mean stress on the hysteresis loop width results.*

While this is promising for inelastic design, DSA must also be considered and because of the large plastic strains that DSA may cause, in order to capitolize on shakedown, ways to suppress the DSA would be needed in order to reliably remain below allowable plastic strains. Unexpectedly, the strain levels reached in the first two levels overlapped for most of the multi-level force-controlled cyclic tests (an example of this is shown in Figure 7a). Three distinct strain levels were visible only for sample #4 (Figure 3.21c) and sample #8 (not shown). We believe that this is due to the DSA behavior observed during the initial loading to the maximum stress of each load level (a, b and c) in all of the cyclic tests (Figure 3.15a). In particular, sudden jumps in strain are seen due to DSA, creating a stair-like behavior in the plastic regime.

As there are large post-yielding strain rates generated by the DSA mechanism, the strain value at the peak of the first cycle (at all load levels) varies greatly (even among repeat tests). These sudden jumps result in large strain values (that are otherwise not expected) at the maximum stress of the first levels (level a) of the

tests, (Figure 3.15a). For instance, strain values of 0.3%, 1.4%, 1.5% and 1.6% were observed at 489 MPa in tests 1a-6a in Table 3.4, while based on the monotonic tests (Figure 3.17), a strain value of 0.3% was expected. It is surmised that as a sample experiences large deformation in the first test level (level a) due to DSA, when loaded to the second level (level b), the strain does not further increase noticeably, resulting in the apparent overlapping of the hysteresis loops for the two levels. The stress strain diagram in Figure 3.21e shows the results of test #3a (Table 3.4) where the loading condition is identical to the test #1c but without any loading history. It is seen from this figure that the DSA is active until the maximum load in the first cycle is reached for test #3a. The maximum strain level is higher than test #1c although the stresses are identical. This is again believed to be due to the DSA.

The experimental results in this chapter show that the cyclic inelastic behaviors of stainless steel 316L and IN625 involve time- and rate-dependent effects and whether the material shows shakedown response or not depends on the loading conditions (i.e. stress amplitude and mean stress for uniaxial cyclic tests). As it is not possible to perform cyclic tests at every loading combination, constitutive models are needed to develop FE-based Bree load-interaction diagrams over broader ranges of load space. With experimental validation, these FE-models could then be used to provide load-interaction diagrams and shakedown limits for structures with greater geometric and loading complexities. The following chapter gives an example of this to complement and aide in interpretation of the experimental SS 316L results presented.

Chapter 4

Finite Element Analysis for Shakedown and Cyclic Inelastic Behaviors

This chapter focuses on numerically determining shakedown limits and identifying cyclic inelastic behaviors for the room-temperature SS 316L tests complicated by the presence of creep in Chapter 3. Section 4.1.1 details the constitutive model used in the numerical analysis. Parameter identification for the constitutive model is presented in Section 4.1.2. Lastly, the numerical shakedown limits are compared with the experimental results from Chapter 3.

4.1 Phenomenological models for cyclic inelastic behavior

There has been considerable effort in developing phenomenological models to accurately simulate the cyclic plastic deformation (including ratchetting) of metals under uniaxial loading, but very few studies have addressed shakedown. At the same time,

micromechanical models (such as crystal plasticity) have also been developed and applied for cyclic plasticity analysis [147, 148]. However, as these approaches involve many inter-dependent variables and they require significant computational effort, they are beyond the scope of this dissertation. For SS 316L, many phenomenological models, considering isotropic and kinematic hardening combined with time-dependent creep deformation, have been used to investigate ratchetting behavior [83, 85, 86, 89–93, 97, 99, 149–153].

In contrast, most of the numerical shakedown studies in the literature use elastic-perfectly plastic material behavior as it provides simplicity and a conservative analysis. The more complex inelastic behaviors of metals in reality (including for example cyclic and kinematic hardening) have been shown to improve the shakedown performance of structures [154, 155]. Moreover, depending on material, temperature and loading rates, additional deformation modes such as creep and dynamic strain aging can be observed. This chapter presents an exploration of these behaviors and their interactions with shakedown behavior in order to more accurately determine safe inelastic loading limits of materials and structures. Based on results for SS 316L in Chapter 3 Figure 3.8a,b), it is clear that there is some limit beyond which unstable cyclic inelastic strain accumulation (dominated by creep) persists. We use a numerical model to find this effective shakedown limit at ambient conditions for a broad range of mean stresses and stress amplitudes.

Finite element analyses in this chapter were performed using the commercial software Abaqus 2016 (SIMULIA, Providence, RI). A single 1D element was used to simulate the uniaxial behavior with the constitutive relations explained below. Full cyclic elastoplastic analyses were performed in a static step with the Abaqus/Standard solver where nonlinear geometrical effects were neglected. This is a suitable assumption as the axial strains observed experimentally in the cyclic force-controlled tests in Chapter 3 were relatively small (below 2%).

4.1.1 Constitutive Model

In order to determine shakedown limits in the presence of ambient creep, a simple constitutive model for SS 316L that combines isotropic hardening with time-dependent creep behavior is used. It should be noted that, for the stress levels used in the experiments, we did not observe time-independent cyclic behaviors (alternating plasticity or ratchetting). The onset of alternating plasticity (thin hysteresis loops) are visible only at the largest amplitude tests at ambient conditions (Figure 3.8e). At larger amplitudes than those considered in this study, the hysteresis loops are expected to be larger which would require the use of combined isotropic/kinematic hardening models.

The parameters describing isotropic hardening for the constitutive model in this study can be obtained from the monotonic tests performed in strain control or from the cyclic tests performed in force control. As the material is rate-dependent, the responses under strain control and force control conditions may differ slightly as it is difficult to obtain the same deformation rate (Figure 4.1). In Figure 4.1, the data points for the force-controlled tests correspond to the stress and strain values at the first stress peaks of the three stages of the cyclic tests in Figure 3.8a, c, and e. A Ramberg-Osgood type stress-strain relation is used to describe the material behavior:

$$\epsilon = \frac{\sigma}{E} + \alpha \left(\frac{\sigma}{E}\right) \left(\frac{\sigma}{\sigma_y}\right)^{(n-1)}, \tag{4.1}$$

where α and n are the material parameters and σ_y is the 0.2% yield stress given in Table 3.2. The parameters of the hardening model were determined based on force-controlled cyclic tests ($\alpha = 0.9563$, $n = 8.4711$) and are shown in Figure 4.1 (dashed black line for RO-force) to compare with the monotonic test results (solid black line). The difference between the strain-controlled monotonic and other tests becomes more significant in the large plastic strain region. At a large stress value,

force-controlled tests give smaller strain values compared to the monotonic test.

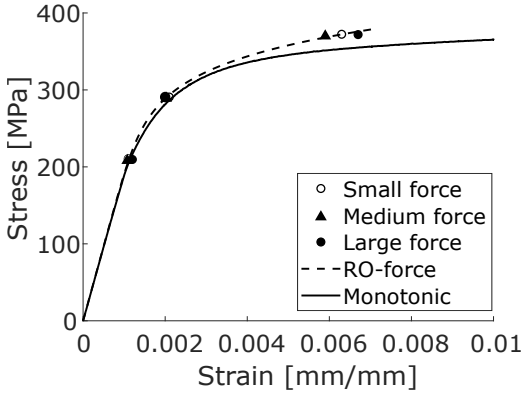

Figure 4.1: *Comparison of isotropic hardening of the material in monotonic and force-controlled cyclic tests corresponding to Figure 3.8a ("small force"), Figure 3.8c ("medium force"), and Figure 3.8e ("large force"). Superimposed is the numerical result ("RO-force") based on the Ramberg-Osgood type model (Eq. 4.1).*

The other component of the constitutive model simulates the time-dependent creep deformation. In order to combine the hardening and creep behaviors, material models available in Abaqus are used. A strain hardening form of the creep power law (based on the Norton-Bailey creep model) is used:

$$\dot{\epsilon}^{cr} = \left(A\sigma^n \left((m+1)\,\epsilon^{cr}\right)^m\right)^{\frac{1}{m+1}}, \tag{4.2}$$

where A, m and n are the creep model parameters to be calibrated using experimental data, described next [72].

4.1.2 Creep model parameter identification

The parameters of the creep model (Eq. 4.2) are determined based on the experimental data shown in Figure 3.13a. An optimization method based on a Levenberg-Marquardt algorithm was used to identify the creep parameters as $A = 3.023 \times 10^{-28}$ $MPa^{-1}s^{-1}$, $n = 9.417$, $m = -0.8036$. Figure 4.2a shows the creep strains obtained with the optimized parameters, and compares it with experimental results during the multiple level creep test (Section 3.3.1, Figure 3.5). When combined with the

material hardening, the numerical model agrees well with the experimental data as shown in Figure 4.2b.

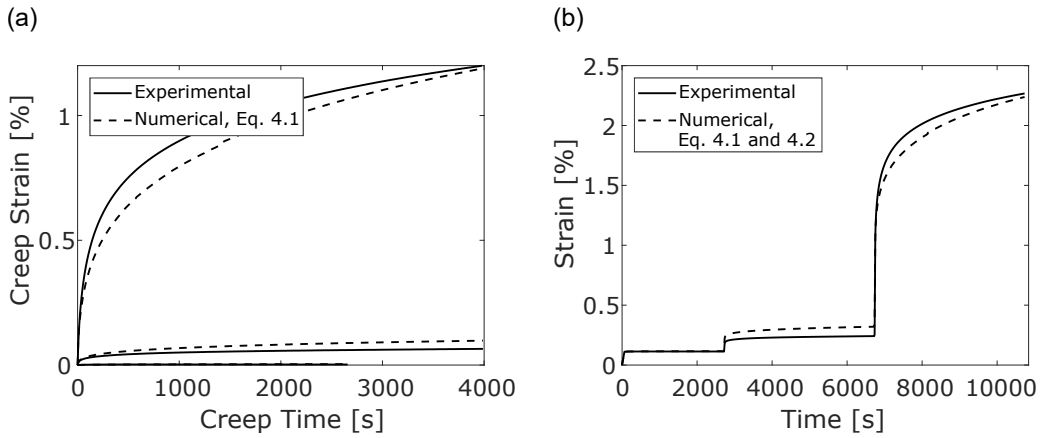

Figure 4.2: *Comparison of strains from numerical model and experimental results. a) Creep-only numerical model, Eq. 4.1, and b) combined hardening and creep model, Eqs 4.1 and 4.2.*

The combined numerical model with both hardening and creep (Eqs. 4.1 and 4.2) is used in the following section to investigate the shakedown limit of the material, below which a stable cyclic response is achieved.

4.2 Inelastic design diagrams

In order to determine the shakedown limit of the SS316 material under the room-temperature uniaxial loading conditions from Section 3.3.1, a parametric analysis using the numerical model described in Section 4.1.1 was performed. A series of different mean stresses below the 5% cut-off limit line in Figure 3.7a and stress amplitudes below the largest experimental value ($\sigma_{amp}/\sigma_y^o < 2.8$, Section 3.3.1, Figure 3.7a) were probed. For each stress amplitude, 150 load cycles were repeated at increasing mean stress levels with increments of 10 MPa. The resulting peak strains during stress cycles were monitored to determine the limiting stress values above which a continuous accumulation of plastic strain with cycling was observed. As

explained in Section 3.3.2 for SS 316L, cyclic plastic strain accumulation was dominated by creep deformation at ambient conditions. As creep occurs even at stresses below the yield limit of the material, a threshold for the allowable strain (or strain increment per cycle) has to be defined.

In a very limited number of studies on uniaxial cyclic tests on metals, criteria that can be readily experimentally measured have been proposed to distinguish shakedown behavior from inadmissible continuous plastic strain accumulation. Pelissier *et al.* defined the shakedown criterion as a measured axial strain increment smaller than 0.1% between cycles 50 and 100 (i.e. $2 \times 10^{-5}/cycle$) [74]. Similarly Ruggles and Krempl considered the deformation of the material stable if a ratchetting strain per cycle below 2×10^{-5} after 100 cycles is observed [149, 156]. Another approach for shakedown determination is suggested by Wolters *et al.*. They proposed to use the slope of the plastic strain increment against cycle number in a log-log plot. If the slope approximated by a straight line fit to the log-log data is below -1, they assume that the cyclic inelastic deformation stabilizes (shakedown). all of these criteria would suggest that the behaviors we observed in the ambient force-controlled tests (Section 3.4.2) all reached shakedown, even though continuous accumulation of inelastic strain is apparent.

It is not trivial to determine one shakedown criterion that is suitable for different applications; a structure's cyclic inelastic response depends on the material, loading conditions, environmental effects etc. For this reason, in this section we compare maximum allowable stresses based on two different criteria, ($2 \times 10^{-5}/cycle$ and a more conservative $2 \times 10^{-6}/cycle$). An example of the determination of the shakedown limit is demonstrated in Figure 4.3 for one stress amplitude level at ambient conditions which corresponds to Figure 3.8. A parametric finite element analysis was performed at a constant stress amplitude corresponding to $\sigma_{amp}/\sigma_y^o = 0.67$. The analysis is repeated at increasing mean stress levels (240 - 320 MPa in incre-

ments of 10 MPa) and the evolution of the maximum strain over $N = 150$ cycles at each mean stress level is plotted in this figure (dashed lines). For comparison, peak strains from the multi-level force-controlled cyclic test at the same stress magnitude ($\sigma_{amp}/\sigma_y^o = 0.67$, Figure 3.8b) are shown in the figure (solid lines). Maximum allowable stress limits obtained from the numerical shakedown analysis are indicated on Figure 4.3 by red arrows and listed in Table 4.1.

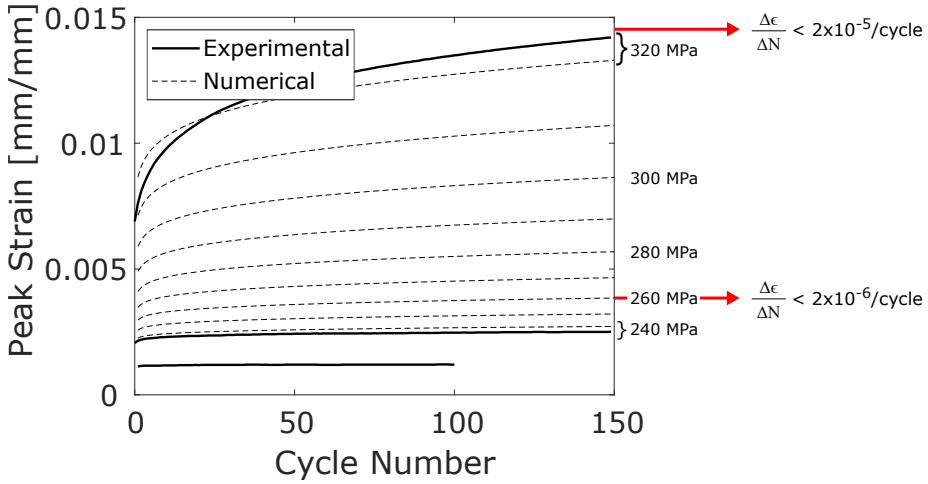

Figure 4.3: *Parametric numerical analysis results between mean stresses of* $\sigma_{mean} = 240 - 320$ *MPa for shakedown determination (refer to Figure 3.8b for experimental lines).*

Design standards for some applications that use stainless steel 316L enforce specific limits on the maximum accumulated inelastic strains in structures. For instance, the ORNL nuclear standard gives maximum allowable strain limits at critical locations (strains extrapolated to the end-of-life of the structure as: 1.0% average through the thickness, 2.0% at the surface due to an equivalent linear distribution of strain through the thickness, and 5.0% at all locations) [2]. Hence it is also important to examine the time or number of cycles that would create specific amounts of inelastic strain when there is a continuous increase in the strain increment per cycle. Table 4.1 shows the number of cycles that would result in 1% and 2% inelastic strain at the maximum allowable stresses based on the two shakedown criteria. The approach for these calculations is conservative in that in order to find the # of cycles required

to accumulate 1% and 2% strain, the strain increment after 150 cycles was assumed constant (no further stabilization of creep deformation is assumed).

Table 4.1: *Shakedown determination criteria for the design of structures under creep effects.*

Criterion	Max. Allowable Stress [MPa]	# of cycles to 1% strain	# of cycles to 2% strain
$\frac{\Delta\epsilon}{\Delta N} < 2 \times 10^{-5}/cycle$	370	≈ 500	≈ 1000
$\frac{\Delta\epsilon}{\Delta N} < 2 \times 10^{-6}/cycle$	300	≈ 5000	≈ 10000

This procedure was also used to determine the shakedown limit at ambient conditions within the loading space considered in Figure 3.7 based on the shakedown criterion of $\frac{\Delta\epsilon}{\Delta N} < 2 \times 10^{-6}/cycle$ (shown in Figure 4.4 with blue squares). Stress amplitudes above the largest experimental value ($\sigma_{amp}/\sigma_y^o = 2.7$) are not considered and are grayed out in Figure 4.4. This is done because undesirable time-independent cyclic plastic behaviors (ratchetting, alternating plasticity) are expected and the numerical model used in this study is incapable of simulating these behaviors.

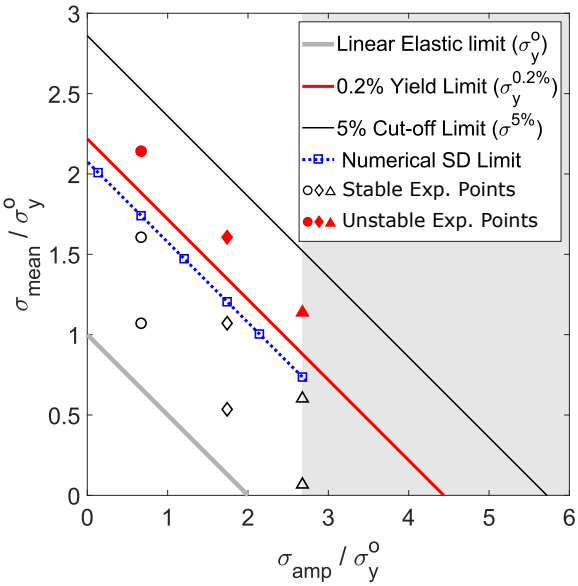

Figure 4.4: *Bree load interaction diagram showing the numerical shakedown (SD) limit of the material at ambient conditions.*

The load interaction diagram in Figure 4.4 reveals the benefit of considering

shakedown behavior in the design process. At room temperature, the shakedown limit doubles the feasible design space based on the linear elastic limit of the material (Figure 4.4). Above the shakedown limit, the material response becomes inadmissible due to unstable creep deformation.

Chapter 5

Conclusions

In this dissertation, the shakedown behavior of metals and metallic structures subjected to cyclic mechanical and thermomechanical loads has been explored analytically, numerically and experimentally. Specific case studies have leveraged shakedown design to identify weight-savings, sizing guides, and durability benefits that are relevant for aerospace and civil engineering applications. The key conclusions follow.

For some thin-walled thermostructural components that are prone to thermal buckling or have curvilinear shapes (combustor liners, rocket nozzles, stiffeners) this dissertation was the first to establish beneficial interactions of geometric nonlinearity induced by thermal buckling and cyclic elastoplastic shakedown both. In particular, shakedown limits for built-in-beams that are uniformly heated and cooled while subject to constant distributed loads were analytically and numerically determined and used to construct Bree load-interaction diagrams for design purposes. It was found that considering shakedown behavior extended the design space by 2.5-4 times for large aspect ratio beams.

This dissertation also provides the first experimental studies of uniaxial macroscopic shakedown for stainless steel 316L (at ambient and 600^oC) and Inconel 625 (at

600^oC). The effects of creep and dynamic strain aging on the shakedown performance were investigated for these materials.

It was found that for stainless steel 316L at ambient conditions, creep contributes to the cyclic inelastic strain accumulation. Finite element analysis was used to assist in determining shakedown limits in the presence of creep; shakedown occured at maximum stress levels up to two times the linear elastic limit in this study. At the elevated temperature of 600^oC, dynamic strain aging was present and there was negligible creep. At 600^oC, shakedown occured at maximum stress levels up to 4 times the linear elastic limit. The identified behaviors for the testing programs at ambient and 600^oC were included in Bree load-interaction diagrams as design guides.

A Bree load-interaction diagram was also created for the uniaxial cycling of Inconel 625 at 600^oC, indicating the domains for shakedown or alternating plasticity behavior (no cyclic accumulation of inelastic strain was found). At 600^oC, shakedown occured at maximum stress levels up to 1.4 times the linear elastic limit. However, the uniaxial shakedown behavior was affected by both stress amplitude and mean stress, indicating that maximum stress alone could not be used as a design criterion.

Future Work

Future work should focus on providing component-level testing and direct experimental validation for the numerical case studies presented in Chapter 2. Auxetic structures would be ideal candidates to leverage full-field measurements to identify structural shakedown. The direct experimental validation of these case studies would provide valuable insight regarding the practical implementation and incorporation of shakedown considerations in the design process.

In addition, a better understanding of the micromechanical mechanisms responsible for material and structural shakedown is needed. Studies at the micro, meso,

and macro scales should be jointly considered to establish a multiscale methodology for shakedown design. Such a framework could be used to direct the development of materials to promote shakedown behavior. A key step in achieving this would be the use of in-situ experimental techniques.

Bibliography

[1] J Bree. Elastic-plastic behaviour of thin tubes subjected to internal pressure and intermittent high-heat fluxes with application to fast-nuclear-reactor fuel elements. *The Journal of Strain Analysis for Engineering Design*, 2(3):226–238, 1967. ISSN 0309-3247. doi: 10.1243/03093247V023226.

[2] RDT Standard. Rdt f9-5t guidelines and procedures for the design of nuclear system components at elevated temperatures. *USAEC, Division of Reactor Research and Development*, 1974.

[3] *ASME Boiler and Pressure Vessel Code: Section VIII. Rules for Construction of Pressure Vessels*. 1940.

[4] British Standards Institute. *BS 5500: British standard specification for fusion welded pressure vessels*. London, 1996.

[5] Nuclear Electric PLC. *R5 Assessment Procedure for the high temperature response of structures*. 1990.

[6] J Bree. Incremental growth due to creep and plastic yielding of thin tubes subjected to internal pressure and cyclic thermal stresses. *The Journal of Strain Analysis for Engineering Design*, 3(2):122–127, 1968.

[7] M. Abdel-Karim. Shakedown of complex structures according to various hard-

ening rules. *International Journal of Pressure Vessels and Piping*, 82:427–458, 2005. doi: 10.1016$/$j.ijpvp.2005.01.007.

[8] A Oueslati and G De Saxcè. Static shakedown theorem for solids with temperature-dependent elastic modulus. In *Limit States of Materials and Structures*, pages 157–178. Springer, 2009.

[9] Michael Peigney. Shakedown of elastic-perfectly plastic materials with temperature-dependent elastic moduli. *Journal of the Mechanics and Physics of Solids*, 71:112–131, 2014.

[10] Haofeng Chen. Lower and upper bound shakedown analysis of structures with temperature-dependent yield stress. *Journal of Pressure Vessel Technology*, 132(1):011202, 2010.

[11] Guido Borino. Consistent shakedown theorems for materials with temperature dependent yield functions. *International journal of solids and structures*, 37 (22):3121–3147, 2000.

[12] Hartwig Hubel. Basic conditions for material and structural ratcheting. *Nuclear Engineering and Design*, 162(1):55–65, 1996.

[13] Hartwig Hübel and Bastian Vollrath. Limited versus unlimited strain accumulation due to ratcheting mechanisms. *Journal of Pressure Vessel Technology*, 141(3):031206, 2019.

[14] ARS Ponter, AD Hearle, and KL Johnson. Application of the kinematical shakedown theorem to rolling and sliding point contacts. *Journal of the Mechanics and Physics of Solids*, 33(4):339–362, 1985. URL `http://www.sciencedirect.com/science/article/pii/002250968590033X`.

[15] M. R. Begley and a. G. Evans. Progressive Cracking of a Multilayer System Upon Thermal Cycling. *Journal of Applied Mechanics*, 68(4):513, 2001. ISSN 00218936. doi: 10.1115/1.1379529. URL `http://appliedmechanics.asmedigitalcollection.asme.org/article.aspx?articleid=1414328`.

[16] Yan Zhuang and Kangyu Wang. Shakedown solutions for pavement structures with von mises criterion subjected to hertz loads. *Road Materials and Pavement Design*, 19(3):710–726, 2018.

[17] Michaël Peigney. On shakedown of shape memory alloys structures. *Annals of Solid and Structural Mechanics*, 6(1-2):17–28, 2014.

[18] WT Koiter. General theorems for elastic-plastic solids. *Progress in solid mechanics*, pages 167–221, 1960.

[19] Michael Peigney. Shakedown of elastic-perfectly plastic materials with temperature-dependent elastic moduli. *Journal of the Mechanics and Physics of Solids*, 71:112–131, 2014.

[20] D Weichert. Shakedown at finite displacements; a note on melan's theorem. *Mechanics Research Communications*, 11(2):121–127, 1984.

[21] Dieter Weichert and Alan Ponter. A historical view on shakedown theory. In *The History of Theoretical, Material and Computational Mechanics-Mathematics Meets Mechanics and Engineering*, pages 169–193. Springer, 2014.

[22] HF Chen and Alan RS Ponter. Shakedown and limit analyses for 3-d structures using the linear matching method. *International Journal of Pressure Vessels and Piping*, 78(6):443–451, 2001.

[23] Hien V Do and H Nguyen-Xuan. Limit and shakedown isogeometric analy-

sis of structures based on bézier extraction. *European Journal of Mechanics-A/Solids*, 63:149–164, 2017.

[24] B Simoens, M.H. Lefebvre, R.E. Nickell, and F. Minami. Experimental demonstration of shakedown in a vessel submitted to impulsive loading. *Journal of Pressure Vessel Technology*, 134:1–6, 2012. doi: 10.1115/1.4003824. URL http://materialstechnology.asmedigitalcollection.asme.org/article.aspx?articleid=1661591.

[25] M. Heitzer, M. Staat, H. Reiners, and F. Schubert. Shakedown and ratchetting under tension–torsion loadings: analysis and experiments. *Nuclear engineering and ...*, 225(1):11–26, October 2003. ISSN 00295493. doi: 10.1016/S0029-5493(03)00134-1. URL http://linkinghub.elsevier.com/retrieve/pii/S0029549303001341http://www.sciencedirect.com/science/article/pii/S0029549303001341.

[26] H Lang, K Wirtz, M Heitzer, M Staat, and R Oettel. Cyclic plastic deformation tests to verify FEM-based shakedown analyses. *Nuclear Engineering and Design*, 206(2–3):235–247, 2001. ISSN 0029-5493. doi: http://dx.doi.org/10.1016/S0029-5493(00)00438-6. URL http://www.sciencedirect.com/science/article/pii/S0029549300004386.

[27] HW Ng, DJ Brookfield, and DN Moreton. A technique for conducting shakedown tests at elevated temperatures. *Strain*, 20(1):7–14, 1984.

[28] O Mahrenholtz, K Leers, and J Konig. Shakedown of tubes: a theoretrical analysis and experimental investigation. *Pergamon Press, Metal Forming and Impact Mechanics*, pages 155–172, 1985.

[29] K Leers, W Klie, JA König, and O Mahrenholtz. Experimental investigations

on shakedown of tubes. In *Plasticity Today*, pages 259–275. Elsevier London, 1985.

[30] Joshua D Deaton and Ramana V Grandhi. Significance of geometric nonlinearity in the design of thermally loaded structures. *Journal of Aircraft*, 2014.

[31] Manav Bhatia and Philip Beran. Design of thermally-stressed panels subject to transonic flutter constraints. In *17th AIAA/ISSMO Multidisciplinary Analysis and Optimization Conference*, page 4119, 2016.

[32] David John Neiferd, Ramana V Grandhi, Joshua D Deaton, Philip S Beran, and Manav Bhatia. A nonlinear finite element analysis capability for the optimization of thermoelastic structures. In *58th AIAA/ASCE/AHS/ASC Structures, Structural Dynamics, and Materials Conference*, page 1302, 2017.

[33] Juozas Atkočiūnas, Adam Borkowski, and Jan A König. Improved bounds for displacements at shakedown. *Computer Methods in Applied Mechanics and Engineering*, 28(3):365–376, 1981.

[34] Morteza AM Torkamani and Mohammad R Pajand. Plastic cyclic analysis using linear yield surface. *Journal of engineering mechanics*, 110(5):776–793, 1984.

[35] F Giambanco, L Palizzolo, and C Polizzotto. Optimal shakedown design of beam structures. *Structural and Multidisciplinary Optimization*, 8(2):156–167, 1994.

[36] F Giambanco and L Palizzolo. Computation of bounds on chosen measures of real plastic deformation for beams. *Computers & structures*, 61(1):171–182, 1996.

[37] F Tin-Loi. Optimum shakedown design under residual displacement constraints. *Structural and Multidisciplinary Optimization*, 19(2):130–139, 2000.

[38] H Mahbadi, AR Gowhari, and MR Eslami. Elastic-plastic-creep cyclic loading of beams using the prager kinematic hardening model. *The Journal of Strain Analysis for Engineering Design*, 39(2):127–136, 2004.

[39] Luigi Palizzolo. Optimization of continuous elastic perfectly plastic beams. *Computers & structures*, 82(4):397–411, 2004.

[40] Giovanni Garcea, Giampaolo Armentano, Salvatore Petrolo, and Raffaele Casciaro. Finite element shakedown analysis of two-dimensional structures. *International journal for numerical methods in engineering*, 63(8):1174–1202, 2005.

[41] A Nayebi. Bree's interaction diagram of beams with considering creep and ductile damage. *Structural Engineering and Mechanics*, 30(6):665–678, 2008.

[42] A Nayebi and R El Abdi. Shakedown analysis of beams using nonlinear kinematic hardening materials coupled with continuum damage mechanics. *International Journal of Mechanical Sciences*, 50(8):1247–1254, 2008.

[43] H Nguyen-Xuan, T Rabczuk, T Nguyen-Thoi, TN Tran, and N Nguyen-Thanh. Computation of limit and shakedown loads using a node-based smoothed finite element method. *International Journal for Numerical Methods in Engineering*, 90(3):287–310, 2012.

[44] R Adibi-Asl and W Reinhardt. Ratcheting with no thermal bending and membrane stress. In *ASME 2016 Pressure Vessels and Piping Conference*, pages V01AT01A034–V01AT01A034. American Society of Mechanical Engineers, 2016.

[45] M Megahed, ARS Ponter, and CJ Morrison. A theoretical and experimental investigation of material ratchetting rates in a bree beam element. *International journal of mechanical sciences*, 25(12):917–933, 1983.

[46] R Hamilton and JT Boyle. Simplified lower bound limit analysis of transversely loaded thin plates using generalised yield criteria. *Thin-walled structures*, 40 (6):503–522, 2002.

[47] Stephen Timoshenko, Gleason Harvey MacCullough, et al. Elements of strength of materials. 1949.

[48] E. Melan. Der spannungszustand eines mises-henckyschen kontinuums bei veraenderlicker belastung. *Sitzber. Akad. Wiss.*, 147:73–78, 1938.

[49] A.F. Bower. *Applied mechanics of solids*. CRC Press, 2009.

[50] J.A. König. *Shakedown of elastic-plastic structures*. Elsevier, The Netherlands, 1987.

[51] Jagabanduhu Chakrabarty. *Theory of plasticity*. Butterworth-Heinemann, 2012.

[52] JB Choi and RS Lakes. Non-linear properties of polymer cellular materials with a negative poisson's ratio. *Journal of Materials Science*, 27(17):4678–4684, 1992.

[53] JB Choi and RS Lakes. Fracture toughness of re-entrant foam materials with a negative poisson's ratio: experiment and analysis. *International Journal of fracture*, 80(1):73–83, 1996.

[54] Ivan I Argatov, Raúl Guinovart-Díaz, and Federico J Sabina. On local indentation and impact compliance of isotropic auxetic materials from the continuum

mechanics viewpoint. *International Journal of Engineering Science*, 54:42–57, 2012.

[55] VL Coenen and KL Alderson. Mechanisms of failure in the static indentation resistance of auxetic carbon fibre laminates. *physica status solidi (b)*, 248(1): 66–72, 2011.

[56] Roderic Lakes. Advances in negative poisson's ratio materials. *Advanced Materials*, 5(4):293–296, 1993.

[57] Kenneth E Evans and Andrew Alderson. Auxetic materials: functional materials and structures from lateral thinking! *Advanced materials*, 12(9):617–628, 2000.

[58] Ken E Evans. Auxetic polymers: a new range of materials. *Endeavour*, 15(4): 170–174, 1991.

[59] Alderson Alderson and KL Alderson. Auxetic materials. *Proceedings of the Institution of Mechanical Engineers, Part G: Journal of Aerospace Engineering*, 221(4):565–575, 2007.

[60] S Mohsenizadeh, R Alipour, M Shokri Rad, A Farokhi Nejad, and Z Ahmad. Crashworthiness assessment of auxetic foam-filled tube under quasi-static axial loading. *Materials & Design*, 88:258–268, 2015.

[61] Shujuan Hou, Taiqu Liu, Zhidan Zhang, Xu Han, and Qing Li. How does negative poissons ratio of foam filler affect crashworthiness? *Materials & Design*, 82:247–259, 2015.

[62] Michael Taylor, Luca Francesconi, Miklós Gerendás, Ali Shanian, Carl Carson, and Katia Bertoldi. Low porosity metallic periodic structures with negative poisson's ratio. *Advanced Materials*, 26(15):2365–2370, 2014.

[63] Farhad Javid, Jia Liu, Ahmad Rafsanjani, Megan Schaenzer, Minh Quan Pham, David Backman, Scott Yandt, Matthew C Innes, Christopher Booth-Morrison, Miklos Gerendas, et al. On the design of porous structures with enhanced fatigue life. *Extreme Mechanics Letters*, 16:13–17, 2017.

[64] Jeremy Bleyer, Duc Toan Pham, and Patrick De Buhan. Failure design of high-rise concrete panels under fire loading. *Proceedings of the ICE-Engineering and Computational Mechanics*, 168(4):178–185, 2015.

[65] Jérémy Bleyer, Duc Toan Pham, Patrick De Buhan, and Céline Florence. Yield design of periodically heterogeneous plates. In *Direct Methods for Limit and Shakedown Analysis of Structures*, pages 143–158. Springer, 2015.

[66] Marialaura Malena and Raffaele Casciaro. Finite element shakedown analysis of reinforced concrete 3d frames. *Computers & Structures*, 86(11-12):1176–1188, 2008.

[67] Sidney A Guralnick and Abbes Yala. Plastic collapse, incremental collapse, and shakedown of reinforced concrete structures. *Structural Journal*, 95(2): 163–174, 1998.

[68] Piotr Alawdin and George Bulanov. Shakedown of composite frames taking into account plastic and brittle fracture of elements. *Civil and Environmental Engineering Reports*, 15(4):5–21, 2015.

[69] P Alawdin and L Liepa. Optimal shakedown analysis of plane reinforced concrete frames according to eurocodes. *International Journal of Mechanics and Materials in Design*, 13(2):253–266, 2017.

[70] Michael Bogomolny and Oded Amir. Conceptual design of reinforced concrete structures using topology optimization with elastoplastic material modeling.

International journal for numerical methods in engineering, 90(13):1578–1597, 2012.

[71] S Rizzo, R Spallino, and G Giambanco. Shakedown optimal design of reinforced concrete structures by evolution strategies. *Engineering Computations*, 17(4): 440–458, 2000.

[72] ABAQUS. V2016, online documentation help, theory manual: Dassault systms, 2016.

[73] BS EN. 1-2: 2002 eurocode 1: Actions on structurespart 1-2: General actionsactions on structures exposed to fire. *British Standards*, 1991.

[74] A. Pellissier-Tanon, J. L. Bernard, C. Amzallag, and P. Rabbe. Evaluation of the Resistance of Type 316 Stainless Steel Against Progressive Deformation. In *Low-Cycle Fatigue and Life Prediction, ASTM STP 770*, pages 69–80. 1982.

[75] Dale G Eyre and TV Galambos. Shakedown tests on steel bars and beams. *Journal of the Structural Division*, 1970.

[76] O Mahrenholtz, K Leers, and JA König. Shakedown of tubes: A theoretical analysis and experimental investigation. In *Metal Forming and Impact Mechanics*, pages 155–172. Elsevier, 1985.

[77] E Procter and RF Flinders. Shakedown investigations on partial penetration welded nozzles in a spherical shell. *Nuclear Engineering and Design*, 8(1): 171–185, 1968.

[78] MG Barker, PM Bergson, CE French, RT Leon, TV Galambos, and FW Klaiber. Shakedown tests of one-third–cale composite bridge. *Journal of Bridge Engineering*, 1(1):2–9, 1996.

[79] Roberto T Leon and Daniel J Flemming. Experimental verification of shakedown approaches for bridge design. *Transportation research record*, 1594(1): 50–56, 1997.

[80] ASTM Standard. E8. standard test method for tension testing of metallic materials. *West Conshohocken (USA): ASTM*, 2004.

[81] ASTM Standard. A370, standard test methods and definitions for mechanical testing of steel products. *West Conshohocken, PA: ASTM International*, 2005.

[82] ASTM Standard. E466: Standard practice for conduction force controlled constant amplitude axial fatigue test of metallic materials, vol. 03.01. *Annual Book of ASTM Standards, West Conshohocken*, 2002.

[83] C. S. White, C. A. Bronkhorst, and L. Anand. An improved isotropic-kinematic hardening model for moderate deformation metal plasticity. *Mechanics of Materials*, 10(1-2):127–147, 1990. ISSN 01676636. doi: 10.1016/0167-6636(90)90023-9.

[84] E G Ellison. Thermal-mechanical strain cyclicng for a 1 CrMoV ferrtici steel and two 316 stainless steels. *Fatigue & fracture of Engineering Materials and Structures*, 17(I):39–51, 1994.

[85] P Delobelle, P Robinet, and L Bocher. Experimental study and phenomenological modelization of ratchet under uniaxial and biaxial loading on an austenitic stainless steel. *International Journal of Plasticity*, 11(4):295–330, 1995. ISSN 0749-6419. doi: http://dx.doi.org/10.1016/S0749-6419(95)00001-1. URL `http://www.sciencedirect.com/science/article/pii/S0749641995000011`.

[86] J Schwertel and B Schinke. Automated Evaluation of Material Parameters

of Viscoplastic Constitutive Equations. *Journal of Engineering Materials and Technology*, 118(3):273–280, 1996. ISSN 15288889. doi: 10.1115/1.2806805.

[87] Jaroslav Polák, Farouk Fardoun, and Suzanne Degallaix. Effective and internal stresses in cyclic straining of 316 stainless steel. *Materials Science and Engineering A*, 215(1-2):104–112, 1996. ISSN 09215093. doi: 10.1016/0921-5093(96)10373-7.

[88] A. Haupt, D. Munz, W. Scheibe, B. Schinke, R. Schmitt, and V. Sklenicka. High temperature creep and cyclic deformation behaviour of AISI 316 L(N) austenitic steel and its modelling with unified constitutive equations. *Nuclear Engineering and Design*, 162:13–20, 1996.

[89] M. P. O'Donnell, S. K. Bate, I. Bretherton, D. N. Gladwin, and J. P. Hayes. Use of conventional stress-strain data to develop parameters for an advanced constitutive model. *Materials at High Temperatures*, 19(4):215–223, 2002. ISSN 09603409.

[90] Yung Chuan Chiou and Ming Chuen Yip. Effect of mean strain level on the cyclic stress-strain behavior of AISI 316 stainless steel. *Materials Science and Engineering A*, 354(1-2):270–278, 2003. ISSN 09215093. doi: 10.1016/S0921-5093(03)00016-9.

[91] Paul Van Eeten and Fred Nilsson. Constant and variable amplitude cyclic plasticity in 316l stainless steel. *Journal of Testing and Evaluation*, 34(4): 298–311, 2006.

[92] Yannis F. Dafalias, Kyriakos I. Kourousis, and George J. Saridis. Multiplicative AF kinematic hardening in plasticity. *International Journal of Solids and Structures*, 45(10):2861–2880, 2008. ISSN 00207683. doi: 10.1016/j.ijsolstr.2008.01.001.

[93] Y P Gong, C J Hyde, W Sun, and T H Hyde. Determination of material properties in the Chaboche unified viscoplasticity model. *Proceedings of the Institution of Mechanical Engineers, Part L: Journal of Materials: Design and Applications*, 224:19–29, 2009. ISSN 1464-4207. doi: 10.1243/14644207JMDA273.

[94] A. Dutta, S. Dhar, and S. K. Acharyya. Material characterization of SS 316 in low-cycle fatigue loading. *Journal of Materials Science*, 45(7):1782–1789, 2010. ISSN 00222461. doi: 10.1007/s10853-009-4155-7.

[95] C. J. Hyde, W. Sun, and S. B. Leen. Cyclic thermo-mechanical material modelling and testing of 316 stainless steel. *International Journal of Pressure Vessels and Piping*, 87(6):365–372, 2010. ISSN 03080161. doi: 10.1016/j.ijpvp.2010.03.007.

[96] R. Hormozi, F. Biglari, and K. Nikbin. Experimental study of type 316 stainless steel failure under LCF/TMF loading conditions. *International Journal of Fatigue*, 75:153–169, 2015. ISSN 01421123. doi: 10.1016/j.ijfatigue.2015.02.014.

[97] Liang Hsiung Chou, Yung Chuan Chiou, Chia Chin Wu, and Ying Jen Huang. Predictions of stress-strain curve and fatigue life for AISI 316 stainless steel in cyclic straining. *Journal of Marine Science and Technology (Taiwan)*, 24(3):426–433, 2016. ISSN 10232796. doi: 10.6119/JMST-015-0820-1.

[98] A Haupt and B Schinke. Experiments on the Ratchetting Behavior of AISI316L (N) Austenitic Steel at Room Temperature. *Journal of Engineering Materials and Technology*, 118(3):281–284, 1996.

[99] Laurence Portier, Sylvain Calloch, Didier Marquis, and Philippe Geyer. Ratchetting under tension-torsion loadings: Experiments and modelling. *Inter-*

national journal of plasticity, 16(3):303–335, 2000. ISSN 07496419. doi: 10.1016/S0749-6419(99)00056-X.

[100] C. Austin, S.K. Bate, L.a. Higham, M.a. Lynch, and D.W. Dean. Derivation of shakedown factors (K s) for Type 316 and Type 321 stainless steel at high temperature. *Materials at High Temperatures*, 28(3):219–224, 2011. ISSN 0960-3409. doi: 10.3184/096034011X13123727647364.

[101] A M Nomine, D Dubois, and D Miannay. Creep and Cyclic Tension Behavior of a Type 316 Stainless Steel at Room Temperature. In *Low-Cycle Fatigue and Life Prediction*. ASTM International, 1982.

[102] J Shit, S Dhar, and S Acharyya. Characterization of Cyclic Plastic Behavior of SS 316 Stainless Steel. *International Journal of Engineering Science and Innovative Technology (IJESIT)*, 2(5):524–538, 2013.

[103] David G. Morris and D. R. Harries. The cyclic creep behaviour of Type 316 stainless steel. *Journal of Materials Science*, 13(5):985–996, 1978. ISSN 00222461. doi: 10.1007/BF00544693.

[104] J Danks and S J Harvey. Hardening interaction in cyclic creep of a type 316 stainless steel at 20^{o}C and 500^{o}C. *Fatigue and Fracture of Engineering Materials and Structures*, 19(4):515–521, 1996. ISSN 8756758X. doi: 10.1111/j.1460-2695.1996.tb00986.x.

[105] Fusahito Yoshida. Uniaxial and biaxial creep-ratcheting behavior of sus304 stainless steel at room temperature. *International Journal of Pressure Vessels and Piping*, 44(2):207–223, 1990.

[106] M. B. Ruggles and E. Krempl. The interaction of cyclic hardening and ratchetting for AISI type 304 stainless steel at room temperature-II. Model-

ing with the viscoplasticity theory based on overstress. *Journal of the Mechanics and Physics of Solids*, 38(4):587–597, 1990. ISSN 00225096. doi: 10.1016/0022-5096(90)90016-W.

[107] E. Krempl. An experimental sturdy of room termperature rate sensitivity creep and relaxation. *Journal of the Mechanics and Physics of Solids*, 27:363–375, 1979.

[108] Guozheng Kang, Qianhua Kan, Juan Zhang, and Yafang Sun. Time-dependent ratchetting experiments of SS304 stainless steel. *International Journal of Plasticity*, 22(5):858–894, 2006. ISSN 07496419. doi: 10.1016/j.ijplas.2005.05.006.

[109] Guozheng Kang, Qing Gao, and Xianjie Yang. A visco-plastic constitutive model incorporated with cyclic hardening for uniaxial/multiaxial ratcheting of SS304 stainless steel at room temperature. *Mechanics of Materials*, 34(9): 521–531, 2002. ISSN 01676636. doi: 10.1016/S0167-6636(02)00153-9.

[110] Guozheng Kang, Qing Gao, and Xianjie Yang. Uniaxial and non-proportionally multiaxial ratcheting of SS304 stainless steel at room temperature: Experiments and simulations. *International Journal of Non-Linear Mechanics*, 39(5): 843–857, 2004. ISSN 00207462. doi: 10.1016/S0020-7462(03)00060-X.

[111] Robert William Kerr Honeycombe. *The plastic deformation of metals*. 1968.

[112] Donald McLean. *Mechanical properties of metals*. Krieger Pub Co, 1977.

[113] S. L. Mannan, K. G. Samuel, and P. Rodriguez. Stress-strain relation for 316 stainless steel at 300K. *Scripta Metallurgica*, 16(3):255–257, 1982. ISSN 00369748. doi: 10.1016/0036-9748(82)90345-3.

[114] M. R. Daymond and P. J. Bouchard. Elastoplastic deformation of 316 stainless steel under tensile loading at elevated temperatures. *Metallurgical and*

Materials Transactions A: Physical Metallurgy and Materials Science, 37(6): 1863–1873, 2006. ISSN 10735623. doi: 10.1007/s11661-006-0129-4.

[115] Seong Gu Hong and Soon Bok Lee. The tensile and low-cycle fatigue behavior of cold worked 316L stainless steel: Influence of dynamic strain aging. *International Journal of Fatigue*, 26(8):899–910, 2004. ISSN 01421123. doi: 10.1016/j.ijfatigue.2003.12.002.

[116] Dae Whan Kim, Woo-Seog Ryu, Jun Hwa Hong, and Si-Kyung Choi. Effect of nitrogen on the dynamic strain ageing behaviour of type 316l stainless steel. *Journal of Materials Science*, 33(3):675–679, Feb 1998. ISSN 1573-4803. doi: 10.1023/A:1004381510474.

[117] Seong Gu Hong and Soon Bok Lee. Dynamic strain aging under tensile and LCF loading conditions, and their comparison in cold worked 316L stainless steel. *Journal of Nuclear Materials*, 328(2-3):232–242, 2004. ISSN 00223115. doi: 10.1016/j.jnucmat.2004.04.331.

[118] Seong Gu Hong, Keum Oh Lee, and Soon Bok Lee. Dynamic strain aging effect on the fatigue resistance of type 316L stainless steel. *International Journal of Fatigue*, 27(10-12):1420–1424, 2005. ISSN 01421123. doi: 10.1016/j.ijfatigue.2005.06.037.

[119] Seong Gu Hong and Soon Bok Lee. Mechanism of dynamic strain aging and characterization of its effect on the low-cycle fatigue behavior in type 316L stainless steel. *Journal of Nuclear Materials*, 340(2-3):307–314, 2005. ISSN 00223115. doi: 10.1016/j.jnucmat.2004.12.012.

[120] M. S. Pham and S. R. Holdsworth. Dynamic strain ageing of AISI 316L during cyclic loading at 300^{o}C: Mechanism, evolution, and its effects. *Ma-*

terials Science and Engineering A, 556:122–133, 2012. ISSN 09215093. doi: 10.1016/j.msea.2012.06.067.

[121] K Yamaguchi, K Kanazawa, and S Yoshida. Crack Propagation in Low-Cycle Fatigue of Type 316 Stainless Steel at Temperatures below 600^{o}C Observed by Scanning Electron Microscopy. *Materials Science and Engineering*, 33:135–139, 1978.

[122] S. L. Mannan. Role of dynamic strain ageing in low cycle fatigue. *Bulletin of Materials Science*, 16(6):561–582, 1993. ISSN 02504707. doi: 10.1007/BF02757656.

[123] Jean Lemaitre and Jean-Louis Chaboche. *Mechanics of solid materials*. Cambridge university press, 1990.

[124] Lakhdar Taleb and Georges Cailletaud. Cyclic accumulation of the inelastic strain in the 304l ss under stress control at room temperature: Ratcheting or creep? *International Journal of Plasticity*, 27(12):1936–1958, 2011.

[125] M. B. Ruggles and E. Krempl. The Influence of Test Temperature on the Ratchetting Behavior of Type 304 Stainless Steel. *Journal of Engineering Materials and Technology*, 111(4):378, 1989. ISSN 00944289. doi: 10.1115/1.3226483.

[126] N Ohno, Y Takahashi, and K Kuwabara. Constitutive modeling of anisothermal cyclic plasticity of 304 stainless steel. *Journal of Engineering Materials and Technology*, 111(1):106–114, 1989.

[127] Nobutada Ohno. Recent topics in constitutive modeling of cyclic plasticity and viscoplasticity. *Applied Mechanics Reviews*, 43(11):283–295, 1990.

[128] Erhard Krempl and Toshiya Nakamura. The influence of the equilibrium stress growth law formulation on the modeling of recently observed relaxation behaviors. *JSME International Journal Series A Solid Mechanics and Material Engineering*, 41(1):103–111, 1998.

[129] P Rodriguez. Serrated plastic flow. *Bulletin of Materials Science*, 6(4):653–663, 1984.

[130] Wade Karlsen, Mykola Ivanchenko, Ulla Ehrnstén, Yuriy Yagodzinskyy, and Hannu Hänninen. Microstructural manifestation of dynamic strain aging in aisi 316 stainless steel. *Journal of nuclear materials*, 395(1-3):156–161, 2009.

[131] Tasnim Hassan, Lakhdar Taleb, and Shree Krishna. Influence of non-proportional loading on ratcheting responses and simulations by two recent cyclic plasticity models. *International Journal of Plasticity*, 24(10):1863–1889, 2008. ISSN 07496419. doi: 10.1016/j.ijplas.2008.04.008.

[132] HL Eiselstein and DJ Tillack. The invention and definition of alloy 625. *Superalloys*, 718(625):1–14, 1991.

[133] Lewis E Shoemaker. Alloys 625 and 725: trends in properties and applications. *Superalloys*, 718(625):409–418, 2005.

[134] James M Rakowski, Charles P Stinner, Mark Lipschutz, and J Preston Montague. The use and performance of wrought 625 alloy in primary surface recuperators for gas turbine engines. *Proceedings of Superalloys*, 718:625–706, 2005.

[135] Charles Thomas and Peter Tait. The performance of alloy 625 in long-term intermediate temperature applications. *International journal of pressure vessels and piping*, 59(1-3):41–49, 1994.

[136] MJ Donachie and SJ Donachie. Superalloys a technical guide, asm international. *The Materials Society, Materials Park, Ohio*, 2002.

[137] WL Mankins and S Lamb. Nickel and nickel alloys. *ASM International, Metals Handbook, Tenth Edition.*, 2:428–445, 1990.

[138] T Bui-Quoc, R Gomuc, A Biron, HL Nguyen, and J Masounave. Elevated temperature fatigue-creep behavior of nickel-base superalloy in 625. In *Low cycle fatigue*. ASTM International, 1988.

[139] Lorena Mataveli Suave, Jonathan Cormier, Denis Bertheau, Patrick Villechaise, Aurélie Soula, Zéline Hervier, and Florence Hamon. High temperature low cycle fatigue properties of alloy 625. *Materials Science and Engineering: A*, 650:161–170, 2016.

[140] A Nagesha, P Parameswaran, Niraj Kumar, R Sandhya, and MD Mathew. Influence of re-solutionising treatment on the cyclic deformation behaviour of a service-exposed inconel® 625 superalloy. *Materials at High Temperatures*, 29(1):49–53, 2012.

[141] Vani Shankar, M Valsan, K Bhanu Sankara Rao, and SL Mannan. Effects of temperature and strain rate on tensile properties and activation energy for dynamic strain aging in alloy 625. *Metallurgical and Materials Transactions A*, 35(10):3129–3139, 2004.

[142] In Sup Kim and Mahesh C Chaturvedi. Serrated flow in inconel 625. *Transactions of the Japan institute of metals*, 28(3):205–212, 1987.

[143] Arnomitra Chatterjee, Garima Sharma, R Tewari, and JK Chakravartty. Investigation of the dynamic strain aging and mechanical properties in alloy-625

with different microstructures. *Metallurgical and Materials Transactions A*, 46 (3):1097–1107, 2015.

[144] Mauro M de Oliveira, Antônio A Couto, Gisele FC Almeida, Danieli AP Reis, Nelson B de Lima, and Renato Baldan. Mechanical behavior of inconel 625 at elevated temperatures. *Metals*, 9(3):301, 2019.

[145] P Maj, J Zdunek, J Mizera, KJ Kurzydlowski, B Sakowicz, and M Kaminski. Microstructure and strain-stress analysis of the dynamic strain aging in inconel 625 at high temperature. *Metals and Materials International*, 23(1):54–67, 2017.

[146] Tasnim Hassan and Stelios Kyriakides. Ratcheting of cyclically hardening and softening materials: I. uniaxial behavior. *International Journal of Plasticity*, 10(2):149–184, 1994.

[147] Bing Lin, LG Zhao, Jie Tong, and H-J Christ. Crystal plasticity modeling of cyclic deformation for a polycrystalline nickel-based superalloy at high temperature. *Materials Science and Engineering: A*, 527(15):3581–3587, 2010.

[148] Saeede Ghorbanpour, Milovan Zecevic, Anil Kumar, Mohammad Jahedi, Jonathan Bicknell, Luke Jorgensen, Irene J Beyerlein, and Marko Knezevic. A crystal plasticity model incorporating the effects of precipitates in superalloys: application to tensile, compressive, and cyclic deformation of inconel 718. *International Journal of Plasticity*, 99:162–185, 2017.

[149] J L Chaboche and D Nouailhas. Constitutive Modeling Of Ratchetting EffectsPart I: Experimental Facts And Properties Of The Classical Models. *Journal of Engineering Materials and Technology*, 111(4):384–392, 1989. ISSN 0094-4289. doi: 10.1115/1.3226484.

[150] J. L. Chaboche and D. Nouailhas. Constitutive Modeling of Ratchetting EffectsPart II: Possibilities of Some Additional Kinematic Rules. *Journal of Engineering Materials and Technology*, 111(4):409, 1989. ISSN 00944289. doi: 10.1115/1.3226488.

[151] Yasuaki Ohmi, Eiichi TANAKA, Sumio MURAKAMI, Morio JINCHO, and Tetsuya SUZUKI. Constitutive modeling of proportional/nonproportional cyclic plasticity for type 316 stainless steel applicable to a wide temperature range. *Journal of the Society of Materials Science, Japan*, 44(507Appendix): 247–253, 1995.

[152] J. L. Chaboche. A review of some plasticity and viscoplasticity constitutive theories. *International Journal of Plasticity*, 24(10):1642–1693, 2008. ISSN 07496419. doi: 10.1016/j.ijplas.2008.03.009.

[153] A. Mishra, P. Chellapandi, R. Suresh Kumar, and G. Sasikala. Comparative Study of Cyclic Hardening Behavior of SS 316 L Using Time Independent and Dependent Constitutive Modeling: A Simplified Semi-implicit Integration Approach. *Transactions of the Indian Institute of Metals*, 68(4):623–631, 2015. ISSN 0972-2815. doi: 10.1007/s12666-014-0492-6.

[154] HF Abdalla, Maher Y. A. Younan, and Mohammad M Megahed. Shakedown limit load determination for a kinematically hardening 90 ° pipe bend subjected to steady internal pressures and cyclic bending moments. *Journal of Pressure Vessel Technology*, 133:051212–1–10, 2011. doi: 10.1115/1.4003474. URL `http://proceedings.asmedigitalcollection.asme.org/article.aspx?articleid=1461627`.

[155] J-W Simon and D Weichert. Shakedown analysis of engineering structures with

limited kinematical hardening. *International Journal of Solids and Structures*, 49(15-16):2177–2186, 2012.

[156] M Ruggles and E Krempl. Rate dependence of ratchetting of aisi type 304 stainless steel at room temperature. *Report*, 2050:87–41, 1987.

[157] John Gaskins, N Scott Barker, and Matthew R Begley. Comprehensive solutions for the response of freestanding beams with tensile residual stress subject to point-loading. *Journal of Applied Mechanics*, 81(3):031008, 2014.

[158] Matthew R Begley and N Scott Barker. Analysis and design of kinked (bent) beam sensors. *Journal of Micromechanics and Microengineering*, 17(2):350, 2007.

[159] MK Abass and MA Elshafei. Linear and nonlinear finite element modeling of advanced isotropic and anisotropic beams, part i: Euler bernoulli theory. In *13th International Conference on Aerospace Sciences & Aviation Technology*, 2009.

Appendix A

Supplementary Analysis for Shakedown of Beams

A.1 Small deformation plane strain analysis for decoupled thermoelastic loading

The analysis for plane strain assumptions is identical to that presented in Section 2.1.1 if $E/(1-\nu)$ is substituted for E. The corresponding elastic limit equation from Section 2.1.1, Eqn. 2.2 for plane strain is:

$$\frac{PL^2}{t^2} + \frac{2E\alpha\Delta T}{1-\nu} = 2\sigma_o, \tag{A.1}$$

and the shakedown limit equation (similar to Eqn. 2.7 in Section 2.1.1) is:

$$\frac{PL^2}{t^2} + \frac{E\alpha\Delta T}{1-\nu} = 2\sigma_o. \tag{A.2}$$

A.2 Plane stress and plane strain small deformation analysis of clamped and pinned beams under decoupled thermomechanical loading

Integrating the equation that relates the pressure, P, and the beam deflection, u, ($d^4u/dx^4 = P/EI$) and applying the boundary conditions for a pinned beam gives the moment distribution:

$$M(x) = EI\frac{d^2u}{dx^2} = \frac{P}{8}\left(4x^2 - L^2\right), \tag{A.3}$$

where I is the second moment of area of the beam cross-section about the neutral axis. The resulting distribution of mechanical stress in the pinned beam is:

$$\sigma_{xx}(x, y) = -M\frac{y}{I} = -\frac{3Py}{2t^3}\left(4x^2 - L^2\right). \tag{A.4}$$

The axial thermomechanical stress is:

$$\sigma_{xx} = -\frac{3Py}{2t^3}\left(4x^2 - L^2\right) - E\alpha\Delta T. \tag{A.5}$$

The critical cross-section of the pinned beam is at the middle, $x = 0$, where the bending moment due to the mechanical loading is maximum (Figure 2.2). Moreover, the pressure creates compressive stresses below the beam neutral axis and tensile stresses above the neutral axis. Hence, the elastic limit is found upon thermal unloading by setting $\sigma_{xx}(0, -t/2) = -\sigma_o$, where both the thermal load and pressure contributes to the compressive stresses. The elastic limit equation is then:

$$\frac{3PL^2}{4t^2} + E\alpha\Delta T = \sigma_o. \tag{A.6}$$

The potential residual stress, $\bar{\rho}_{ij}$, is the stress necessary to return the maximum (absolute value) fictitious thermomechanical stress to the yield limit:

$$\sigma_{xx}(0, -\frac{t}{2}) = -\frac{3PL^2}{4t^2} - E\alpha\Delta T + \bar{\rho}_{ij} = -\sigma_o, \tag{A.7}$$

giving,

$$\bar{\rho}_{ij} = \frac{3PL^2}{4t^2} + E\alpha\Delta T - \sigma_o. \tag{A.8}$$

The shakedown limit load (the maximum allowable ΔT) is determined by the case where the residual stress field brings the point at $y = t/2$ to the yield limit in tension upon thermally unloading. Upon thermally unloading, the stress distribution at the critical location $y = t/2$ is:

$$\sigma_{xx}(0, \frac{t}{2}) = \frac{3PL^2}{4t^2} + \bar{\rho}_{ij}, \tag{A.9}$$

or substituting the residual stress from Eq. (A.8):

$$\sigma_{xx}(0, \frac{t}{2}) = \frac{3PL^2}{4t^2} + \frac{3PL^2}{4t^2} + E\alpha\Delta T - \sigma_o. \tag{A.10}$$

Again, to solve for the shakedown limit load, the stress at $y = t/2$ should just reach yield in tension when thermally unloading, resulting in the shakedown limit equation:

$$\frac{3PL^2}{2t^2} + E\alpha\Delta T = 2\sigma_o. \tag{A.11}$$

The plane strain solution for this end condition is identical with the plane stress analysis in Eqs. (A.3)-(A.11) if $E/(1-\nu)$ is substituted for E. The elastic limit equation assuming plane strain for pinned beams is:

$$\frac{3PL^2}{4t^2} + \frac{E\alpha\Delta T}{1-\nu} = \sigma_o. \tag{A.12}$$

and the shakedown limit equation assuming plane strain for pinned beams is:

$$\frac{3PL^2}{2t^2} + \frac{E\alpha\Delta T}{1-\nu} = 2\sigma_o, \tag{A.13}$$

Appendix B

Analytic Thermoelastic Buckled Beam Derivation

In the following, beams are described using a one-dimensional version of nonlinear von Karman plate theory under plane stress conditions to develop a thermoelastic solution similar to references [157, 158]. The corresponding assumptions are made such that plane sections perpendicular to the neutral axis in the undeformed beam shape will remain plane, rigid and perpendicular to the neutral axis after deformation. This allows one to neglect displacements due to Poisson's effect in the z-axis direction, Figure 2.2b [159]. Note that the following assumes that the beam cross-section is constant or varies smoothly, and the material is homogeneous and isotropic. Furthermore, it is assumed that the beam is slender enough to ignore transverse shear and moderate rotations are allowed. With these assumptions, the total axial strain in the beam (which is the only non-zero strain component resulting from the combined thermomechanical loading) is calculated from the beam kinematics:

$$\varepsilon_{xx}(x,y) = u'(x) - yw''(x) + \frac{1}{2}\left(w'(x)\right)^2 - \alpha\Delta T, \tag{B.1}$$

where y denotes the distance from the beam neutral axis and the prime, $'$, denotes a

derivative with respect to the x coordinate. The terms $u(x)$ and $w(x)$ represent the axial displacement and the transverse displacement at the neutral axis, respectively. The third (nonlinear) term accounts for moderate rotations, which can generate significant stretching of the neutral axis when transverse displacements, $w(x)$, are comparable to the beam thickness [158]. The fourth thermal strain term (- $\alpha\Delta T$) is introduced here as negative due to the type of loading and constraint provided by the boundary conditions considered – clamped and pinned. Under uniform heating, the boundary constraints resist thermal expansion, inducing compressive thermal strains. The uniform heating from a reference temperature, T_o is represented by $\Delta T = T - T_0$. With the strain from Eq. (B.1), the axial stress at the neutral axis ($y = 0$) can be found using Hooke's Law:

$$\sigma_{xx}(x, y = 0) = E\left(u'(x) + \frac{1}{2}\left(w'(x)\right)^2 - \alpha\Delta T\right). \tag{B.2}$$

Note that the stress at the neutral axis can be compressive or tensile depending on the relative magnitude of the thermal strain. A variational approach is used to obtain the transverse beam displacement. As a result, it is found that the derivative of the stress at the neutral axis is zero, $\sigma'(x, y = 0) = 0$, hence it must be uniform along the beam axis. In the following, this constant reference level for the axial stress at the neutral axis is denoted by σ_{na}. The governing equation for the beam transverse displacement, $w(x)$, is:

$$w'''' + \lambda^2 w'' = \frac{12P}{Et^3}, \tag{B.3}$$

where the eigenvalue, λ, is introduced:

$$\lambda = \sqrt{-\frac{12\sigma_{na}}{Et^2}}, \qquad \text{or} \qquad \sigma_{na} = -\frac{\lambda^2 Et^2}{12}. \tag{B.4}$$

As increasing the temperature change (ΔT) will cause compressive axial stresses in the beam, from this point on, all of the stresses given by σ_{na} (Eq. (B.4)) are assumed to be compressive. With this governing fourth order differential equation and the boundary conditions for the clamped beam, the resulting transverse displacement solution for the beam is:

$$w(x) = \frac{6P}{\lambda^3 E t^3}\left(\lambda x\left[x - L\right] + L\cot\left(\frac{L\lambda}{2}\right)\left[\cos\left(\lambda x\right) - 1\right] + L\sin\left(\lambda x\right)\right). \tag{B.5}$$

Note that the eigenvalue, λ, depends on the applied thermal (compressive) load and the distributed pressure load. The eigenvalue can be found using the constraint that the axial displacement at the fixed ends of the beam must be zero. Enforcing zero displacement with Eq. (B.1) at $x = L$ yields:

$$u(x = L) = L\left(\frac{\sigma_{na}}{E} + \alpha\Delta T\right) - \frac{1}{2}\int_0^L \left[w'(x)\right]^2 dx = 0. \tag{B.6}$$

Taking the derivative of the transverse displacement Eq. (B.5) and substituting it into Eq. (B.6), results in the following implicit equation for the eigenvalue λ:

$$\frac{L\left(\frac{12P}{Et^3}\right)^2 \csc\left(\frac{\lambda L}{2}\right)^2 \left[4\left(\lambda^2 L^2 - 6\right) - \left(\lambda^2 L^2 - 24\right)\cos\left(\lambda L\right) + 9\lambda L\sin\left(\lambda L\right)\right]}{48\lambda^6} = L\left(\alpha\Delta T - \frac{t^2\lambda^2}{12}\right). \tag{B.7}$$

The eigenvalue that satisfies Eq. (B.7) can be found for a given ΔT and P and used in Eq. (B.5) to find the transverse displacement. Substituting Eqs. (B.5) and (B.6)

in Eq. (B.1) gives the axial stress of the beam:

$$\sigma(x,y) = \frac{-\lambda^2 E t^2}{12} - \frac{6yP}{\lambda^2 t^3}\left(2 - L\lambda\cot\left(\frac{L\lambda}{2}\right)\cos\left(\lambda x\right) - L\lambda\sin\left(\lambda x\right)\right). \qquad \text{(B.8)}$$

Biography

Ismail Soner Cinoglu is a Ph.D. candidate in the Mechanical Engineering and Mechanics Department at Lehigh University. He obtained his B.S. degree from the Mechanical Engineering Department at TOBB University of Economics and Technology, Ankara, Turkey, in 2012. He received his M.S. degree from the Mechanical Engineering Department at Koc University, Istanbul, Turkey in 2014. During his time at Lehigh University, he was awarded an ICMR International Research Fellowship and was a visiting scholar at Aachen University of Applied Sciences. He served in the Graduate Student Senate as Treasurer (2017), Interim Vice President (2018 summer) and as the Chair of the Budget Committee for Graduate Student Clubs (2017). He is a Rossin Doctoral Fellow and he received an Honorable Mention for the Graduate Life Leadership Award at Lehigh University.